Title	Single crystal preparation of LaB_6 and related borides and their electronic structures
Author(s)	Tanaka, Takaho
Citation	大阪大学, 1981, 博士論文
Version Type	VoR
URL	https://hdl.handle.net/11094/24347
rights	
Note	

Single crystal preparation of LaB_6 and related borides

and their electronic structures

Takaho Tanaka

Contents

Abstracts

Abstracts

Stoichiometric and high-purity single crystals of LaB_6, rare-earth hexaborides (CeB_6, SmB_6, EuB_6 and GdB_6) and transition metal diborides (ZrB_2, TiB_2 and CrB_2) have been prepared by the floating zone method in a pressurized gas atmosphere. Multiple zone refining improved the purity of the crystals of LaB_6 and other congruently melt hexaborides markedly. The zone leveling method has been used to obtain the stoichiometric crystals of GdB_6 and diborides.

The de Haas-van Alphen effect measurements on LaB_6 and IVth group diborides (ZrB_2 and TiB_2) have been carried out at temperatures of about 1.5 K in magnetic field up to 6 T. The experimental Fermi surfaces of LaB_6 and diborides were constructed. The Fermi surface of LaB_6 is a multiply-connected Fermi surface. The Fermi surface of ZrB_2 and TiB_2 consists of electron and hole Fermi surfaces, indicating that they are semi-metals. The lattice dynamic properties of LaB_6 have been measured. The results were expalined by a lattice vibration model proposed.

The conduction band structures of LaB_6 and Ivth group diborides and their bonding natures are discussed according to the experimenatl results and the theoretical band structure calculations refered

Chapter 1. Introduction

Metal borides, in which the boron to metal atom ratio is two or larger, are the refractory materials like transition metal carbides, nitrides and silicides. They have high melting temperatures, large hardness values as shown in Fig.1-1(a) and (b), and considerable chemical stability. Many of them also have low electrical resistivities as shown in Fig.1-1(c), making them prime candidates for use in various refractory situations such as thermionic electron emission cathodes and magnetohydrodynamic channel electrodes.

It would be of interest to inquire, what kind of chemical bonding is most responsible for the combination of their metallic conductivity and refractory properties. There are many contradictory theories of bonding for these materials, and available experimental evidence is insufficient to distinguish unambiguously between these theories.

In transition metal carbides and nitrides, for example, important bonds can be formed between both metal-metal pairs of atoms and metal-nonmetal pairs. Most theories have attempted to determine the relative importance of metal-metal versus metal-nonmetal bonds. The theories, moreover, have concerned about the direction of electron transfer, if any, between metal and nonmetal atoms. The recent band structure calculations emphasize the importance of metal-nonmetal bonding, because the band arising from the p-wave functions of the nonmetals and the d-wave functions of the metals is low in energy relative to the Fermi
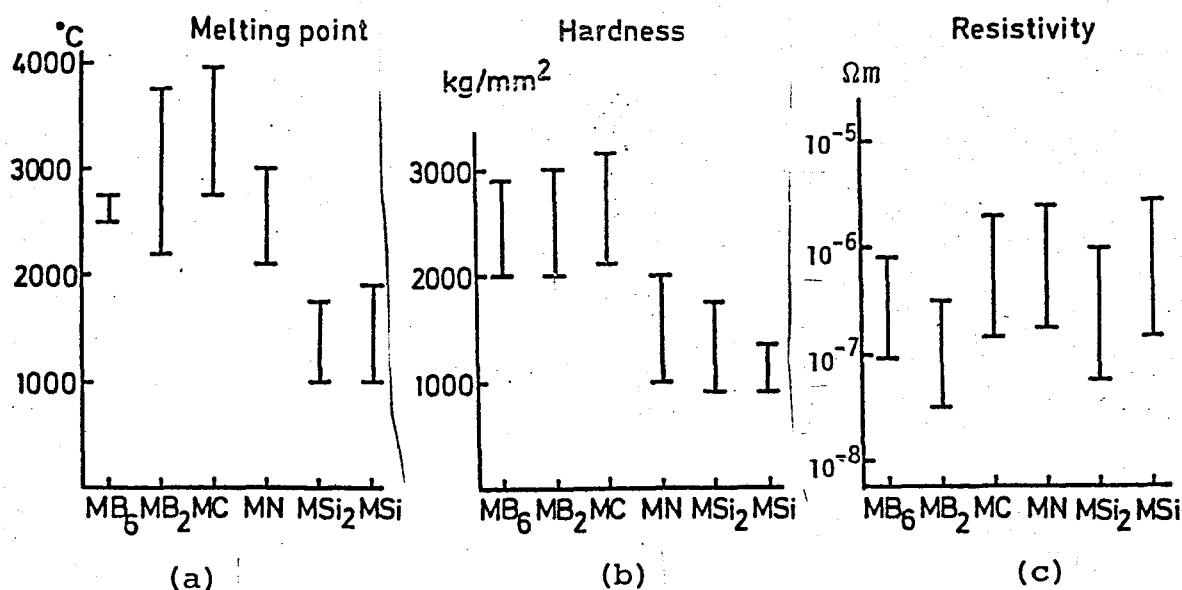
Fig.1-1. Melting point(a), hardness(b) and electrical resistivity(c) of borides, carbides, nitrides and silicides[1,2].

level and these p-d hybrid bands are occupied.

From the viewpoint of the band structure investigation, existing theoretical treatments of the electronic structures of the boron-rich higher borides are at best first approximations. Moreover, there are few experimental investigations which can be correlated to the theoretical energy band structure. If any, only polycrystalline specimens have been used for most measurements on relevant physical properties of the higher borides though the experiments on detailed electronic properties usually require high purity single crystals. Thus, the understanding of the electronic structures and bonding nature of the higher borides has been restricted to qualitative aspects only. It is the main purpose of the present study to clarify experimentally the electronic structures of the metal hexaborides by the Fermi surface construction, which lends a quantitative support to the

band structure calculation. For comparison, diborides which have been considered as the boron-rich higher borides from their bonding nature, are also examined because they have the lowest boron content among the higher borides. Preparation of high purity single crystals is another purpose of the present study, because such samples are needed for carrying out the measurements on the electronic structures of these borides.

Metal borides have considerably wide composition ranges as compared with carbides, nitrides and silicides. The latter have the composition ranges of,

$$1/3 \leq C,N,Si/M \leq 2 \qquad [1,2].$$

The composition range of borides is

$$1/4 \leq B/M \leq 66 \qquad [1,3].$$

Boron rich phases are characteristic in the borides. The higher borides are closely related to elemental boron and could be regarded as 'stabilized' modifications of the element. Thus the boron arrangement is an interesting aspect of the crystal structure of the borides. Even in the metal-rich phases, a boron arrangement exists such that the interatomic B-B distance is close to the covalent B-B distance. The boron atoms occur isolated or take part in B-B bonds, forming pairs, zig-zag chains, branched chains and double chains following with increase of boron content. This series of non-metal atom arrangement is observed also for silicides[1].

In the higher borides, strongly bonded two- and three-

dimensional networks of boron atoms exist. Basic compounds of the higher boride are MB_2, MB_4, MB_6 and MB_{66}.

The boron arrangement in the diborides is a two dimensional network like the graphite layer. As shown in Fig.1-2(a), metal atoms and boron atoms are stacked alternatively forming hexagonal net planes[1].

In the composition range, $4 \leq B/M$, the boron arrangement becomes a three dimensional network and it contains polyhedra consisting of a group of borons. The MB_6 structure contains octahedra consisting of six borons. The boron octahedra are located at cube corners of the simple cubic structure. The metal atom occupies the large open space at the body center of the cube. The crystal structure of MB_6 is shown in Fig.1-2(b)[1].

The boron framework of MB_4 consists of both elements of the MB_6 and MB_2 structures as shown in Fig.1-2(c). The MB_4 structure has tetragonal symmetry and the boron layers and the metal layers are stacked alternatively along the [001] direction[1].

The basic unit of the MB_{12} structure is a 12 atom cubo-octahedron. The cubo-octahedron and metal atom form a fcc structure of NaCl type. The cubo-octahedra are bonded together to form a rigid three dimensional framework of boron atoms as shown in Fig.1-2(d)[3].

In the crystal structure of MB_{66}, the basic polyhedron of boron is a supericosahedron composed of thirteen B_{12} icosa-hedra, a $B_{12}(B_{12})_{12}$ group. Two kinds of supericosahedra that differ only by the 90° rotation, form a interpenetrating fcc

(a)

(b)

(c)

(d)

ONE OF RE ATOMS
IN OCTANT OF CELL

● = RE atom in one
of six sites in octant.

⊖ = ⊕ = B₁₂ (B₁₂)₁₂ group.

⊖ and ⊕ differ by
90° rotation.

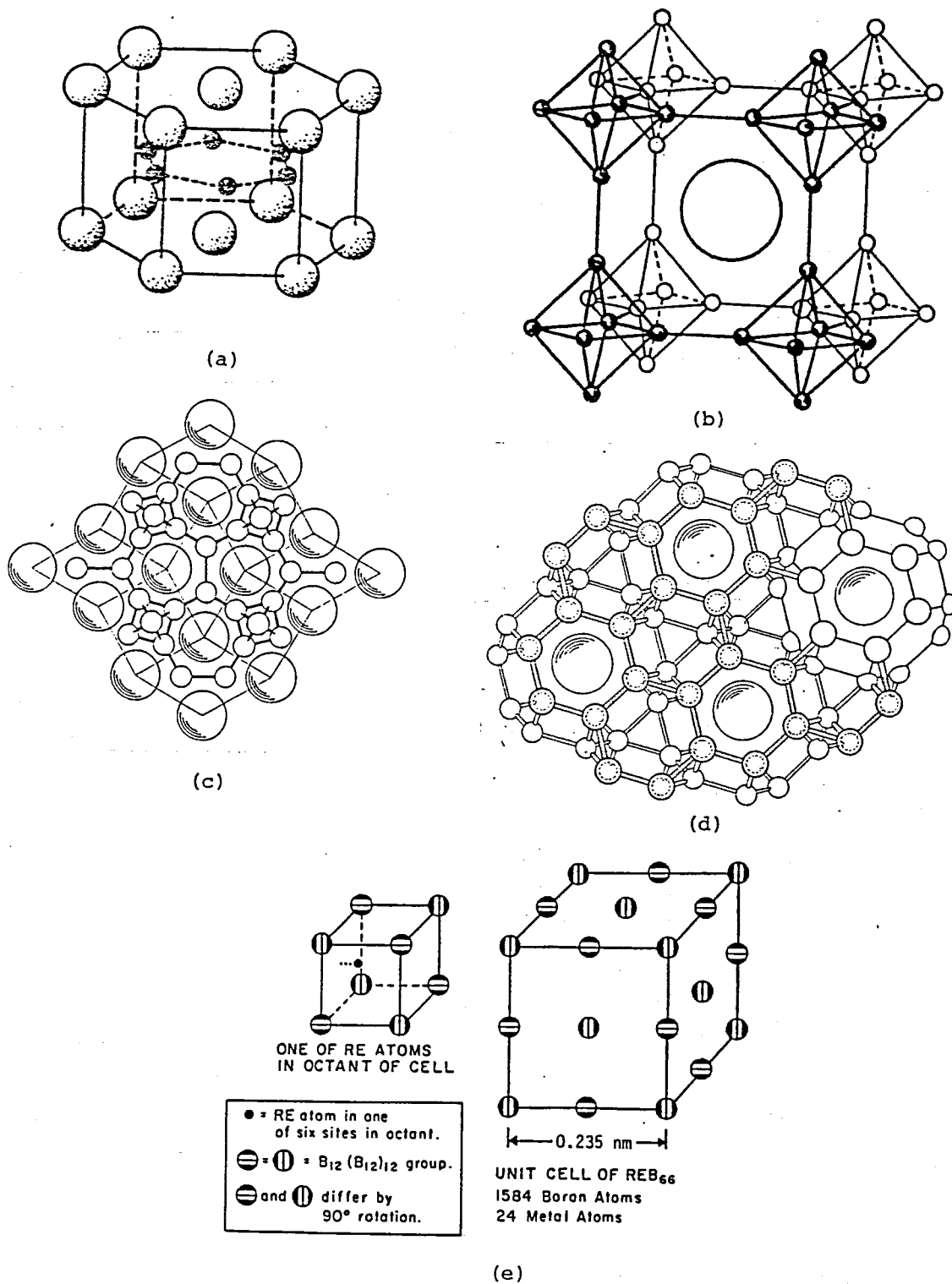|←——0.235 nm——→|

UNIT CELL OF REB₆₆
1584 Boron Atoms
24 Metal Atoms

(e)

Fig.1-2. Schematic drawing of the crystal structures of (a) MB_2,
(b) MB_6, (c) MB_4 in the projection down to the (001) plane[3],
(d) MB_{12} in the projection down to the (111) plane[3] and (e) MB_{66}.

lattice. Thus there are eight of the supericosahedra per unit cell. In each octant of the unit cell, there are six metal atom sites which are located at 0.127 nm (for the case of YB_{66}) inside the cell from the face center of the octant. Only half of the sites are occupied randomly. The body center of each octant is filled by either a 36- or 48-boron atom group with equal content. The average formula for one octant of the unit cell is

$$M_3[B_{12}(B_{12})_{12}][B_{36}]_{1/2}[B_{48}]_{1/2}.$$

Thus there are 24 formula weights per unit cell[4]. The crystal structure of MB_{66} is shown in Fig.1-2(e).

Bonding distances of boron atoms have been measured for some hexaborides[3]. The inter-octahedron B-B distance is mostly observed at about 0.166 nm (0.166 - 0.175 nm) and the intra-octahedron one is about 0.176 nm (0.175 - 0.178 nm). The average B-B distances in MB_{12} and MB_{66} are similar to the covalent B-B distance of 0.176 nm[5]. The lattice constants of the higher borides are almost independent of the change of the metal ion radius. For example, correlations among rare-earth boride lattice constant versus RE^{3+} ionic radius reveal much information concerning the rigidity of the different types of boron sublattices. The normalized slope K is defined as[4]

$$K = (1/n)[\Delta(\text{unit cell dimension})/\Delta r^{3+}],$$

where n is the normalization factor, representing the number of metal radii occuring in the structure along the direction of

the unit cell dimension being considered, and the quantity in brackets is the slope of the linear plots of the lattice constant versus RE^{3+} ionic radius. If the changes of the unit cell dimension were determined solely by the change in RE^{3+} radius, the constant K would, of course, be equal to unity. As shown in Table 1-1, the K value of REB_6, REB_{12} and REB_{66} are 0.19, 0.13 and 0.15, respectively. This indicates very rigid three-dimensional boron frameworks in these structures. In the case of REB_4, the unit cell dimension varies with the change of ionic radius, having

Table 1-1

Normalized relating the change in unit cell dimension per change in the ionic radii of trivalent rare-earth ions [4].

Phase	Unit cell parameter	K
REB_2	a	0.41
	c	1.08
REB_4	a	0.31
	c	0.44
REB_6	a	0.19
REB_{12}	a	0.13
REB_{66}	a	0.15

comparatively large K values. The difference between K(a) and K(c) values for REB_2 is to be expected since B-B bonding occurs only in the form of graphite like nets in the xy plane of this structure.

In the boron-rich higher borides, the first calculation of the energy band structure was carried out for hexaborides by Longuet-Higgins and Roberts [6] using the tight binding approxi-

mation. They assumed that the bonding in the boron framework is dominant and the bonding between metal atom and boron framework is very weak. Only the boron 2s and 2p states were used for the calculation of the energy band structure of the boron framework. The orbitals of the metal atom were neglected. The energy band structure which was obtained is shown in Fig.1-3. Numerals shown in each energy band designate the number of electrons being required to fill each band. Low lying three bonding bands, E, A and B correspond to the intra-octahedron B-B bondings and the band F corresponds to the inter-octahedron B-B bondings. Thus, the stabilization of the MB_6 structure by filling all the bonding orbitals of the boron framework requires twenty electrons as a whole. Since the number of valence electrons of a boron atom is three, having electronic configuration of $2s^2 2p^1$, the valence electrons of six boron atoms are
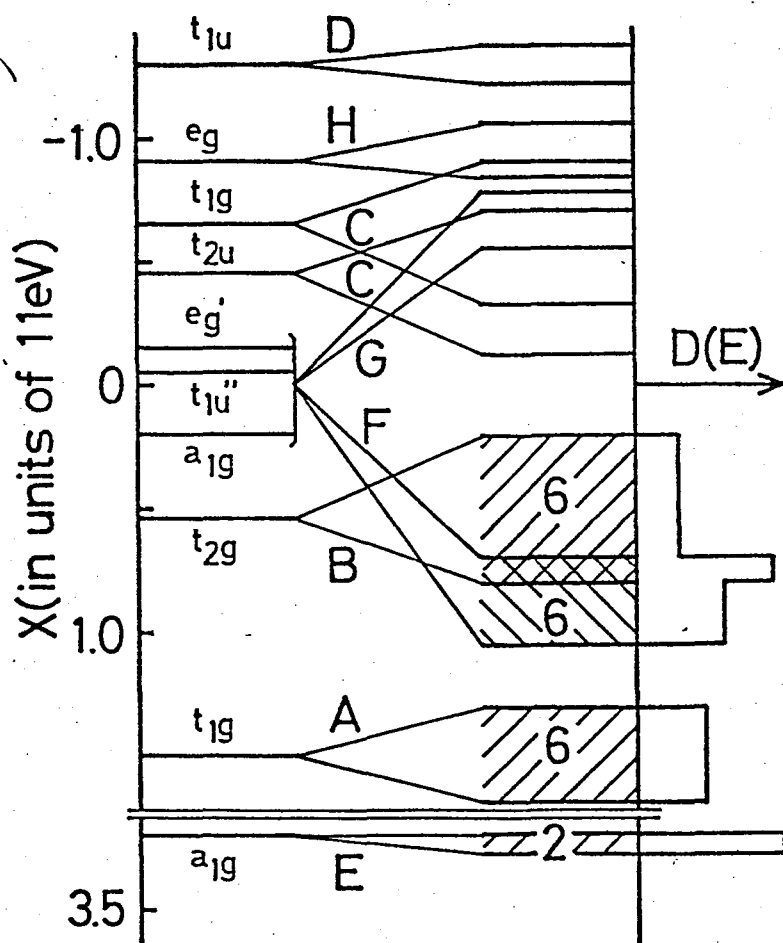

Fig.1-3. Energy band structure of MB_6 calculated by Longuet-Higgins and Roberts[6] using tight binding approximation.

insufficient to fill the bonding band of the boron framework. They assumed that the deficient two electrons are supplied from the metal atom. Therefore, the hexaborides of divalent metal occur as a semiconductor. In the hexaborides of trivalent metal, the remaining one electron which is free from the boron lattice bonding, becomes a mobile electron and contributes to metallic conduction.

Lipscomb and Britton[7] extended the above consideration over the whole MB_2, MB_4, MB_6 and MB_{12}. They examined the electronic structure of these borides using the molecular orbital approach. Their results reached for the four binary borides were similar in that the stabilization of each structure requires two electrons to transfer from each metal atom to the boron framework. This closed-shell structure for the boron units in the metal borides leads to a simple picture of a negatively charged boron framework containing positive metal ions located in the interstices.

In the case of diborides, the above model postulates that the hexagonal boron layer is isoelectronic with the graphite layer. The bonding in the boron layer requires four electrons per atom for a closed shell configuration: three for the bonding sp^2-bands and one for the p_z-band. The metal atoms in the diboride must provide the fourth electron for each boron if graphite-like bonding is exist.

As compared with the higher borides, the direction of electron transfer in the metal-rich lower borides of $B/M \leq 1$,

is considered to be opposite; from boron atom to metal atom[8].

Such consideration is quite similar to that of the interstitial

compound model; metal packing is modified to boride structure

owing to the boron interstitials. The energy bands are regarded

as being essentially similar to those in the elementary metal

but modified by the presence of nonmetal atoms. Valence electrons

of boron atoms are donated to the incompletely filled metallic

d-band which has a high density of states.

The bonding model of the higher borides based on the

electron transfer theory seems to be confirmed by several experi-

mental facts. Johnson and Daane[9] measured the Hall coefficients

of the series of yttrium borides, YB_2, YB_4, YB_6 and YB_{12} and they

concluded that all yttrium borides are one-electron conductor.

In addition, they showed that the temperature dependence of the

electrical conductivities of CaB_6, SrB_6 and BaB_6 is like that

of the semiconductors. These results seemed to lend support to

the electron transfer theory for the higher borides.

Silver and Bray[10] carried out NMR measurement of ^{11}B in

TiB_2 and ZrB_2. The small value of $|e^2qQ|$ observed by them was

explained by reason that the boron atoms have the closed-shell

configuration which causes a spherical electric field gradient

at the boron site. They concluded that the boron layer is

isoelectronic with the graphite layer.

Etourneau et al.[11] measured the magnetic susceptibility,

the thermoelectric power and the heat capacity of hexaborides

of Th, La, Yb, Ca and Sr. They found that ThB_6 and LaB_6 are

metallic and the hexaborides of Yb, Ca and Sr are semiconductors. Furthermore, Samsonov[12] estimated the carrier concentrations of the hexaborides of Y, La, Ce, Pr, Nd, Gd and Tb to be approximately one per formula weight, and that of the hexaborides of Ca, Sr, Ba and Yb to be less than 0.1 and that of ThB_6 to be two. Every result seems to support the above electron transfer theory.

Bondings in the higher borides can be expressed as follows; the dominant bonding is the covalent B-B bonding which constructs the boron framework. To complete this B-B bonding, the deficient electrons are donated from the metal atom. Therefore bonding between the metal atom and the boron framework is ionic. The valence electrons free from the boron lattice bonding become mobile electrons which contribute to metallic conductivity.

Although the above models for the electronic structure of the higher borides are overly simplistic, they appear to be compatible with many experimental results and have been widely supported[3,4]. However, the bonding between the metal and the boron has not been critically examined by any of the above treatments and the conduction band structure has not been examined at all. More experiments on electronic properties and an experimental approach to band structure calculations are needed.

There are few experimental data of MB_6 and MB_2 with respect to information on the conduction band structure which consists of the following: (1) shape of the Fermi surface, (2) cyclotron mass, (3) Fermi energy, (4) density of states and (5) electron concentration. The carrier concentrations of the hexaborides

of triavlent metal are approximately one per formula weight as mentioned above. Many metals lower their electrical resistivity when they form borides, as shown in Table 1-2.

For LaB_6, Etourneau et al.[11] obtained the γ-value of electronic heat capacity to be 2.6 mJ/mole·K^2, resulting in an electron density of states at the Fermi level to be 1.1 states/eV·unit cell. Using the free electron model, γ is expressed as $\frac{1}{2}\pi^2 \frac{N}{E_F} k_B^2$, where the Fermi energy $E_F = \frac{\hbar^2}{2m_0}(\frac{3\pi^2 N}{V})^{2/3}$, k_B, $\hbar$ and m_0 have the usual meaning, N the number of electrons and V the crystal volume. The free electron γ-value of LaB_6 is 1.67 mJ/mole·K^2. This gives the thermal effective mass of the conduction electron as $m_{therm.} = \frac{\gamma_{obs.}}{\gamma_{free\ electron}} m_0 = 1.6\ m_0$. However, this expression is only significant if the Fermi surface consists of one nearly spherical surface. In a later section, the value of the thermal effective mass can be understood by the fact that the Fermi surface of LaB_6 consists of three equivalent pieces in the Brillouin zone and the effective

Table 1-2

Electrical resistivities of some metals[13] and their borides

Substance	Resistivity e (10^{-8} Ωm) at room temperature
La	79
LaB_6	8.9
Ce	81
CeB_6	27
Gd	134
GdB_6	32
Ti	43.1
TiB_2	6.5
Zr	42.4
ZrB_2	4.6

mass is about 0.6 m_0.

In the case of the diborides, Piper's experiment on ZrB_2 [14] is most important. He measured magnetoresistance and Hall coefficient of ZrB_2. Estimates were made of the magnitudes of the concentration and mobilities of the carriers using a simple two band model; compensation, i.e. that the electron concentration is equal to the hole concentration, is also assumed. The resultant electron concentration is approximately 0.06 per unit cell and the electron and hole mobilities are about 6×10^{-2} and 2×10^{-2} $m^2/V \cdot sec$, respectively. This low carrier concentration is also supported by the experimental fact that the γ-value of the electronic heat capacity has a relatively low value of about 1 mJ/mole·K^2. Owing to the previous electron transfer theory, ZrB_2 should have two conduction electrons per unit cell, which is doubtful from the above experimental fact due to Piper.

In this study, the measurement of the de Haas-van Alphen (dHvA) effect was used to construct the Fermi surface of LaB_6, ZrB_2 and TiB_2, which would be valuable for formulating better theories of bonding. The dHvA effect is an oscillatory phenomenon of diamagnetic susceptibility of the metal as a function of the static magnetic field. The oscillation frequency is proportional to the extremal cross section of the Fermi surface which is perpendicular to the direction of the applied magnetic field. Thus in Fig.1-4 the section AA' dominates the observed cyclotron period, however, the section BB' not.

The whole shape of the Fermi surface can be examined by the angular dependence of the dHvA frequency on the crystal direction. Expreimental methods for the measurement of the Fermi surface are summa-rized in Table 1-3 along with the information that can be obtained[15]. Every experiment needs low temperature, strong magnetic field and high purity single crystal. The dHvA effect measurement is superior with its relative ease of measurement technique and abundance of information as compared with other methods.

Since the quantization of
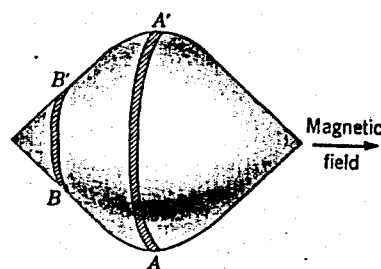
Fig.1-4. Schematic interpretation of the dHvA effect. The orbits in the section AA' are the extremal orbits, but those in the section BB' not.

Table 1-3

Experimental methods for the measurement of the Fermi surface.

Method	Information
dHvA effect	Extremal cross section Cyclotron mass
Cyclotron resonance	Cyclotron mass
Ultrasonic attenua-tion in the magnetic field	Extremal diameter
Magnetoresistance	Extremal cross section Open orbit direction
Radiofrequency size effect	Extremal diameter

the electron orbits should not be blurred by collisions, the

specimens for the dHvA measurement must satisfy the strong

magnetic field condition of $\omega_c \tau > 1$, where $\omega_c = \frac{eB}{m*}$ is the cyclotron

frequency and τ the relaxation time of the electron scatterings.

The scattering centers of the electrons at low temperature are

mainly the crystal imperfections such as impurities, defects,

dislocations, stacking faults and so on. The magnitude of the

cyclotron frequency is limited by the maximum value of the magnetic

field so that the crystal imperfections should be decreased as low

as possible. For example, LaB_6 whose room temperature resistivity

is about 9×10^{-8} Ωm, has the electron mobility of 7×10^{-3} m^2/V·

sec provided the electron concentration of LaB_6 is one electron

per unit cell. The electron mobility at low temperature must be

over 1.7×10^{-1} m^2/V·sec because the maximum field is 6 T in the

present measurement system. The resistivity should be decreased

to less than 3×10^{-9} Ωm at the temperature of the dHvA measure-

ment. For the case of dilute alloys, one atomic per cent of an

element B dissolved in A, gives rise to an extra resistance of

the order of 5×10^{-9} Ωm. If the crystal imperfections in LaB_6

behave like that in the dilute alloys, the concentration of

the imperfections is required to be less than about 0.05 at%

in a rough estimation. Therefore, the control of the crystal

composition and the purification appear as substantial problems

of the preparation of the single crystals.

ZrB_2 and TiB_2 have higher mobilities of the electrons

and holes according to

Piper's estimation. Crystal perfection is not such a severe requirement as in the case of LaB_6.

The shape of the Fermi surface obtained experimentally can be compared with that calculated theoretically from the band structure calculation. Usual method of lending support to the theoretical band structure by the experimental data is the comparison of the theoretical energy distribution curves calculated from the density of states with the measured XPS spectrum. However, the details of the band structure cannot be discussed by such comparison. The dHvA effect measurement gives a direct observation of the electronic structure at the Fermi level. Moreover, the Fermi surface can be determined very precisely; the errors in the measurement of the cross section of the Fermi surface is only about 1 %. Reliability of the band structure calculation can be markedly improved by comparing the calculated Fermi surface with that obtained experimentally. Such a calculation for LaB_6 has been carried out by Hasegawa and Yanase[16] by comparing with the result obtained by the present study, and for ZrB_2 and TiB_2 by Ihara [17]. Regarding their band structure calculations, more detailed discussions have been done not only for the conduction band structure but also for the valence band structure, especially the bonding between the metal and boron has been critically examined, which has indicated in the case of LaB_6 that there are mixings of the B-sp states into the La-d states in the conduction band and of La-s state into the B-sp states

in the valence band; the former spreads the conduction band width, resulting in a light effective mass of the conduction electrons, and the latter causes a covalent character of the M-B bonding in addition to its ionic bonding due to the electron transfer.

It has been found that the dominant bonding in the chemical bond of ZrB_2 and TiB_2 is not the covalent B-B bonding but the covalent metal-boron bonding, resulting in little electron transfer between metal atom and boron atom.

An experimental determination of the phonon spectrum of borides would be useful in understanding their bond nature. An ionic bonding between the positive metal ions and the negatively charged boron framework may cause some effect of the electron-phonon interaction on the electrical resistivity. Thus, the lattice dynamic properties of LaB_6, such as the elastic constant, the heat capacity, the phonon contribution to the electrical resistivity and the lattice thermal conduction, have been discussed consistently using the assumed lattice vibration model.

Chapter 2. Preparation of the single crystal

2-1. Introduction

In the present study, the single crystals of hexaborides (LaB_6, CeB_6, SmB_6, EuB_6 and GdB_6) and diborides (ZrB_2, TiB_2 and CrB_2) have been prepared for studying its electronic properties and bond nature using mainly the dHvA effect measurement. The single crystals of LaB_6 have been also useful for basic research of developping single crystal thermionic emission cathodes. Requisites for the crystals are stoichiometry, high purity, high crystallographic quality and large dimensions. Such requisites are often satisfied by the use of the melt growth methods. Some typical recent examples of the melt growth are summarized in Table 2-1 with its preparation methods[18].

Table 2-1

Some examples of recent single crystal preparation of high quality.

Material	Compound	Preparation method
Laser material	Al_2O_3–Cr, YAG–Nd	CZ
Optoelectronics material	$LiNbO_3$, $LiTaO_3$ $Gd_2(MoO_4)_3$	CZ
Semiconductor	Si, Ge, GaAs, GaP	CZ, FZ(Si)
Magnetic material	$Gd_3Ga_5O_{12}$, YIG	CZ

CZ:Czochralski method, FZ:Floating zone method.

Most of the single crystals have been prepared by the Czochralski method using high purity raw materials. However, LaB_6 and other borides are an unfamiliar non-oxide compound having high melting temperature so that high purity raw material was not available commercially. It is necessary to purify the crystal during the crystal growth process. Zone melting is suitable for purifying the crystal by repeating the zone pass which is the so-called zone refining process. Because of the high reactivity of molten LaB_6, there are no crucible materials. The zone melting applicable to LaB_6 is only the floating zone method in which a molten zone is held in place by its own surface tension between two vertical collinear solid rods.

Many problems would occur when high melting point compounds are prepared using the floating zone method. They are class-ified into two groups; (1) technical problems of forming and keeping the molten zone at temperature above 2500°C, and (2) distribution problem of constituent atoms and impurity atoms at the crystal-molten zone boundary. The problems belonging to the former group are:

(1) Strong power concentration is necessary to raise the temperature above the melting point at the molten zone.

(2) The molten zone must be kept stable during every zone pass of the repeated zone refining.

(3) Vaporization from the molten zone needs to be suppressed as much as possible.

The latter problems are

(4) What chemical composition do the crystals have after

the repeated zone refining?

(5) How many times should the molten zone pass to purify

the crystal enough for the present purposes?

The third problem relates also to the latter group. Vaporization

of constituent elements and impurities may change the composition

and the impurity concentration of the molten zone.

As far as the author could find, there was no example in

which the purification by the repeated zone refining was

successfully applied to such high melting point compounds as

LaB_6. The difficulty is mainly due to instability of the molten

zone under strong power concentration.

To avoid the former technical problems, some investigators

[19-21] prepared the single crystals of LaB_6 at relatively low

temperatures by making use of flux growth, chemical vapor

deposition and fused-salt electrolysis methods. In the first

case, Aita et al.[19] obtained LaB_6 crystals by slow cooling

method using molten aluminum as the flux. The maximum dimension

of the crystals thus obtained was approximately 2-3 mm. The

crystals contained impurities of Fe, Mn, Si and Al of 50-100 ppm.

The solubility of LaB_6 in Al flux is low, for example, it is

0.5 mole% at 1300°C[24], so that it is difficult to prepare a

larger crystal than that described above. Koltz[20] and

Niemyski and Kierzek-Pecold[21] prepared the LaB_6 single

crystals using chemical vapor deposition method. The former

used halogens as a transport agent. The crystals were about 0.15 x 0.15 x 2 mm^3 in size. The latter authors also prepared cubic crystals with sides up to 1 mm in length by reacting gaseous BCl_3 and H_2 with solid La_2O_3 to form gaseous products that decomposed at higher temperature region to give the LaB_6 crystals. Fused-salt electrolysis which is of potential interest for industrial production, is rather similar to the flux growth method when it is adopted as the preparation method of single crystals, because the crystals are deposited from the solutions of boric oxide, metal oxide and halide salts. Zubeck et al.[22] and Elwell et al.[23] grew single crystals with edge dimensions up to 5 mm using seeding method. However, the composition of the crystals differed from the stoichiometry and the quality of the crystals was not so good judging from their appearances. These methods certainly have an advantage that the growth temperature is considerably low as compared with the melt growth. However, the crystal dimension thus obtained is small in every case. Moreover, if one wishes to control the distribution problems of the constituent atoms and impurity atoms, their control parameters would increase as compared with the melt growth method. It is difficult to prepare stoichiometric and high-purity single crystals by these methods which would not be profitable for preparing the single crystals suitable for the present study.

Curtis and Granffenberger[25] and Niemyski and Kierzek-Pecold[21] tried the floating zone method using induction

heating. Eddy current concentrator was used for both cases
to achieve strong power concentration. Evaporation products
were blown off by rapid gas flow, which prevented the evapora-
tion products from adhering to the eddy current concentrator.
Both experiments were restricted to single zone pass only,
moreover, their zone-passed rods consisted of large grains
with average dimensions of about 6-7 mm. Probably it was
caused by the instability of the molten zone. According to
measurements by Curtis and Granffenberger, the surface tension
of the molten LaB_6 is 0.2 N/m. The value is about one tenth
of that of molibdenum and tantalum metals whose melting points
are of the same order of magnitude as that of LaB_6. Large
single crystals of silicon have been prepared industrially by
the floating zone method. The surface tension of Si is about
three times that of LaB_6 and the melting point of Si is only
1430°C. It must be difficult to keep the molten zone of LaB_6
stable under the strong rf field.

Curtis and Granffenberger reported the effect of the zone
refining on LaB_6. In their crystal, the impurity concentration
of the initial part of the crystal was reduced about one
order of magnitude than that of the final part. If multiple
zone refining can be applied successfully, the crystal purity
will be improved markedly.

The floating zone method used in the present study was
carried out under a pressurized gas atmosphere to prevent the
vaporization from the molten zone. Purification by repeating

-22-

zone refining succeeded in finding a stable shape of the

molten zone. The following subjects were mainly examined.

    (1) Method of preparation of the sintered rod for the
        floating zone method.

    (2) Stable shape of the molten zone.

    (3) Atmospheric pressure and the vaporization.

    (4) Chemical composition of the crystals after multi-
        zone passage.

    (5) Purity and the number of times of zone refining.

    (6) Growth direction and the crystallographic quality
        of the crystals.

Each subject will be discussed in the later sections. Here

let us make a brief mention of the results. For LaB_6, it was found

that the stable shape of the molten zone is funnel-like. Zone

refining can be repeated constantly three times, nevertheless

frequent and very delicate power control was necessary. The

purity of the crystals after 3-fold zone refining was improved

markedly to a level never achieved by previous invetigations.

The chemical composition of the crystals was confirmed to be

stoichiometric after 3-fold zone refining. The zone passed

rods were almost always single crystals from top to end of

the rods.

Single crystals of rare-earth hexaborides and transition

metal diborides were prepared also by the floating zone method.

These hexaborides can be classified into two groups of phase

relation. The one is congruently melt compounds and the other

is incongruently melt compounds. Single crystals of the former
group were purified by multi pass of the molten zone without
destroying the stoichiometry of the crystal. This is also the
case of LaB_6. Usually, the melt growth of crystals has been
applied only for congruently melt compounds. In the present
study, the single crystals of the latter group compounds
were grown using a suitable molten zone composition which can
coexist with the compound. Transition metal diborides have
nonstoichiometric regions. Stoichiometry of the crystals of
the transition metal diborides was also controlled by adding
excess boron to the raw powders.

2-2. Melting behavior in the floating zone method

Pfann[27] defined zone melting(ZM) as a method which can
control the distribution of impurity concentration along a
crystal rod. Consideration of the freezing phenomenon of
ZM at the solidus-liquidus interface where the crystal is
growing from the molten zone, should be based on Fig.2-1.
The figure shows a portion of the phase diagram for a binary
system as the melting point of an element A is lowered by an
impurity B. At the initial stage of ZM, if the concentration
of B in the feed rod is C_L, the molten zone can be formed
slightly above at temperature T. When the molten zone begins
to travel, the crystal grows having the impurity concentration
of C_S. As the molten zone successively travels, both the
concentrations of B in the molten zone and in the growing

-24-

crystal increase as shown in Fig.2-1 since the concentration
of B in the feed rod which melts in the molten zone is
higher than that in the growing crystal. Finally a steady
state is achieved when the concentration of B in the growing
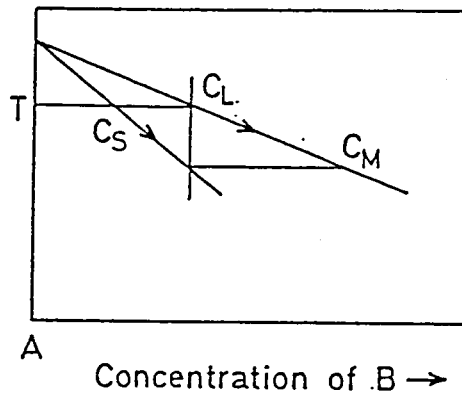
Fig.2-1. Phase diagram in which the
freezing point of the solvent is
lowered.

crystal coincides with that
in the feed rod, then the
molten zone has the concen-
tration of C_M. This state
is called "zone leveling (ZL)
condition". In the above
situation, the following
conditions are assumed, (1)
the diffusion of constituent
atoms is negligible in the

Fig.2-2. (i) Typical phase relations of the two component system.

(ii) The composition relation in the FZ system.

feed rod and the growing crystal and (2) the equilibrium is nearly achieved at the boundary between the molten zone and crystal.

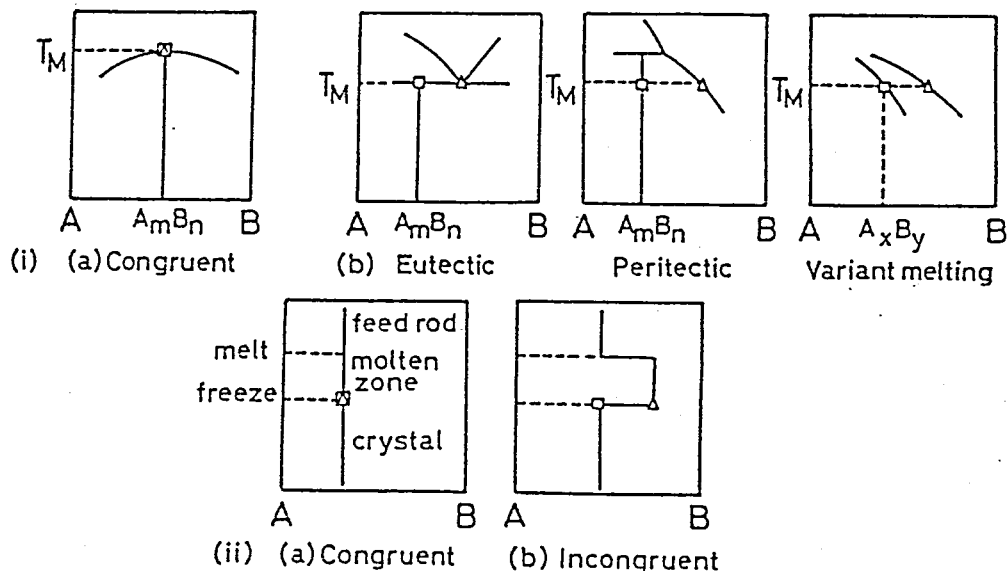For the case of floating zone of compounds, this basic idea can be applied to the distribution between the components of the compound at the crystal-molten zone boundary. Some typical phase relations of the two component system (A,B) are shown in Fig.2-2, where (i,a) shows a congruently melt compound and (i,b) shows incongruent ones of eutectically, peritectically and variant melt compounds, respectively. The crystal composition of A_mB_n or A_xB_y and the liquid composition which can coexist with the crystal are designated by square and triangular marks, respectively. In the case of the congruently melt compounds, the composition of the crystal and the molten zone composition coincide each other so that the floating zone can be done in the same manner as that for the single component. On the other hand, it is necessary to establish the ZL condition in order to apply the floating zone for the incongruently melt compounds. That is, the feed rod composition and the molten zone composition need to coincide with the compositions marked by square and triangular signs, respectively. The composition relation between the feed rod, the molten zone and the crystal are shown in (ii) for both the congruent and incongruent cases.

Spear[4] summarized the melting behavior of the rare-earth hexaborides using the reported data. The rare-earth metals

that form hexaboride phases can be divided into two groups:
the first group includes La through Eu, and the second group
Gd through Yb. The hexaborides of the first group melt
congruently at the stoichiometric composition.

The hexaborides of the second group melt peritectically
to give tetraboride and liquid. According to those melting
behavior, hexaborides of La, Ce, Nd and Sm must be purified
by repeating the zone refining without destroying stoichio-
metry of the crystal. The purification mode on EuB_6 is the
same, though a gas phase product is accompanied by decomposi-
tion. The GdB_6 crystals can only be grown by floating zone
by achieving the ZL condition.

The phase diagram[28] of transition metal diborides
show that they have nonstoichiometric region and have a melting
behavior of variant melting except for congruently melt
composition which seems to differ from the stoichiometric
composition to boron deficient one. It is necessary to achieve
the ZL condition to grow the stoichiometric crystals of
transition metal diborides.

The single crystal preparation under the ZL condition
becomes much more difficult. There will be a region of laminar
flow very near the interface where the velocity of flow is
so small that diffusion is the primary means of transporting
excess component away from the growing crystal. Beyond this
region which is called the diffusion layer, transport by
fluid motion dominates. Thus, the growth rate should be

lowered sufficiently as the excess component can diffuse out
through the diffusion layer, and the crystal rotation is
effective to reduce the thickness of the diffusion layer by
stirring the molten zone. Volume change of the molten zone
causes the composition change of the molten zone, resulting
in the appearance of some other phase or a fluctuation of
the composition of the crystal.

2-3. Apparatus

Since the hexaborides and diborides have very high melt-
ing points above 2500°C, the floating zone of them accompanies
a violent vaporization from the molten zone. It is possible
to suppress to some degree the vaporization by using a
pressurized ambient gas atmosphere. Haggerty et al.[29]
asserted that the vaporization rate from the molten zone is
suppressed to a rate of $1/\sqrt{P}$, where P is the ambient gas
pressure.

Furthermore, the pressurized gas atmosphere served to
suppress an arc discharge between the turns of the rf induction
coil on which strong rf power is concentrated. So the
apparatus used for floating zone method is a high pressure
type furnace of Arthur D. Little Inc. as shown in Fig.2-3.
The furnace can be pressurized to 10^7 Pa(max.). Maximum
heating power is 40 kW. The furnace is applicable to the
three modes of the floating zone method, the Czochralski
method and the Bridgeman method by a suitable combination

of driving mechanisms set in
the upper and lower parts of
the furnace. As can be seen
in Fig.2-3, the rf power is
supplied from the left side
port under which the vacuum
line is set to be used for
gas replacement. There is a
view port at the right side
of the furnace from which the
experimenter observes through
a thick heat-treated glass.
The setting of the sample can
be done from the front port.
The furnace and the moving
shafts are water-cooled.
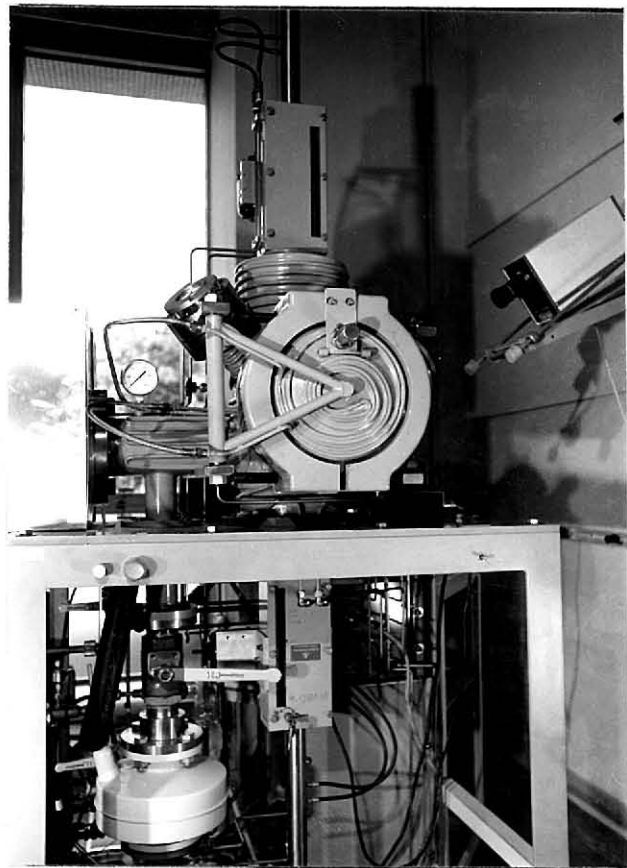
Fig.2-3. High pressure type
furnace of Arthur D. Little
Inc. used for FZ experiment.

This furnace had a weak point for the use of the floating zone
mode. The furnace should be equipped with both synchronized
moving mode and especially differential moving mode in order
to control precisely the molten zone shape. However, the
furnace did not have the differential mode. Moreover, the
moving speed was controlled by supplying a constant power
to driving motors. Such a system has less reliability and
stability of the drive speed. Thus the speed control systems
of the furnace were improved as shown in Fig.2-4. The
rotation speed of the driving motor was detected by a tacho-

Drive shaft

Fig.2-4. Block diagram of the improved speed control system.

meter whose output was compared with a reference voltage by a differential controller. The differential controller supplies a co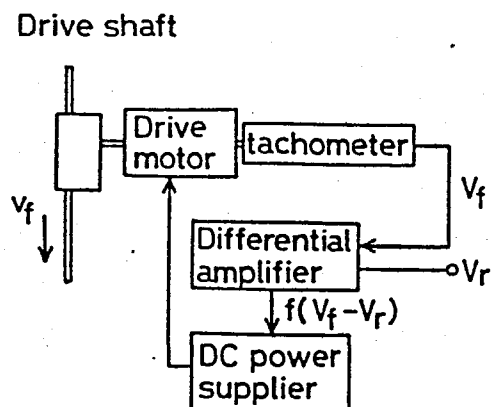ntrol signal to a dc current supplier of the driving motor corresponding to the difference between the output of the tachometer and the reference voltage. Owing to this feed back circuit, the driving motor rotates always correctly at the constant speed corresponding to the reference voltage. Thus the accurate speed control can be achieved by calibrating the relation between the moving speed and the reference voltage beforehand.

2-4. LaB_6

LaB_6 single crystals were prepared by the floating zone method in an ambient Ar gas pressure using rf induction heating. The preparation of the polycrystalline rods for the floating zone method and the multi-float zone pass process will be described next, followed by the results concerning the character- ization of the crystals.

2-4-1.   Preparation of the polycrystalline rods

It is one of the keys for the successful float zoning

-30-

to prepare a straight polycrystalline rod of uniform density. The polycrystalline rod requires a dimension of at least about 10 mm diameter and 150 mm long. However, it is a difficult thing to prepare such a long rod since LaB_6 has a very high melting point and is a poorly sinterable material due to its covalent nature of the chemical bonds. A method of preparing the polycrystalline rods was developed at the begining. The following methods were examined.

(1) Arc-melting the LaB_6 powder which is filled in a water cooled copper boat.

(2) Hot-press method.

(3) Sintering the compact rod shaped by cold press.

    (a) Hydrostatic press of a rubber pipe containing LaB_6 powder.

    (b) Hydrostatic press of a compact rod of LaB_6 shaped cyclindrically after die-press.

The polycrystalline rod obtained by the first method had many cracks owing to a steep temperature gradient around melted region. For the second case when the LaB_6 powder was uniaxially pressed along the long axis of the rod, the density variation increased in the hot-pressed rod. For the cold-press method, it is necessary to fill uniformly the LaB_6 powder in the rubber pipe or the die. This problem increased in the method (3a) more than in the method (3b). As a result, troubles may be least in the method (3b) so that

it was selected.

Powder materials of LaB_6 were purchased from Cerac Inc. and/or Herman C. Starck Inc. The nominal purity was 99.9 % up. The powder size of the former was under 325 mesh and that of the latter was 8 μm average. Since Cerac powder was too coarse to compact into rods, it was ground by a planet-type high speed ball-mill of stainless steel with stainless steel balls to a mean powder size of 4 μm. Contamination from the stainless steel was leached out by boiling in HCl/ethanol= 1/1 solution.

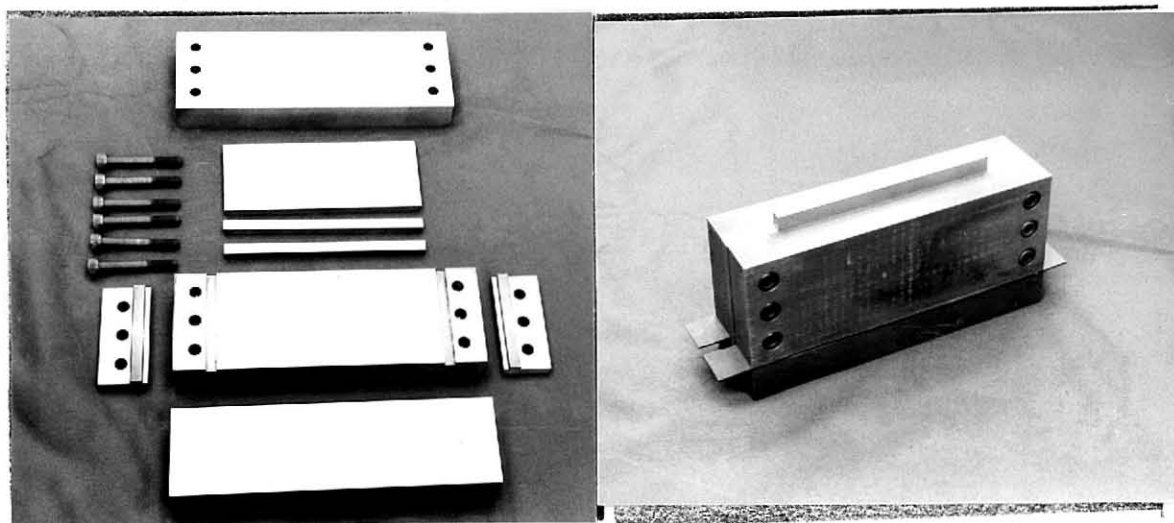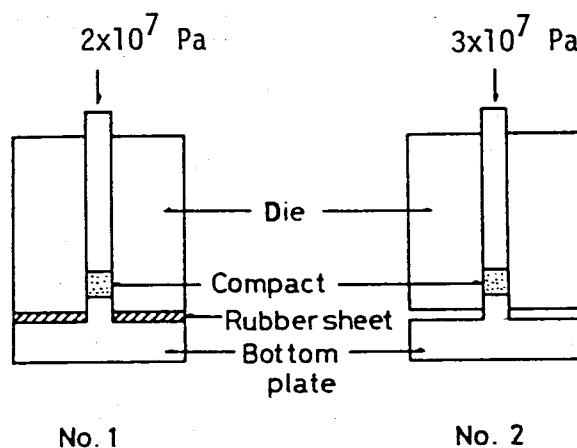Fig.2-5. Convertible die for obtaining uniform compact rod.

A convertible die which is shown in Fig.2-5 was made such that the die can be filled easily and uniformly with the LaB_6 powder and a compact rod of 10 x 10 x 200 mm^3 can be taken out easily from the die. Sometimes camphor was added as a binder. Usual binders for oxide powder could not be used for the LaB_6 powder because such binders can be removed

only by the oxidation. At early stages, a solid paraffin solved in chloroform was used instead of camphor, however, it caused a carbon contamination of the sintered rod. On the other hand, camphor sublimates with a very high rate so that carbon does not remain in the sintered rod.

The density and the cross section of the polycrystalline rod need to be as uniform as possible. The powder compacting procedure used in the present study was rather complicated; at first, a rubber sheet was inserted between the die and the bottom plate and the powder was pressed at 2×10^7 Pa, but the pressure applied to the lower part was decreased by the friction between the powder and the die. Then the rubber sheet was removed and the compact was pressed again at 3×10^7 Pa under a friction free condition as shown in Fig.2-6. Finally, the compact was isostatically re-pressed

Fig.2-6. Process of die-press for obtaining uniform compact rod.

9.5×10^7 Pa in a rubber bug to obtain uniform density. This procedure prevents the compact rod to bend during sintering. All processes were carried out at room temperature.

The compact rods of LaB_6 were sintered using a graphite susceptor heated by induction heating under 1.5×10^5 Pa

Ar gas atmosphere
for 0. 5 h at 1900°C.
Any direct touch of
the LaB_6 rod to the
graphite susceptor
was avoided by boron
nitride spacers.
The polycrystalline
rod thus obtained
had about 73 % of
the theoretical
density. A schematic
diagram of the
sintering furnace
is shown in Fig.2-7.
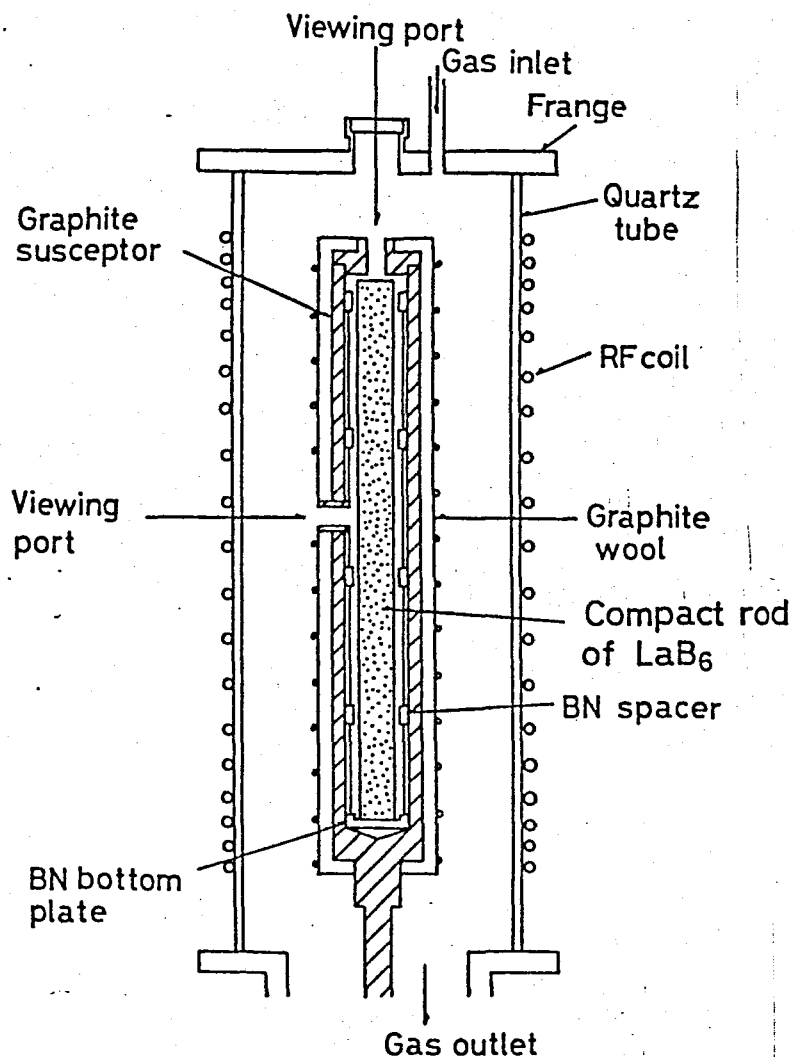
Fig.2-7. Schematic diagram of the sintering furnace.

2-4-2. Flaoting zone

    The crystals of
LaB_6 were prepared
by the floating zone method in an ambient Ar gas pressure
of 5-30 x 10^5 Pa. The polycrystalline rod was heated by
direct induction heating with a frequency of 200 kHz. The rf
coil used was 2 turn x 2 step coil with inner diameter of
about 14 mm as shown in Fig.2-8.

    The polycrystalline rod was inserted in the rf coil and
melted. The feed rod and the growing crystal were driven

-34-

downwards with a speed of 5-20 mm/h. As a consequence of
the passage of the molten zone a single crystal was obtained.
In the subsequent zone passes, the last zone-passed crystal
was used as a feed rod and the process was repeated to
purify the crystal of LaB_6.

The zone pass for
LaB_6 was very difficult,
especially for the case
of the repeated zone
pass. Heating power
needs to be controlled
always. Unless the heat-
ing power is controlled,
after a while the molten

Fig.2-8. Work coil for floating zone method.
It is made by water cooled copper pipe of
3 mm outer diameter.

zone will certainly over-melt or freeze even if it was stable
just after the last power control. Increase (decrease) of
the diameter of the molten zone makes the matching between
the coil and the molten zone better (worse), leading to
more (less) power input to the molten zone. Therefore,
instability of the molten zone is amplified. A stable
condition of the molten zone was sought along the following
analyses.

Zone length: The stability of the molten zone has been
analyzed mathematically and the results have received ample
experimental verification. Heywang and Zeigler[30] and later
Heywang[31] showed that the maximum length l_m of the zone

-35-

supported by its own surface tension approaches a limit at
large radii of the molten zone. The value is

$$l_m \simeq 2.8\sqrt{\gamma/\rho g}$$

where ρ denotes density, g the gravitational constant and
γ the surface tension. The maximum length of the zone of
LaB_6 is estimated to be about 5 mm. However, practical
zone length was about 7 mm. It was impossible to depress the
zone length to below 5 mm when the molten zone was formed,
because the induction coil must fit the charge as closely as
is feasible to concentrate the induced power in a short
region of a vertical rod. This requirement poses a problem
of zone-length control. This is one reason that the zone
pass for LaB_6 is difficult.

Zone shape: There is a difference of the zone stability
between the first pass and the repeated case. Heating
power is necessary to control at least within the time
interval of about 10 minutes for the former case and of
3-4 minutes for the latter case. Kobayashi[32] discussed
the relation between the heating power and the zone shape.
The relation is classified by the Biot number H which is
defined by

$$H = \varepsilon \sigma T_m^3 / \lambda_s ,$$

where ε is the emissivity, σ is the Stefan-Boltzmann constant,
T_m is the melting point and λ_s is the thermal conductivity of
the solid. Small H corresponds to the case that the power

supplied to the zone is mainly conducted through the inter-
face to the rods, the heat radiated from the zone surface
being relatively small. Large H corresponds to the opposite
case. For the former case, the zone length increases with
increasing power input. On the other hand, the zone length
remains constant for the latter case, while the zone shape
varies from concave to convex zone boundary toward the zone
with increasing power input. The critical value is $H=0.8/L_p^2$,
where L_p is the zone length measured by the rod radius.
The Biot number of LaB_6 lies close to the critical value of
$H \simeq 0.2$. Therefore both conduction and radiation contribute
to the heat dissipation from the molten zone. For the first
zone pass, at least the feed rod is polycrystalline. The
thermal conductivity of the rod is lowered from that of the
crystal, leading to high Biot number. In fact, the zone
length does not change so much when the power input changed.
For the repeated zone pass even the feed rod is a crystal,
the contribution of conduction plays larger part than the
first pass. The zone length changed markedly when the power
input changed, making the repeated zone pass more difficult
than the first pass.

Levitation effect: In addition to the surface tension,
there is another force acting on the molten zone, that is
a repulsive force which accompanies induction heating.
Repulsion between the current in the coil and the induced current
in the zone can make the molten zone unstable, particularly

if the coil is above the center of the molten zone.

However, the molten zone can be centered above the coil

and a levitation will be achieved, which helps to support

the molten zone[33]. By cooling the lower rod, for example,

this effect can be achieved[34].

By many trials of float zoning, it was found that the

difference of the zone stability between the first zone pass

and the repeated zone pass is partly due to this levitation

effect. As shown in Fig.2-9(a), for the first zone pass the

(a)   (b)
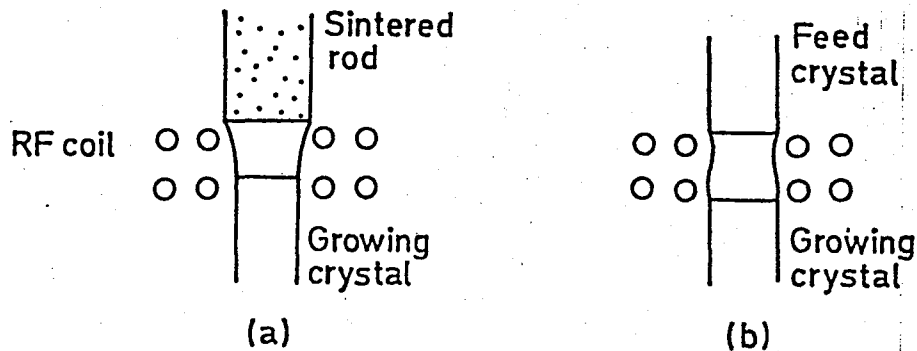
Fig.2-9. Configuration of the rf coil and the molten zone.

(a) First zone pass case. The feed rod shrinks when it is

melted. The molten zone is centered above the coil.

(b) Repeated zone pass case with equal moving speed for

both the feed rod and the crystal.

sintered rod shrank when it was melted. Since the sintered

rod has a larger diameter than the crystal, it is more

effectively heated. Upper and lower zone boundaries lie

slightly above the top surface and the bottom surface of

the coil, respectively. Such a molten zone is supported by

the levitation force. On the other hand, for the repeated

zone pass the zone shape is almost cylindrical(Fig.2-9(b)),

-38-

if both the feed rod and crystal rod are driven with equal

speed. Upper and lower zone boundaries lie close to the top

surface and the bottom surface of the coil. The levitation

effect does not act on such a molten zone. One way to

achieve this effect for the repeated zone pass is to shape the

molten zone similarly to that of the first zone pass.

Stable zone pass: In order to repeat the zone pass stably,

suitable configurations of the coil and the moving speed were

sought following the above considerations.

Configuration of the coil: The work coil must have abilities

of superior power concentration, narrow heating range and

effective levitation. The coils which were examined are

shown in Fig.2-10.
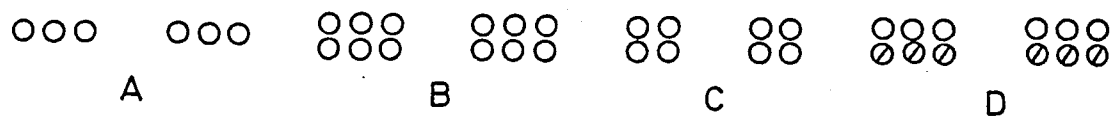
Fig.2-10. Configuration of the rf coils examined. The coil

D is turned in the opposite direction between two steps.

The coil A is a 3 turn x 1 step coil. The coil A was expected

to make a thinner molten zone than other coils. However,

when the molten zone was formed, the zone length was practica-

lly the same for all coils. Moreover, this coil is asymmetric

because one end of the coil must be led out from the center

of the coil, causing the zone boundary to incline and the

molten zone unstable. The coil B and C are 3 turn x 2 step

or 2 turn x 2 step coils. Superior power concentration is

obtained by the coil B. However, the levitation effect by

the coil B became sometimes too strong. Then the molten

zone was blown up. The power concentration and the levitation

effect by the coil C was moderate. The coil D is a 3 turn x

2 step coil also but turning directions of the two steps

are opposite. Wroughton et al.[33] reported that this type

of the coil floated conductive materials between two steps

by the levitation effect. However, when the coil was

energized to form the molten zone, the coil was often

destroyed by discharge between the turns of the coil. Thus

the coil C was selected.

Moving speed: The zone shape is desirable to be funnel-

like even for the repeated zone pass as mentioned above

(Fig.2-9(a)). The moving speed v_f of the feed rod was lowered

than that of the growing crystal(v_g). Suitable value of the

ratio v_g/v_f ranges within $1.1 \sim 1.2$. For larger values of v_g/v_f,

the zone shape differed so much from the flux of the electro-

magnetic field. The repulsive force between the induced

current and the coil current acts to change the zone shape.

The zone stability was destroyed.

It seemed that there is another stable region at about

$v_g/v_f = 0.8 \sim 0.9$. In this case the diameter of the lower

crystal is larger than that of the upper feed crystal. The

molten zone is supported by the lower crystal. However,

the repulsive force acts on the molten zone to blow down so

that a small amount of the molten zone spills down often and

adheres to the crystal at just below the zone boundary. On repeating the floating zone with setting v_g/v_f=1.1∿1.2, the crystal diameter decreases with every zone pass. If the crystal diameter is so different from the inner diameter of the coil, the molten zone becomes unstable as well. As long as another coil having a smaller inner diameter is not used, 3-fold zone pass is the limit. For further zone pass, it is necessary to set the speed relation to be v_g/v_f=0.8∿0.9. However, for the present purpose of the measurement, the 3-fold zone-passed crystals had sufficient purity.

Other effects: Rotating the crystal improves the symmetry of the zone boundary. However, if the alignment of the crystal rod with the rotation axis failed, evidently the molten zone becomes unstable. Since the stability of the molten zone of LaB_6 is very fragile, it is not desirable to add a new instability factor of the molten zone. The crystal rotation was not used for most cases.

Ambient gas pressure was changed from 5×10^5 Pa to 3×10^6 Pa. In spite of the assertion by Haggerty et al.[29], no appreciable difference was observed for the amount of the vaporized LaB_6. If the floating zone was carried out at 5×10^5 Pa, the vaporized LaB_6 adhered tightly to the furnace wall, it becoming difficult to clean up the furnace wall after the floating zone. On the other hand, when the gas pressure was raised to 3×10^6 Pa, convection of ambient gas became considerably violent. It seemed as if the molten zone flickers, which caused a difficulty for

recognizing whether the molten zone is stable or not. Therefore the gas pressure was usually set at 1.5×10^6 Pa.

So, standard conditions for the single crystal preparation of LaB_6 are as follows:— Ar gas pressure of 1.5×10^6 Pa, the growth speed of 10 mm/h(2.8×10^{-6} m/sec) and the number of the zone refining of 3. Rotation of the growing crystal was not applied usually.

The crystal growing system is shown schematically in Fig.2-11 and the actual view of the floating zone experiment through the view port is shown in Fig.2-12, where the lower view is as observed by a mirror which is seen at the left side of the figure.
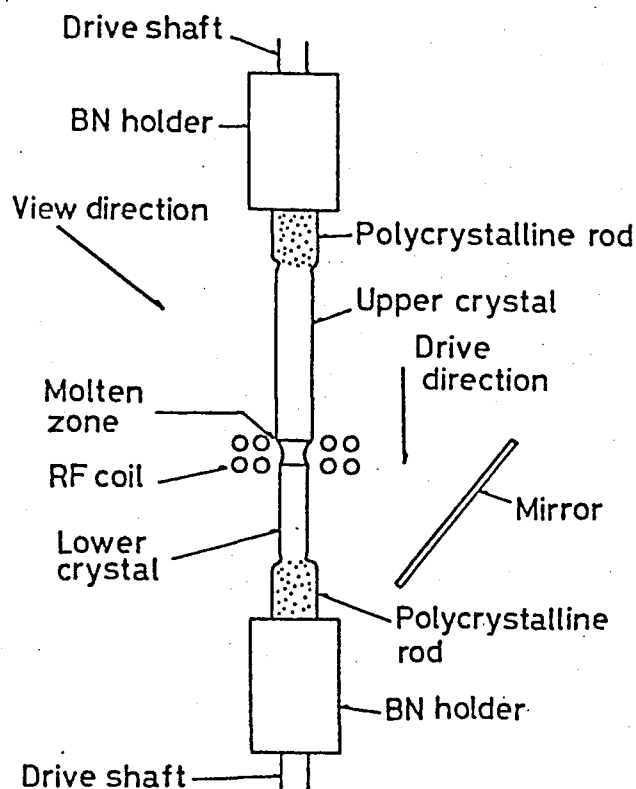
Fig.2-11. Schematic drawing of the floating zone system.

Fig.2-12. Floating zone
experiment observed
through view port.

2-4-3. Quality evaluation

As grown crystal has a fascinating purple color. One of
the crystals thus obtained with about 7 mm in diameter and 60 mm
in length, is shown in Fig.2-13. The growth direction was not
pre-determined by using a seeding method and was dependent on
the initial spontaneous nucleation. The [111] direction was most
frequently observed as a growth axis. However, other growth
directions were also often observed.

Fig.2-13. Photograph of the as-grown LaB_6 crystal.

(i) Stoichiometry

The melting behavior of the La-B system was examined in the vicinity of B/La=6.0. Assuming the composition of the raw powder of LaB_6 to be stoichiometric, boron powder or La_2O_3 powder was added to LaB_6 powder controlling the composition of the sintered rod to coincide with B/La=5.8(No.101), 6.0(No.102), 6.2(No.103) and 6.4(No.104). These powders were mixed for 20 minutes in an agate mortar. After compacting each powder using the same method described in sec.2-4-1, the compact rod was heated up to 1900°C for 30 minutes in vacuum. The sintered rod thus obtained was float-zoned under the condition of the moving speed of 10 mm/h and the He gas pressure of 1×10^6 Pa. Each zone pass was carried out for about 4 hours except the specimen No.104. The molten zone of the specimen No.104 was relatively unstable so that the molten zone was passed only for 1 hour.

Lattice constant, density and chemical composition were measured at positions of the initial(designated I) and final(F) parts of every zone passed rod. The rod No.104 was so short that measurement was restricted only to the initial part. The chemical composition analysis was done also for the solidified molten zone(M) and the sintered rod(S). In the case of No.103, S designates the position of the sintered rod far from the zone passed part and S* the position a little above the solidified molten zone.

The lattice constant was measured by X-ray powder diffraction method with an internal standard of silicon. The ASTM

value of 0.534088 nm was used as the lattice constant of silicon.
The lattice constant of each sample is the average value of
those calculated from six diffraction peaks observed at $2\theta > 100°$.

The density measurements were carried out using hexachloro-
1,3-butadiene as a buoyancy medium of good wetability. High
purity single crystal of silicon was used as a density standard.
The value is 2.330×10^3 kg/m^3. The results of three measure-
ments were averaged.

Table 2-2

Chemical composition, lattice constant and density of LaB_6 single
crystals after zone pass through the sintered rods having
different chemical composition.

Sample	Position	C_{La}(wt%)	B/La	Lattice const.(nm)	Density(10^3kg/m^3)
101	I	68.1	6.02	0.41567±0.00001	4.707±0.003
	F	68.1	6.02	0.41566±0.00001	4.714±0.003
	M	70.4	5.41	–	–
	S	68.2	5.99	–	–
102	I	68.1	6.02	0.41567±0.00001	4.707±0.002
	F	68.2	5.99	0.41569±0.00001	4.714±0.002
	M	70.2	5.45	–	–
	S	67.2	6.25	–	–
103	I	68.1	6.02	0.41569±0.00001	4.714±0.004
	F	68.2	5.99	0.41566±0.00001	4.708±0.004
	M	69.8	5.56	–	–
	S*	65.0	6.74	–	–
	S	67.0	6.32	–	–
104	I	68.2	5.99	0.41569±0.00001	4.714±0.004
	M	68.6	5.88	–	–
	S	66.8	6.38	–	–

Only the La content in the crystal was analyzed and the residual part was assumed to coincide with the boron content because the impurity concentration of the crystals was very low as will be mentioned later. The single crystal was crushed to powder using tungsten carbide mortar. The crushed powder was sieved and the particles were put in order between under 60 mesh and over 100 mesh. The powder thus obtained was dissolved into an aqueous solution of chloric acid and nitric acid mixture. The La content was determined by titration of EDTA using XO indicator after adjusting the pH of the solution.

The results so obtained are summarized in Table 2-2. The La content of every sintered rod was equal or smaller than the stoichiometric composition of C_{La}=68.16 wt%, while the sintered rods did not have the expected composition values. These are due to the fact that the raw powder did not have stoichiometric composition as expected, which is shown by the S value of specimen No.102, and that the ignition loss of raw powders was not estimated beforehand.

Storms[35] reported that the lattice constant of $La_{1-x}B_6$ is independent of its chemical composition, having a value of 0.41565 nm. The present author also confirmed the similar evidence of the lattice constant of $La_{1-x}B_6$ which was synthesized by solid reaction of La_2O_3 and B.

There are no appreciable differences between the lattice constants measured for any positions of the crystals. Assuming the lattice constant at the stoichiometric composition to be

the average value of 0.41568 nm, the stoichiometric density is 4.713 x 10^3 kg/m^3. The measured density values almost coincide with the stoichiometric value. Several values are slightly less than the stoichiometric one, which is attributed to micro voids existing in the crystals. There are no appreciable deviations from the stoichiometric values of the chemical composition, the lattice constant and the density. In conclusion, the zone-passed rods have always the stoichiometric composition independently of the chemical composition of the feed rod.

It is curious that the chemical composition of the molten zone is always La rich though the feed rod composition is a boron rich one and the crystal rod is stoichiometric. The following facts were found by observations near the solidified molten zone:—

(1) The part just above the molten zone may be almost stoichiometric because the color of that position is quite similar to that of crystal*.
Chemical analysis of some crystallites showed their composition to be near stoichiometric.

(2) The part a little above the molten zone (designated S* in the specimen No.103) seemed to be infiltrated by some liquid phase. The chemical composition of S* is more boron rich than that of S.

---

*The color of LaB$_6$ is dependent on the conduction electron concentration. It means also that the color of non-stoichiometric La$_{1-x}$B$_6$ is different from that of the stoichiometric LaB$_6$.

(3) No changes were observed at positions more distant from
the molten zone.

These observations can be understood as follows. The compo-
sition of the feed rod is assumed to be a boron rich one. When
the molten zone comes near any positions of the feed rod, it
decomposes peritectically into solid phase and liquid phase.
The composition of the solid phase is close to the stoichiometric
one and that of the liquid is very rich in boron. This liquid
phase infiltrates into the feed rod away from the molten zone,
which causes the chemcial composition of S* being richer in boron
than that of S. The solid phase which is left, melts in the
molten zone. Boron vaporizes preferentially to La, leading
the zone composition to become La-rich.

The same tendency was reported by Takagi et al.[36]. They
prepared thin single crystals of LaB_6 with about 1 mm in diameter
by the laser heating method. The zone-passed crystals contained
small amounts of LaB_4 phase as inclusion. Their crystals were
so thin that the surface to volume ratio of the molten zone is
about one order of magnitude larger than in the present experiment,
causing a larger composition deviation of the molten zone. In
their experiment, the zone composition shifted probably to some-
where near the peritectic point of LaB_4.

It is found that the crystal grown from the molten zone
of the La rich composition has always the stoichiometric compo-
sition as long as the zone composition does not reach the
peritectic composition. Therefore, the repetition of the zone

pass does not change the crystal composition from the stoichio-metric value. In fact, the measured lattice constant, density and chemical composition of 3-fold zone-passed crystals coincided with the stoichiometric values. The measured values were a= 0.41567$\pm$0.00001 nm, ρ=4.712$\pm$0.002 x 10^3 kg/m^3 and C_{La}=68.2 wt%, respectively.

Furthermore in order to check if the ratio of B/La fluctuates from the stoichiometry along and across the growth axis, the concentration of La ion was measured by electron probe micro-analysis. The X-ray intensity from the La ion was about 8.5 x 10^2 counts/sec.

The total counts of 20 sec fluctuate with 3 % when the measure-ments were repeated at the same point. When the measurement points go along and across the growth axis the fluctuation of the total counts ranged within 3 %. The
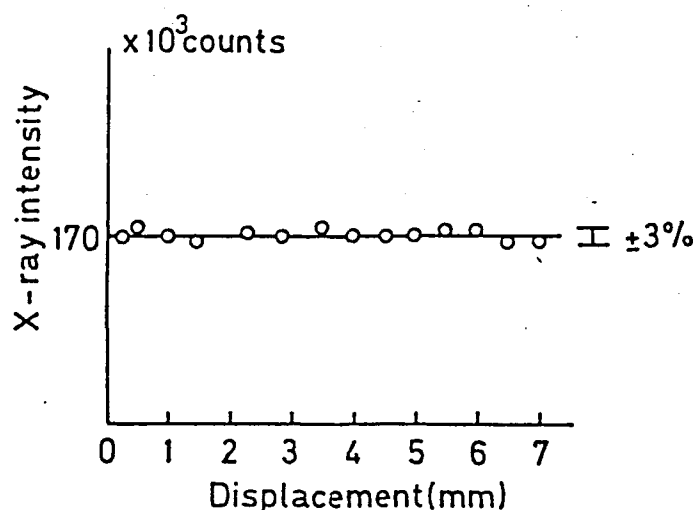

Fig.2-14. The X-ray intensity fluctuation when the measurement points go across the growth direction.

results across the growth axis are shown in Fig.2-14. Thus no appreciable deviation from the stoichiometry has been observed.

There are two other phase diagrams of La-B system in addition to the Spear's one noted in sec.2-2. Johnson and

Daane[37] gave the nonstoichiometric region of LaB_6 to be from LaB_6 to $La_{0.78}B_6$. They did not experiment on the melting behavior of LaB_6 so that the congruently melt composition is unknown. Recently Storms and Mueller[35] carried out a precise study on the phase diagram of the La-B system. They asserted that the congruently melt composition of LaB_6 lies at B/La=6.3 and that the relatively narrow nonstoichiometric region exists. According to their phase diagram, the multiply zone-passed crystal should have the congruent composition of B/La=6.3. The present result does not agree with their assertion. Verhoeven et al.[38] developed a floating zone by arc-discharge heating technique. Noack and Verhoeven[39] reported recently that the densities of their multiply zone-passed crystals coincide with the stoichiometric X-ray density. Nevertheless, the atom ratio of B/La which were analyzed were La rich ones. They suggested that some boron octahedrons may be lacking and that excess La ions substitutionaly may occupy the defects sites of the boron octahedron. However, such a substitution cannot keep the charge neutrality of the crystal. There may be a methodological problem in the composition analysis

The measurement of the electronic properties of the LaB_6 crystals lent support to the fact that the zone-passed crystals of LaB_6 have the stoichiometric composition. For example, if there were many defects caused by the nonstoichiometry of the crystal, the dHvA measurement would be impossible because the scattering of the conduction electrons by the defects would be

an obstacle in satisfying the strong magnetic field condition. Actually the dHvA signal was detected easily using the zone-refined crystals. This situation can be understood more clearly by the residual resistance ratio of the crystals noted in the next section.

(ii) Residual resistance ratio

For evaluating the quality improvement of the crystals of conducting materials, residual resistance ratio(RRR) is a useful parameter. The RRR value is defined approximately by the ratio of room temperature resistance to liquid helium temperature resistance ρ(300 K)/ρ(4.2 K). The room temperature resistance is mainly due to the scattering of electrons by phonons. It is an intrinsic property of the crystal. On the other hand, the low temperature resistance is due to the scattering of electrons by the crystal imperfections such as impurity, defect, dislocation, etc. Large RRR value indicates the overall improvement of the crystal quality, that is, low concentrations of impurity, defect, dislocation, etc. The RRR value of the LaB_6 crystals should increase with the increase in the repetition number of the zone pass. Typical RRR value of the crystals are tabulated in Table 2-3 with its repetition number of the zone pass. The electron mobility of each crystal is supplemented at the last column. The RRR value of 3-fold zone-passed crystals is about an order of magnitude larger than that of the single passed crystal.

In order to observe the dHvA effect, the electron mobility

Table 2-3

Relation between the number of zone pass and the residual
resistance ratio value and corresponding electron
mobility at 4.2 K.

Repetition number of zone pass	RRR value (typical)	Electron mobility at 4.2 K $(10^{-2}$ $m^2/V \cdot sec)$
0 (sintered rod)	3	2.1
1	50	35
2	190	133
3	450 (max. 720)	315 (max. 504)

needs to exceed the threshold value, 1.7×10^{-1} $m^2/V \cdot sec$, of

the present measurement system. The single zone-passed crystal

satisfied this condition already, however, some dHvA oscillations

with a weak signal intensity, were observed only within a

relatively narrow angular region. Using the 3-fold zone-passed

crystal, for example, it became possible to observe the α frequency

even within the weak signal region from 50° to the [111]

direction in the ($1\bar{1}0$) plane.

The RRR value can give a relative evaluation of the overall

improvement of the crystal quality. Each contribution of defect,

impurity, dislocation, etc. cannot be estimated separately.

However, the upper limit of concentration of defects or impurities

can be estimated from the residual resistivity value. The re-

sidual resistivity caused by defect scattering or impurity scatter-

ing is of order of 5×10^{-9} Ωm per 1 at% defects or impurities

for many metals [40]. The residual resistivity of the 3-fold

zone-passed crystals of LaB_6 is about 1×10^{-10} Ωm. The concentration

of defects or impurities can be estimated to be at most of
order of 0.02 at%. There are few examples in literature
in which the residual resistivity due to the dislocations is
estimated. One cannot discuss the dislocation density of the
crystals from the residual resistivity value.

(iii) Impurity

Impurities have been qualitatively or semi-quantitatively
analyzed by emission spectrography. The result is summarized
in Table 2-4. No impurities were detected from the 3-fold
zone-passed crystals prepared using both the Cerac powder and
the Starck powder. The repetition of the zone refining
removed the impurities markedly.

Carbon impurity of 0.6 wt% was detected from the Cerac
powder, but it could not be detected in any zone-passed crystals,
where the detection limit of carbon is 0.04 wt%. Surface
accumulation of carbon impurity from the bulk was observed in
the case of single zone-passed crystals by the flash heating
up to 1300°C several times in a ultra high vacuum chamber[41].
This surface accumulation of carbon impurity is undesirable
in the practical use of LaB_6 as the emission cathode. The work
function of the surface in such state is considerably higher
than that of the clean surface of LaB_6. However, such an
accumulation phenomenon of carbon impurity did not occur for
the 3-fold zone refined crystals. The zone refining process
is also effective in reducing the carbon impurity.

Table 2-4.

Impurity concentrations of LaB_6 raw powders and zone refined crystals analyzed by emission spectrographic analysis.

Zone pass time	Impurities														
	Co	Si	Mn	Mg	Cr	Fe	Mo	V	Ti	Zr	Ni	Ca	Al	Cu	Ba
0(Cerac powder)*	w	w	w	t	vw	w m	m	vw	w	w	m	vw	-	-	-
0(Starck powder)**	50	15	15	<5	150	500	<5	<5	5	5	50	50	15	<5	5
1(Cerac powder)	-	t	t	-	-	w	-	-	-	-	-	-	-	-	-
1(Starck powder)	-	5	5	<5	5	5	-	-	-	-	-	-	-	-	-
3(Cerac powder)	-	-	-	-	-	-	-	-	-	-	-	-	-	-	-
3(Starck powder)	-	-	-	-	-	-	-	-	-	-	<5	-	-	-	-

*vs > s > m > w > vw > t

**semi-quantitative analysis(ppm)

In conclusion, the triple passage of the molten zone increases the purity more than an order of magnitude as compared with the single passed crystals. The purity of the crystals obtained now has been markedly improved as compared with the previous works.

(iv) Crystallographic quality

Etch pits of a cleaved (100) plane appeared on immersing for 30 seconds in the nitric acid solution ($HNO_3/H_2O=1/2$) at 30°C. The etch pit density was of order of $10^4/mm^2$. This order of etch pit density has been often reported for the floating-zoned crystal having melting point above 2000°C. It was also observed that the etch pits formed a line. The etch pit line probably appeared along low angle grain boundaries due to small misalignment of sub-grains. It is known that most of the crystals which are nominaly called "single crystal", consist of sub-grains. Degree of the misalignment ranges from several seconds to degrees. For the case of small misalignment of several seconds, Berg-Barrett photography serves to observe the sub-grains. For larger misalignment the Berg-Barrett photograph cannot be taken and back reflection Laue photograph is better. As shown in Fig.2-15, the observation by Berg-Barrett photograph was possible for the 3-fold zone passed crystal of LaB_6. It was found that the dimension of sub-grains is about 1 mm^3. The misalignments between neighboring sub-grains were estimated to be within several seconds. Since this misalignment
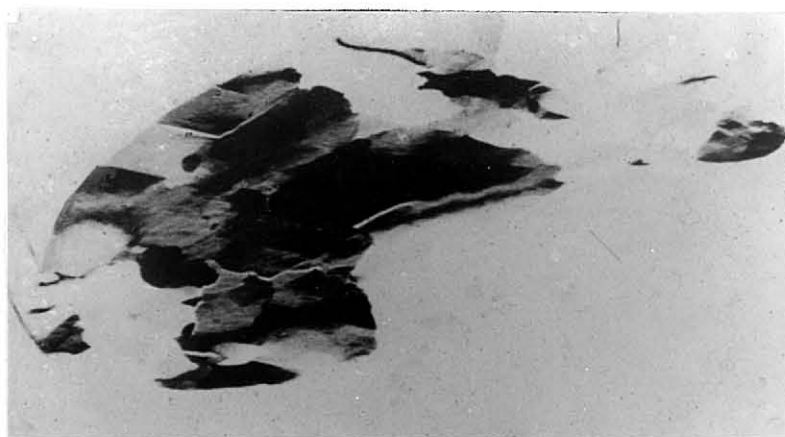
Fig.2-15. Berg-Barrett photograph of the LaB_6 crystal cross section by (211) diffraction.

is very small, we have experienced no troubles caused by the misalignment in the use of the crystals either as thermionic emission cathodes or as specimen for the dHvA measurement.

2-5. Other hexaboirdes

Single crystals of rare-earth hexaborides (CeB_6, SmB_6, EuB_6 and GdB_6) have been prepared by the floating zone method. In principle, the method developed for LaB_6 can be successfully applied to three hexaborides of CeB_6, SmB_6 and EuB_6 since they are congruently melt compounds. But EuB_6 is characteristic with its very high volatilization. On the other hand, GdB_6 is an incongruently melt compound which decomposes into GdB_4 and liquid. The preparation of GdB_6 crystals requires the achievement of the zone leveling condition.

2-5-1. Synthesis of the raw material

These hexaborides are so expensive that it was difficult to purchase the raw materials of them with a sufficient amount for the floating zone experiment. Raw material of 50∿70 g, depending on their density, is necessary for only one experimental

use. Thus the raw materials were synthesized by borothermal-reduction,

$$CeO_2 + 8B \longrightarrow CeB_6 + 2BO$$
$$RE_2O_3 + 15B \longrightarrow 2REB_6 + 3BO$$
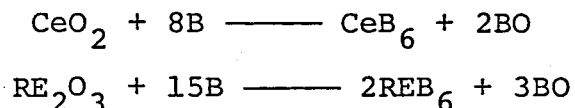
(RE=Sm, Eu and Gd).

Rare-earth oxide powders whose nominal purity are 99.9 %, were purchased from Shin-etsu Chem. Corp. To facilitate the reaction, an amorphous boron powder of 97 % purity which was purchased from Herman C. Sarck Inc., was used. In each reaction, oxide and boron powders were mixed using a plastic ball-mill for about 15 h. Then the mixed powder was pressed into a pellet at 3×10^7 Pa. The reactions were carried out in vacuum at about 1700°C for 1 h using an induction heating furnace with a graphite susceptor. Glow discharge of bluish green color which is characteristic of BO molecule, disappeared after about 0.5 h, indicating that the reaction almost finished at that time. After the reaction, the pellet was crushed in an agate mortar to a coarse powder which was re-ground to a fine powder of mean size of 4 μm by a planet-type high speed ball-mill of stainless steel. Contaminations from the stainless steel were leached out by boiling in dilute HCl ethanol solution. Since GdB_6 is soluble in HCl solution, about 10 % of the synthesized powder was lost by this process. Sometimes the reaction temperature for the GdB_6 synthesis was lowered to about 1500°C and the reaction interval was prolonged. The softly sintered pellet can be ground to a powder of about under 325 mesh only by

using the agate mortar. The GdB_6 powder thus obtained can be pressed into a rod by adding a camphor as a binder.

2-5-2. Preparation of the polycrystalline rod

The preparation method of the polycrystalline rod was essentially the same as that for LaB_6. The powders of hexaborides were die-pressed, followed by the hydrostatic press. The compact rod was sintered at about 1900°C for 0.5 h in the graphite susceptor(Fig.2-7). The sintered rods thus obtained had about 57 % to 63 % of the theoretical density.

2-5-3. Floating zone

CeB_6 and SmB_6: These hexaborides are congruently melt compounds like LaB_6. They have somewhat lower melting points at around 2500°C than LaB_6. The molten zones of these hexaborides were very stable even for the repeated zone passes. This indicates that the surface tension of these hexaborides are considerably higher than that of LaB_6. Probably the difference of melting points is responsible for this problem. The zone pass was easily carried out for the unstable speed region of LaB_6 such as $v_g = v_f$. Therefore, the feed speed and the growth speed were always equal at the value of 10 mm/h. The other operational procedures of the floating zone were pratically the same as those used for LaB_6. Ambient Ar gas pressure was 1.5×10^6 Pa in every experiment.

EuB$_6$: EuB$_6$ is also a congruently melt compound but is so

volatile at the melting point of about 2500°C that it is

difficult to form the molten zone. At the initial stage of

forming the molten zone a violent vaporization occured from the

molten zone. The feed rod was rapidly fed down into the rf

coil to keep the molten zone which tends to shrink by the

vaporization. However, after a few minutes the vaporization

gradually decreased. Then the floating zone was started with

setting a speed of the upper feed rod to 20 mm/h and the growing

speed of the lower crystal to 15 mm/h. This difference of the

speeds is necessary to compensate the vaporization loss.

The vaporization at steady state was not troublesome for the

stable zone pass. The 2-fold zone pass was tried for EuB$_6$.

The zone passage was rather easy although the vaporization

did not decrease in this case. Ambient gas pressure was set at

2 x 10^6 Pa. The other operational procedures were the same as

those used for LaB$_6$. When air was introduced in the furnace to

take out the crystal, the powder which vaporized in the furnace

burned explosively. This was also the case for SmB$_6$.

GdB$_6$: According to the
phase diagram of Gd-B
system[4] which is shown
in Fig.2-16, GdB$_6$
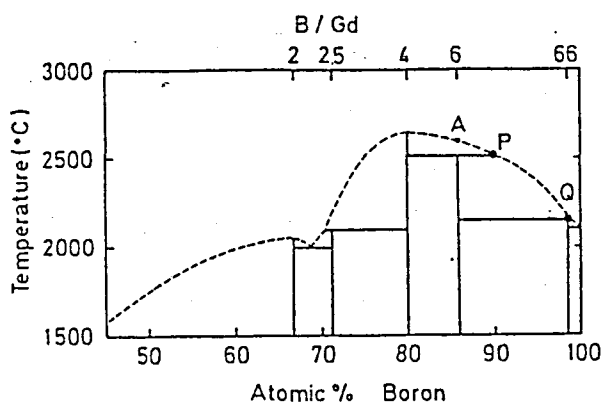peritectically decomposes
at 2510°C. In order to

Fig.2-16. Phase diagram of Gd-B system[4].

apply the zone leveling method, modification of the phase diagram should be made to accomodate to the floating zone method. If the usual floating zone is carried out through the sintered rod of B/Gd=6, the molten zone is formed at point A in Fig.2-16. As the molten zone starts to travel, the GdB_4 phase appears, leading the zone composition to shift from A toward P. After the zone composition reaches P, as long as the zone leveling condition is not destroyed, the GdB_6 phase continues to appear. This estimate was confirmed experimentally. The GdB_4 phase which turns golden luster was recognized in the initial part of the zone passed rod. The remaining part of the rod was GdB_6; however, sometimes the GdB_4 phase was present. It may be caused by the instability of the molten zone. Chemical analysis of the composition of the solidified molten zone determined the composition at P to be B/Gd=7.3 under the floating zone condition. This value is quite close to that of the phase diagram. In using the zone leveling method, the zone pass process requires great care to keep the molten zone composition constant. If the volume of the molten zone changes, the zone composition will change and another phase may appear. For example, if an accidental increase of the heating power re-melts the GdB_6 crystal during the zone pass, the zone composition will shift toward Gd rich composition. If the zone leveling condition was achieved at point P, such a shift of the zone composition causes the appearance of GdB_4 phase. Therefore, the zone composition should be set at about B/Gd=7.5 so as not to exceed the composition at P

by small increase of the zone volume.

In the experiment, the growth speed was lowered to 3.5 mm/h which is about one third of that of LaB_6. The crystal was rotated at 10 rpm. Two modes of the floating zone were tried to establish the zone leveling condition; (1) The molten zone passed through the sintered rod whose composition is B/Gd=6. As mentioned above, after the molten zone passed for a while, the zone leveling condition is established as shown in Fig.2-17(a).
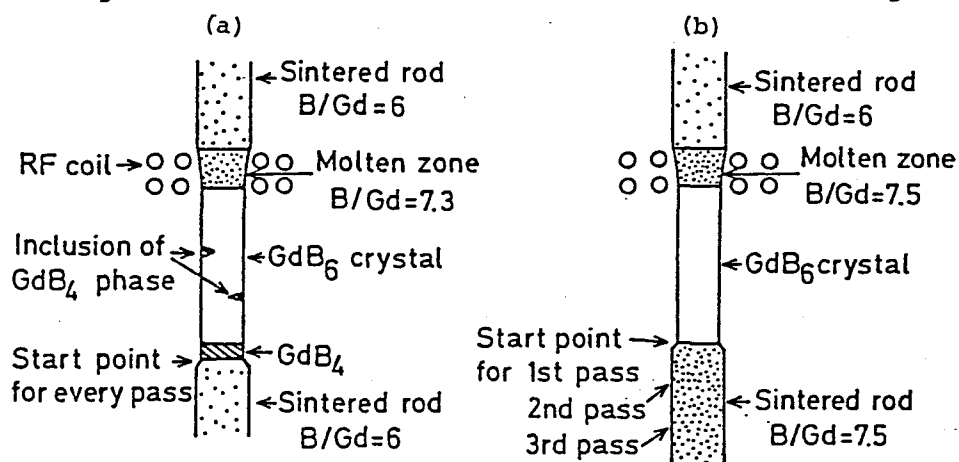

Fig.2-17. Schematic diagram of the zone leveling methods for preparing the GdB_6 crystal.

(a) Usual floating zone method. The molten zone passes through the GdB_6 rod. The zone leveling condition can be achieved after the GdB_4 phase grows.

(b) Molten zone is formed by melting the sintered rod with B/Gd=7.5. The zone leveling condition is already achieved at the starting point.

The zone refining was repeated in the same manner. Single crystal of GdB_6 was cut from the end part of the multiple zone-passed rod. (2) The sintered rod having the composition of B/Gd=7.5 was melted to form the molten zone. The zone leveling condition is established already at the start of the zone pass. Starting

points of repeated zone passes have shifted as shown in Fig.2-17(b).

Both modes are compared in Table 2-5. Zone refining was not so

Table 2-5
Comparison of the two modes of the zone leveling methods to
prepare the GdB_6 crystals.

	1st case	2nd case
Composition of sintered rod	B/Gd=6(both for feed rod and seed rod)	B/Gd=6(feed rod) B/Gd=7.5(seed rod)
Zone composition at the zone leveling condition	B/Gd=7.3	B/Gd=7.5
Starting point of the multiple zone pass	constnat	shifted(see Fig. 2-17(b))
Molten zone of 2nd and 3rd passes	zone passed rod	sintered rod
GdB_6 crystal	end part of the rod	all of the rod
GdB_4 phase	initial part of the rod and sometimes included in GdB_6 crystal region	none

effective for both cases. For the first case, the GdB_6 crystal

had to be cut from the end part of the rod and for the second

case, a new sintered rod had to be used to form the molten

zone in every zone pass. Crystals obtained by the first and

second modes were named as No.901 and No.904, respectively.

2-5-4. Quality evaluation

The crystals of CeB_6, SmB_6, EuB_6 and GdB_6 obtained by the method described, have approximate dimensions of 8 mm in diameter and 30~50 mm in length. These crystals have bluish, bluish black, black with metallic luster and violet colors, respectively. They are shown in Fig.2-18.

(a)

(b)

(c)

(d)
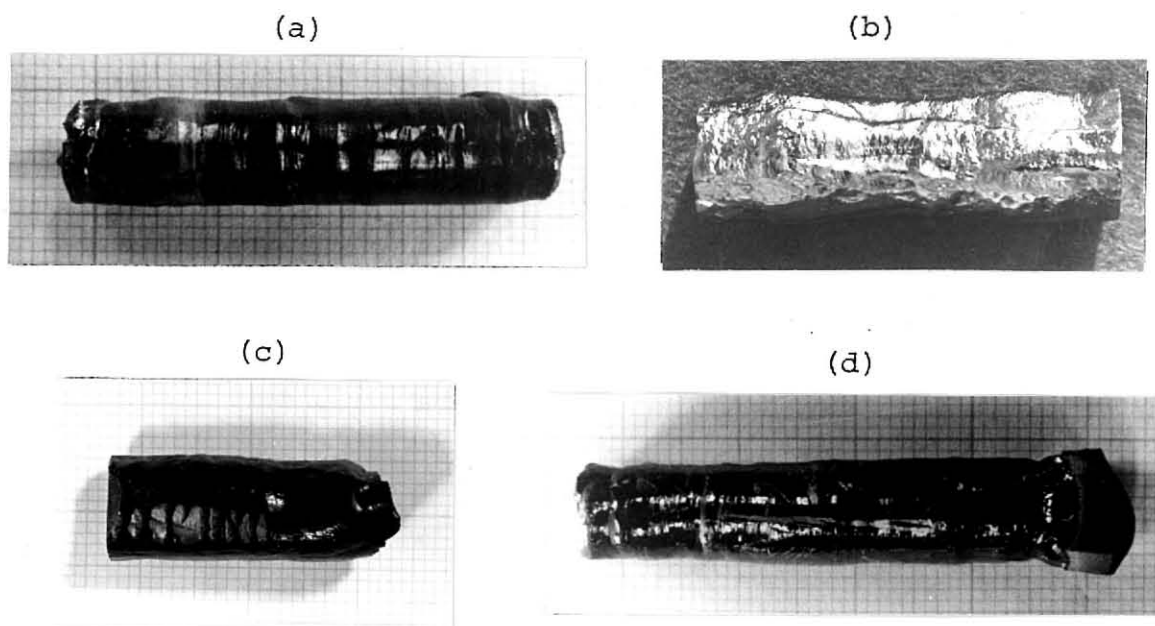
Fig.2-18. Photographs of the rare-earth hexaboride crystals of (a) CeB_6, (b) SmB_6, (c) EuB_6 and (d) GdB_6.

Back reflection Laue photograph showed the growth directions of CeB_6 crystals to be [100] or [110]. The Laue photograph of the core region of the crystals showed a single crystal pattern. However, the spots from the peripheral region showed that sub-grains were formed. The SmB_6 crystal had a rough surface and facets were observed. The growth direction was far from low index directions. The EuB_6 crystal had a rough surface and no

facets or ridges were observed. Fig.2-19 is a section photograph of the (100) plane of the crystal which indicates that the crystal is single crystalline only in the core region of about 6 mm in diameter while the outer side is polycrystalline. The growth direction of the single crystalline domain is about 8° off from the [110] direction. The GdB_6 rod No.901 contained GdB_4 phase and the crystal consisted of several large grains. No.904

Fig.2-19. Section photograph of the (100) plane of EuB_6 crystal.

GdB_6 consisted of a single domain whose growth direction was near [110].

(i) Stoichiometry and impurity of the crystals

The chemical composition and impurity level of each crystal was analyzed by wet chemical analysis and emission spectrographic analysis. The results are tabulated in Table 2-6. In all cases, the chemical compositions have a tendency of boron deficiency. If one considers the bonding nature of the rare-earth hexaborides, it is not likely that there exist boron vacancies. It is probable that the chemical analysis of boron has a tendency to give a slightly lower value than the actual composition, since the sum of the metal and boron contents is always less than 100 %. Another possibility is MeB_4 inclusions, but optical microscope observation did not show the existence of any MeB_4

Table 2-6

Chemical composition and impurity levels of the rare-earth hexaboried crystals of CeB_6, SmB_6, EuB_6 and GdB_6.

Sample	Composition (wt%)		Impurities (ppm)									
	RE	B	Fe	Ni	Co	Mg	Mn	Ag	Pb	Cu	Al	Zr
CeB_6 raw material	–	–	50	–	5	5	–	–	–	5	5	–
3-fold passed CeB_6	68.6 (68.4[a])	30.9	<5	–	5	<5	–	–	–	15	5	–
SmB_6 raw material	–	–	5	–	15	<5	<5	5	<5	–	–	–
4-fold passed SmB_6	70.1 (69.9[a])	29.8	–	–	15	<5	<5	5	<5	–	–	–
Single passes EuB_6	70.2 (70.1[a])	29.5	Traces of Ca, Si and Mo									
GdB_6 raw material	69.2	28.3	50	5	<5	<5	–	–	<5	<5	–	<5
No.901 GdB_6 crystal	70.8 (70.8[a])	27.4	<5	<5	<5	<5	–	–	<5	<5	–	<5
No.904 GdB_6 crystal[b]	70.5	28.4	15	–	<5	<5	<5	–	–	–	–	–

[a]Stoichiometric value.   [b]Free boron was contained.

inclusion except for the GdB_6 crystal No.901. The cation content of every crystal is in agreement with the stoichiometric values within the experimental error except for the GdB_6 crystal No.904. It was concluded that the crystals obtained here are nearly stoichiometric. No.904 GdB_6 contained free boron. The amount

of the free boron is excluded from the composition value in Table 2-6. The ratio of cation and anion of No.904 GdB_6 is comparable with that of the other specimens so that the crystal is nearly stoichiometric. In the case of EuB_6, the crystal density was measured. The measured value of $5.0 \pm 0.1 \times 10^3$ kg/m^3 agrees with the stoichiometric density of 4.94×10^3 kg/m^3 calculated from the X-ray lattice constant. The polycrystalline region of the outer side of the crystal contained inclusions. Except the outer polycrystalline region, there were no fluctuations in the composition ratio B/Eu which was checked by electron probe microanalysis across the (100) plane (Fig.2-19), by measuring the Eu content.

The zone refining process is effective in reducing impurities, especially for the Fe impurity which comes from the milling process. The reason why No.904 GdB_6 has a rather high impurity level is due to the use of the new sintered rod to form the molten zone in every zone pass. Rare-earth impurities were analyzed emission spectrographically for No.904 GdB_6. It was found that both the sintered rod and the crystal contained Tb of 100 ppm, Sm of 50 ppm and Lu of 10 ppm. Rare-earth hexaborides are soluble in one another and have nearly the same melting points of about 2500°C. The distribution coefficient of any rare-earth impurities in some hexaboride matrix must be almost unity. Zone refining is ineffective in reducing rare-earth impurities. On the other hand, Eu impurity of about 300 ppm in the sintered rod was removed markedly to about 10 ppm in the crystal because

of its high volatility. Rare-earth impurities in EuB_6 crystal were analyzed by fluorescent X-ray analysis which showed traces(less than 0.01 wt%) of Er, Dy and Sm.

The RRR could not be determined for CeB_6, EuB_6 and GdB_6. Since the magnetic transition of CeB_6 lies at 2.4 K, even the resistance at 1.6 K does not approximate the residual resistance. Both EuB_6 and GdB_6 showed complicated temperature dependence of the electrical resistivity below the magnetic transition temperature. It seems that the magnetic part of the electrical resistivity contributes substantially even below the transition temperature. Therefore, the value of RRR is meaningless. On the other hand, SmB_6 behaves like a semiconductor resistively so that the RRR cannot be defined. However, the resistivity saturates at sufficiently low temperature. The saturated resistivity seems to be dependent on the crystal purity, e.g. single zone-passed crystal, 3-fold zone-passed crystal and 4-fold zone-passed crystal had the saturated resistivities of 0.08 Ωm, 0.3 Ωm and 0.7 Ωm, respectively. The electrical resistivities of these hexaborides will be discussed in sec.3-2-7.

2-6. Transition metal diborides

Single crystals of TiB_2, ZrB_2 and CrB_2 whose melting points are 3225°C, 3245°C and 2200°C[28], have been prepared by floating zone method. There was violent volatilization from the molten zone of TiB_2 and ZrB_2. Raw powder of TiB_2 whose nominal purity is 99.5 % up, was purchased from Herman C. Starck Inc. Raw

powders of ZrB_2 and CrB_2 whose nominal purities are 99.9 %,
were purchased from Research Inorganic Chem. Corp. In the case
of ZrB_2, hafnium free powder was used.

2-6-1. Preparation of the polycrystalline rod

　　The method of preparing the sintered rod was essentially
the same as the case of LaB_6. The compact rods of raw powder
were produced by a hydrostatic press at 9.5×10^7 Pa following
a die press at 3×10^7 Pa under the friction free condition.
The crucibles used for sintering were graphite susceptor as
shown in Fig.2-7 for the case of ZrB_2 and CrB_2. However, in the
case of TiB_2, direct use of the graphite susceptor as the sintering
crucible caused a severe carbon contamination of the sintered rod.
This is due to both evaporation of carbon and TiB_2 provoked by
a reaction between them at both the surface of the TiB_2 rod and
the graphite crucible wall. Such a phenomenon was not observed
for ZrB_2 and CrB_2, because ZrB_2 has higher chemical inertness and
lower vapor pressure than TiB_2. The sintering temperature of
CrB_2 was relatively low, corresponding to its lower melting point
so that the vaporization of CrB_2 stayed at a low level during
sintering. The BN crucible inserted in the graphite susceptor
was used only for the case of TiB_2. This improved not only
the purity of the sintered rod but also its toughness. The
sinterings were carried out at 2200°C to 2300°C for TiB_2 and
ZrB_2 and 1900°C for CrB_2 in Ar gas atmosphere of about 1.5×10^5
Pa for 0.5 h. In every case, the sintered rod had densities of

70~75 % of the theoretical value.

2-6-2. Floating zone

The operational procedures of floating zone passage were practically the same as those for the preparation of LaB_6 single crystals. The polycrystalline rod was heated by direct induction heating. The molten zone was shifted from the bottom to the top of the rod by lowering the sintered rod through the work coil. The work coil had an inner diameter of about 15 mm and consisted of 2 turn x 2 step coil for CrB_2 and 3 turn x 2 step coil for both TiB_2 and ZrB_2. In the latter cases, the concentration of much heating power on the molten zone was required so that the number of turns of the work coil was increased. When the molten zone of TiB_2 or ZrB_2 was formed at the initial stage of zone passage, a violent volatilization occured from the molten zone which rapidly shrank. In order to compensate for the evaporation loss, the feed rod was fed down into the molten zone faster than the growth rate. However, this violent volatilization subsided within several minutes, then the feed rate had fallen down to the same order of magnitude as the growth rate. Zone passages of TiB_2 and ZrB_2 were carried out only once, in order not to cause composition variation due to the volatilization.

CrB_2: A single pass of the molten zone for the CrB_2 polycrystalline rods was insufficient to grow a single crystal. Usually a double

pass sufficed to produce the single crystal, but in some experiments additional passes were undertaken in an attempt to reduce the impurity concentrations. Growth speeds were less than 7 mm/h, and usually 5 mm/h, for, if the growth speed exceeded 7 mm/h, only a polycrystalline rod consisting of large grains with several mm in average diameter, could be obtained. Both spontaneous growth by necking and seeded growth were tried and growth along any axes was achieved easily. In the case of the former process, the crystal growth speed necessary to obtain a neck diameter of about 3 mm, was initially about ten times that of the feed rod, i.e. the speeds were 16 mm/h and 1.5 mm/h, respectively. Both speeds were then gradually changed to the the final growth speed of 5 mm/h. The seeding procedure, where the cross section of the seed crystal was about 2 x 2 mm^2, was analogous to the above method. In both cases, the crystals were rotated at 8 rpm and since the necessary rf power for a stable zone pass depends upon the diameter of the molten zone, the power had to be carefully controlled when the crystal diameter was increasing after the necking and seeding. When seeded, growth axes were selected along [0001] or [11$\bar{2}$0]. The ambient gas pressure of Ar was set at 1.5 x 10^6 Pa.

ZrB_2 and TiB_2: In the case of these diborides, there is the steepest temperature gradient along growth direction. If the growth rate is set at a relatively low level, any initially nucleated crystallites can continue to grow, causing the zone

passed rod to consist of many thin long bunched crystallites. In order to obtain a large single crystal, it was necessary that the growth speed exceeds 15 mm/h. Ar gas pressure was 2×10^6 Pa.

2-6-3. Quality evaluation

The spontaneously grown crystal and the seeded crystal of CrB_2 are shown in Fig.2-20(a) and (b), respectively, where the dimensions of the crystals are about 8 mm diameter and 50 mm long. Back reflection Laue photographs showed the crystal to be single but sometimes diffraction spots split within a few tens of minutes in arc, indicating that the crystal
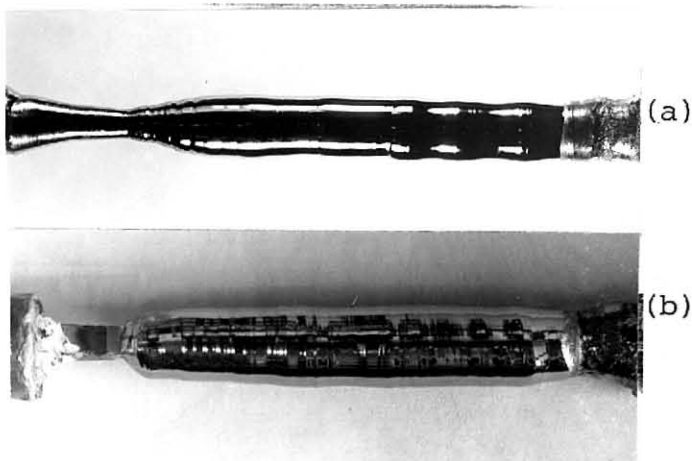

Fig.2-20. Photographs of the (a) spontaneouly grown crystal by necking and (b) seeded crystal of CrB_2.

consisted of sub-grains. The existence of sub-grains with several millimeters in average diameter was also observed from neutron diffraction experiments by Funahashi[42].

The crystal rods of ZrB_2 and TiB_2 consisted of large single crystal at the center of the rods and polycrystalline rim of about 1 mm thick at the peripheral region. The ZrB_2 crystal obtained is shown in Fig.2-21 and the cross sections are shown

-71-

in Fig.2-22(a) and (b), where (a) and (b) show the rod consisting of many bunched crystallites and that consisting of large single crystal domain and polycrystalline rim, respectively. The appearance of the polycrystalline rim may be ascribed to a steeper temperature gradient at the surface region of the crystal. In the core region of the ZrB_2 crystal, back reflection Laue photographs showed sharp spots, indicating that there is no sub-grain formation. However, the Laue spots of TiB_2 splitted into several spots within a few degrees corresponding to the sub-grain formation. The TiB_2 crystals contained many cracks after

Fig.2-21. Phtograph of the as-grown ZrB_2 crystal whose surface has golden luster due to ZrN formation.

(a)   (b)

Fig.2-22. Section photograph of ZrB_2 crystals.
(a) Formation of many crystallites is observed.
(b) Single crystal surrounded by polycrystalline rim.

the zone passage. The crystal rod often broke down to large crystallites of about 5 mm average diameter while being removed from the furnace. This phenomenon is characteristic of only TiB_2 and was not observed for any crystals of hexaboride or diboride.
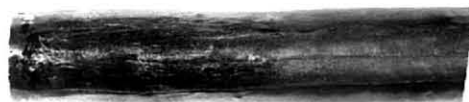
(i) Stoichiometry and impurity

According to the phase diagram[28], transition metal diborides have nonstoichiometric region. Congruently melt composition of CrB_2 is reported to be $CrB_{2.1}$. On the other hand, those of ZrB_2 and TiB_2 are $ZrB_{1.9}$ and $TiB_{1.9}$. The phase diagram must be checked by the floating zone method like the case of LaB_6 and GdB_6. This was done for CrB_2. The sintered rod of CrB_2 was passed through by the molten zone. Chemcial analysis showed the chemical composition of the 2-fold zone-passed crystal to be $CrB_{1.96}$ and that of the 6-fold zone-passed crystal to be $CrB_{1.89}$. Thus congruently melt composition is probably located at about $CrB_{1.9}$. In order to obtain a stoichiometric crystal, the zone composition should be set at some composition of $B/Cr > 2$. For simplicity, a suitable amount of elemental boron was added to the raw powder, adjusting the composition of the sintered rod to $CrB_{2.1}$. The RRR value of the 2-fold zone-passed crystal was improved from 10 (non-addition case) to 25. This indicates that the latter crystal approximated more to the stoichiometric composition.

The composition control method of ZrB_2 and TiB_2 followed that of CrB_2. The compositions of the sintered rods were controlled to be $B/Zr=2.15$ and $B/Ti=2.13$, respectively. These mixing ratios were detemined by characterizing the crystals so as to have larger RRR value. The RRR value of ZrB_2 was improved from 12 (non-addition case) to 25. That of TiB_2 was improved from 7 to 12. The composition ratio of the added

crystal of TiB_2 was found to be B/Ti=1.97 by wet chemical
analysis.

Impurities in CrB_2 and TiB_2 were analyzed by emission
spectrographic analysis. The impurities in the raw powder and
in the 2-fold zone-passed crystal of CrB_2 are given in Table 2-7.
It seems that the effect of zone refining is not so high as LaB_6.
Distribution coefficient of transition elements may not be so
small. Moreover, the melting point of CrB_2 is relatively low
so that the purification effect by volatilization of impurity
is not expected. The latter effect may be prevalent for ZrB_2
and TiB_2, because their melting points are very high. Only a
trace of Mn impurity was detected in TiB_2 crystal. For ZrB_2
crystal, ion beam microanalysis could not detect any impurities.

Table 2-7

Impurity concentrations of CrB_2 analyzed by emission spectro-
graphic analysis.

	Impurities								
	Si	Fe	Mn	Mg	Al	Cu	Ca	Mo	V
Raw material	w	w	w	vw	w	t	w	vw	vw
2-fold passed crystal	vw	w	vw	t	vw	–	–	–	–

2-7. Concluding remarks

The methods used for preparing single crystals of LaB_6,
other hexaborides and diborides are summarized in Table 2-8,
together with their melting behaviors. Those methods were
necessary to control the stoichiometry of the crystals and

-74-

simultaneously to reduce the impurity concentrations. In
this study Spear's phase diagrams were refered for all hexa-
borides prepared. The experimental results are consistent with
the expectations from the phase diagrams.

For the diborides, it is necessary to determine the liquidus
and solidus curves under the floating zone condition to control
more precisely the composition of the crystals. By that method,
the zone leveling condition can be correctly achieved as
mentioned in sec.2-2.

Table 2-8(1) Melting behaviors and some properties of hexaborides and diborides and the composition control method used.

Material	Melting behavior	Melting point	Volatility	Raw powder	Flaoting zone
LaB_6	congruent, line composition	2715°C	high	purchased	difficult
CeB_6	d°	2550	low	synthesized	easy
SmB_6	d°	2580	low	d°	easy
EuB_6	d°	2580	violent	d°	difficult
GdB_6	incongruent, line composition	2510 (decompose)	low	d°	difficult
CrB_2	nonstoichiometric region, (congruent comp. differs from stoi. composition)	2200	low	purchased	easy
ZrB_2	d°	3245	considerable	d°	difficult
TiB_2	d°	3225	violent	d°	difficult

Table 2-8 (2)

Composition control		Growth direction control	Max. number of zone pass	feed/growth speed (mm/h)	Gas pressure (kg/cm^2)
LaB$_6$	—	spontaneous nucleation	3	10/12	15
CeB$_6$	—	d°	3	10/10	15
SmB$_6$	—	d°	4	10/10	15
EuB$_6$	—	d°	2	20/15	20
GdB$_6$	zone leveling method (zone comp. was controlled)	d°	3	3.5/3.5	15
CrB$_2$	boron addition to raw powder	seeding,[0001] and [11$\bar{2}$0]. Spontaneous nucleation by necking process.	6	7/7	15
ZrB$_2$	d°	spontaneous nucleation	1	20/15	20
TiB$_2$	d°	d°	1	20/15	20

Chapter 3. Electronic properties of MB_6 and MB_2

3-1. Experimental

3-1-1. The de Haas-van Alphen effect

(i) dHvA oscillation detection

The dHvA effect[15] is an oscillatory phenomenon of the diamagnetic susceptibility of metals, semimetals and degenerate semiconductors. The dHvA effect arises from the quantization of the conduction electrons in the magnetic field. Strong magnetic field and low temperature are essential to observe the dHvA effect; the quantization of the electron orbits should not be blurred by collisions and the population oscillations should not be averaged out by thermal population of adjacent orbits. Ratio B/T must be large, where B is the magnetic field used and T the temperature of the measurement. In this experiment, B/T can have the maximum value of 4 T/K, where the maximum intensity of the magnetic field used was 6 T and the measurement temperature was usually about 1.5 K.

There are three methods to observe the dHvA effect; field modulation method, torque method and pulse magnetic field method. In this experiment, the field modulation method was used, that is, the sweeping dc magnetic field is modulated by sinusoidal ac field. Block diagram of the apparatus is shown in Fig.3-1.

The apparatus consists of a cryostat containing a super-conducting magnet and a measurement system. The superconducting magnet used has the inner bore diameter of 40 mm. Uniformity

of the magnetic field should be better than 0.1 % in a sphere

of radius 1 cm for the dHvA measurement.   The uniformity of
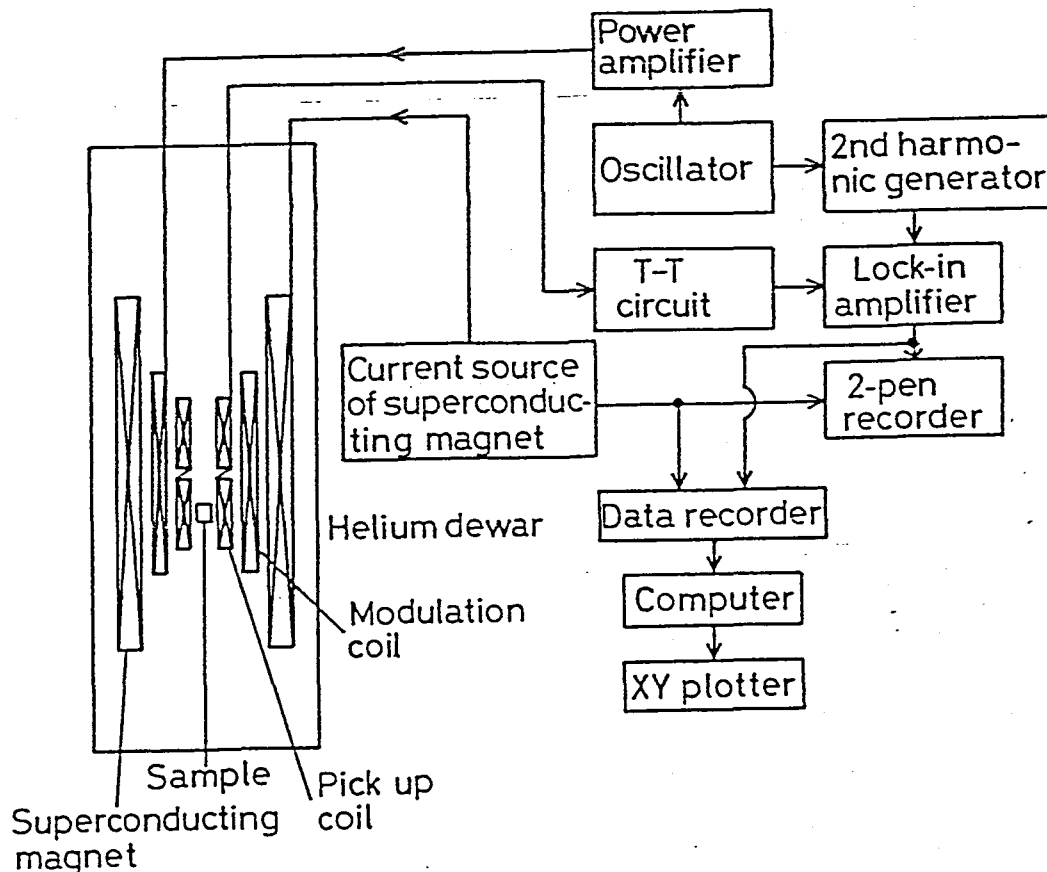

Fig.3-1. Block diagram of the dHvA measurement apparatus.

the present magnet is 0.01 % in a sphere of radius 1 cm.

Sweep velocity can be selected from 5 x 10^{-5} T/sec

to 1 x 10^{-2} T/sec.   Linearity of the field sweep is better than

0.005 %.

The measurement system consists of a pick-up coil, a

compensation coil, a modulation coil and accompanied electronic

circuit equipments.   The system is shown in Fig.3-2 except

the electronic circuit

equipment. The whole

system was fixed by a

wedge in the inner bore

of the superconducting

magnet. This prevents the

system from vibrating under

the strong magnetic field.

The modulation coil which

was wound 3023 turns with

0.1 mm diameter polyester-

coated copper wire on 25 mm

diameter acril resin bobbin,

is mounted at the extreme

outer side of the system.

At every step of winding,

the copper wire was fixed

by   varnish(GE 7031).

Modulation coil was driven

by the power amplifier with

frequency ω which is

generated by a RC frequency

Fig.3-2. Configuration of the
measurement system. The compensa-
tion coil which is located above the
pick-up coil, is not shown.
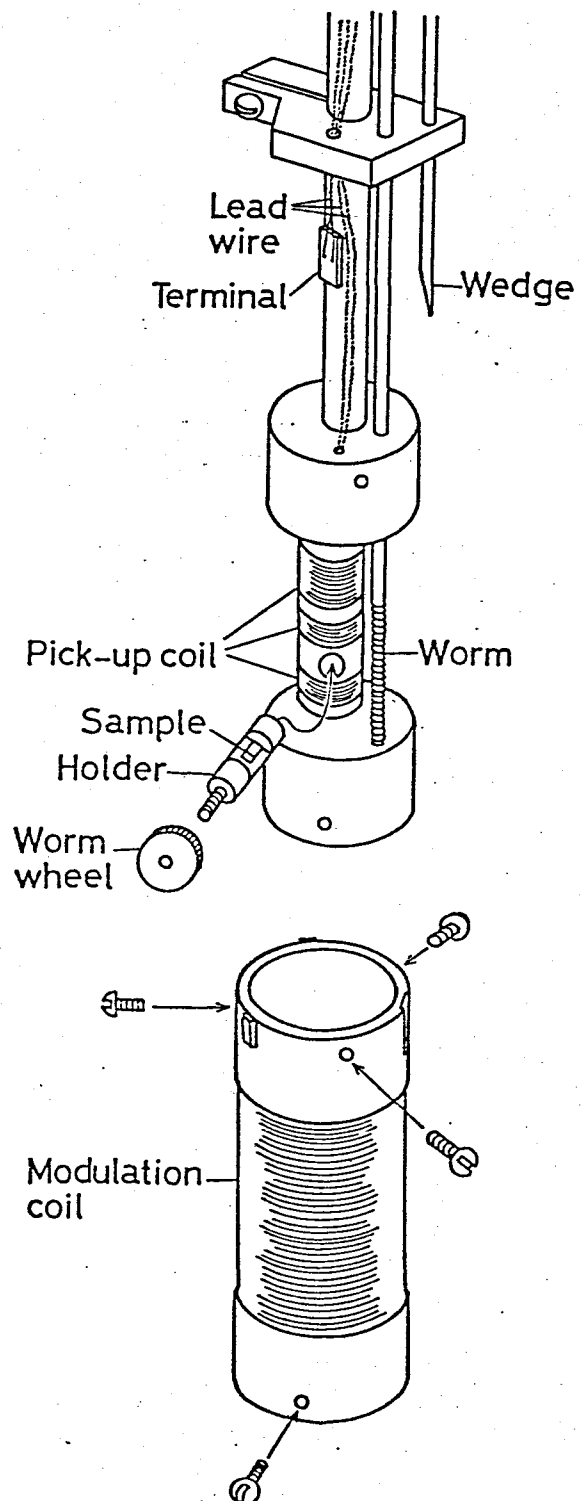
generator. The modulation frequency ω was set at 400 Hz in this experiment.

The specimen can be rotated about a horizontal axis by a worm gear system whose worm shaft is brought out from the cryostat. One turn of the worm shaft tilts the specimen by 6.54°.

The pick-up coil consists of pair of coils. They are separated one surrounding and one above the specimen. Further, the former coil is separated as shown in Fig.3-2; each coil was wound 3300 turns with 0.05 mm diameter polyester-coated copper wire on 8 mm acril resin bobbin. The latter coil was counter-wound 6600 turns. They were connected in series so as to balance out most of the ω signal. The wire fixing method was the same as in the case of the modulation coil.

The role of the compensation coil is to achieve better cancelation in the pick-up coil. The number of turns of the compensation coil was only 300. For the present measurement, the cancelation in the pick-up coil was enough to detect the signal so that the compensation coil was not used.

The signal voltage from the pick-up coil is amplified by a lock-in amplifier(PAR model HR-8) with tuned frequency of 2nd harmonics 2ω. Before the amplification, the remainder fundamental frequency component is rejected by twin-T filter circuit for the improvement in signal/noise ratio. The obtained voltage v which is the 2ω component of the signal, is proportional to d^2M/dB^2 where M is the magnetization. The voltage v is recorded on both pen recorder and paper tape after

rejecting the drift-
ing component using
a high pass filter
whose cut-off freq-
uency was set at 0.03
Hz. An example of
the measured dHvA
signal is shown in
Fig.3-3. The magnet
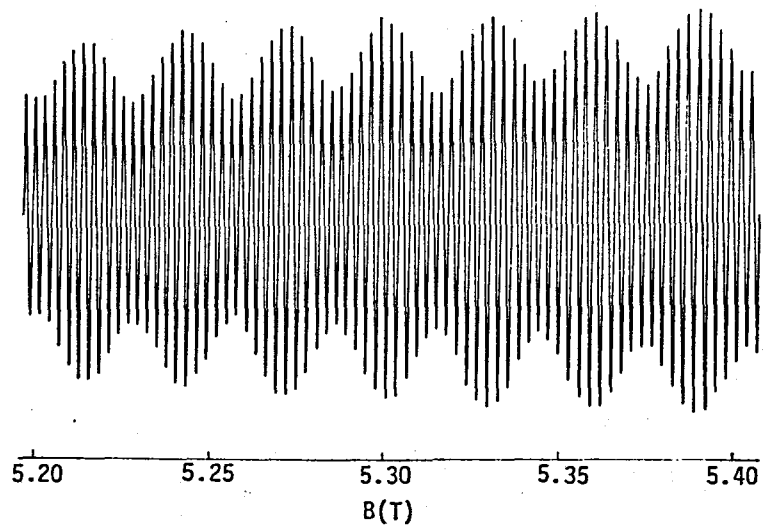current is also
recorded on the

5.20   5.25   5.30   5.35   5.40
                            B(T)

Fig.3-3. An example of the measured dHvA
signal. LaB_6, $\vec{B}$// [110].

paper tape. The voltage v and the magnet current I are
recorded alternatively at time intervals of 0.5 sec.

(ii) Measurement of the dHvA frequency

The dHvA oscillation has the form of $M=M_0(B)sin(2\pi F/B+\beta)$,
where $M_0(B)$ is the oscillation amplitude having a slow dependence
on the field strength, F is the oscillation frequency and β is
the phase. The observed voltage v usually consists of several
fundamental dHvA oscillations, their higher harmonics and their
sum or difference frequency oscillations;

$$v \propto \Sigma_i M'_{0_i} sin(2\pi F_i/B+\beta_i).$$

The frequency F_i of each component can be obtained by Fourier
analysis of the voltage v which was carried out by an electronic
computer in the following way. The flow chart of the computer

-82-

is shown in Fig.3-4.

At first, the
data set (v_s, I_t)
$s,t=1{\sim}n$ is converted
to the data set
$(v_s, B_s)_{s=6{\sim}n-5}$.

n was about 1500.
The values of I_{t-1}
and I_t are the magnet
current at 0.5 sec
before and after the
time when v_s is record-
ed. The magnetic field
B_s at the time when v_s
is recorded, may be
calculated by averag-
ing I_{t-1} and I_t,
however, the sweep
velocity of B is so
slow that increment
$\Delta I = I_t - I_{t-1}$ is only
several times the noise level, where $\Delta I/I$ is of order of 10^{-4}.
The average $(I_t + I_{t-1})/2$ cannot give an accurate value of B_s.
The B_s is then calculated with averaging 10 values of I_t,

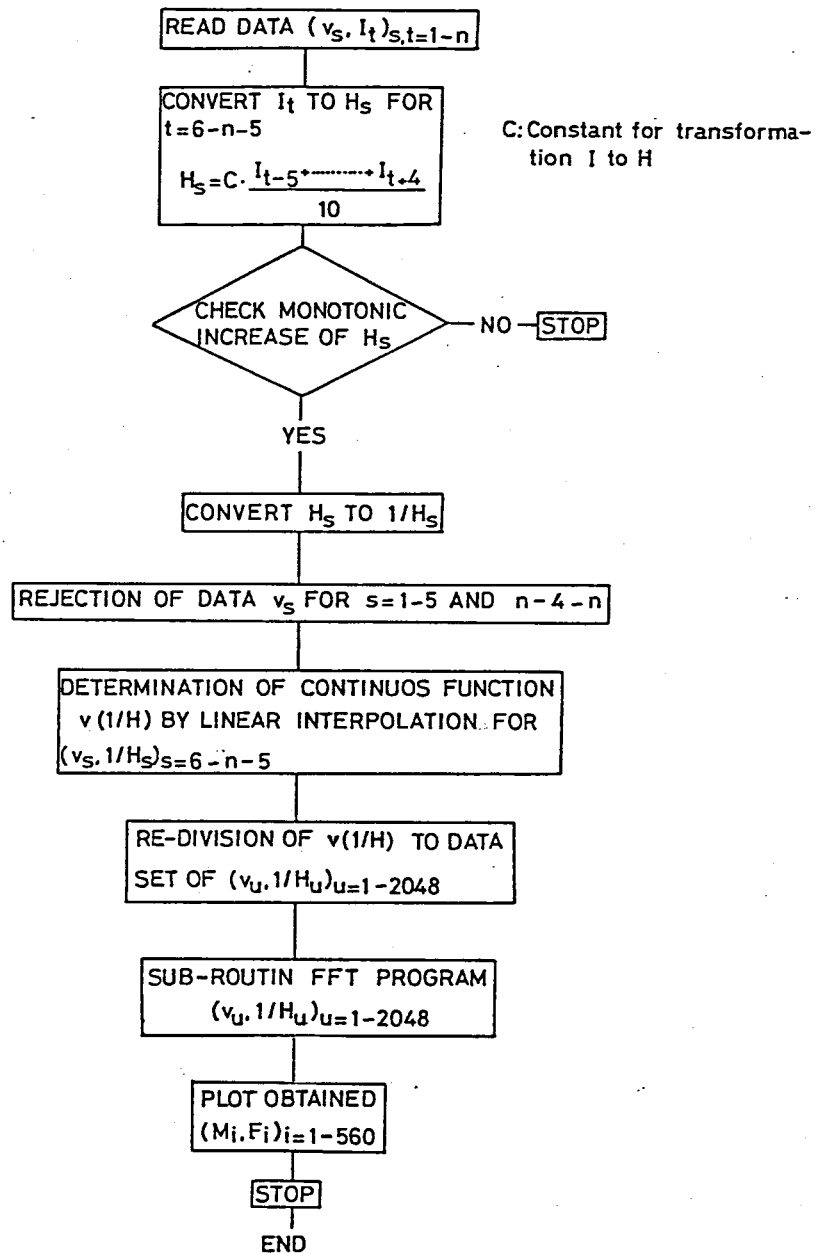$$B_s = C \frac{(I_{t-5} + \cdots + I_{t-1} + I_t + \cdots + I_{t+4})}{10}$$

READ DATA $(v_s, I_t)_{s,t=1-n}$

CONVERT I_t TO H_s FOR
$t=6-n-5$

$$H_s = C \cdot \frac{I_{t-5} \cdot \cdots \cdot I_{t+4}}{10}$$

C: Constant for transforma-
tion I to H

CHECK MONOTONIC
INCREASE OF H_s — NO — STOP

YES

CONVERT H_s TO $1/H_s$

REJECTION OF DATA v_s FOR $s=1-5$ AND $n-4-n$

DETERMINATION OF CONTINUOS FUNCTION
$v(1/H)$ BY LINEAR INTERPOLATION FOR
$(v_s, 1/H_s)_{s=6-n-5}$

RE-DIVISION OF $v(1/H)$ TO DATA
SET OF $(v_u, 1/H_u)_{u=1-2048}$

SUB-ROUTIN FFT PROGRAM
$(v_u, 1/H_u)_{u=1-2048}$

PLOT OBTAINED
$(M_i, F_i)_{i=1-560}$

STOP

END

Fig.3-4. Flow chart of the Fourier analysis.

-83-

where c is the constant for transformation of the magnet current I to the magnetic field B. The data pairs (v_s, B_s) $s=1 \sim 5$ and $n-4 \sim n$ were rejected because B_s cannot be calculated by the above averaging method.

For fast Fourier transformation (FFT) analysis, the number of data pairs must be 2^P, where P is an integer. Usually the pair number n obtained experimentally does not coincide with 2^P. Since the voltage v is sinusoidal with respect to $1/B$, the data set $(v_u, 1/B_u)u=1 \sim 2^P$ is necessary. Therefore the continuous function $v(1/B)$ was defined by the $(n-10)$ data points of $(v_s, 1/B_s)_{s=6 \sim n-5}$ and the linear interpolation between the data points. The function $v(1/B)$ is divided with equal interval to give the data set $(v_u, 1/B_u)_{u=1 \sim 2048}$. The data set is Fourier-analyzed using the sub-routin FFT program. The relation thus obtained between M_i and F_i is plotted by X-Y plotter. One example is shown in Fig.3-5. Each peak in the figure corresponds to some dHvA frequency.

A proportionality relation between the dHvA frequency F_i and the extremum cross section S_i of the Fermi surface perpendicular to the magnetic field direction is expressed as,

$$F_i = (\hbar/2\pi e)S_i(\theta). \qquad \text{Onsager's relation[43]}$$

Therefore, the shape and the dimension of the Fermi surface can be determined from the angular dependence of the dHvA frequency.
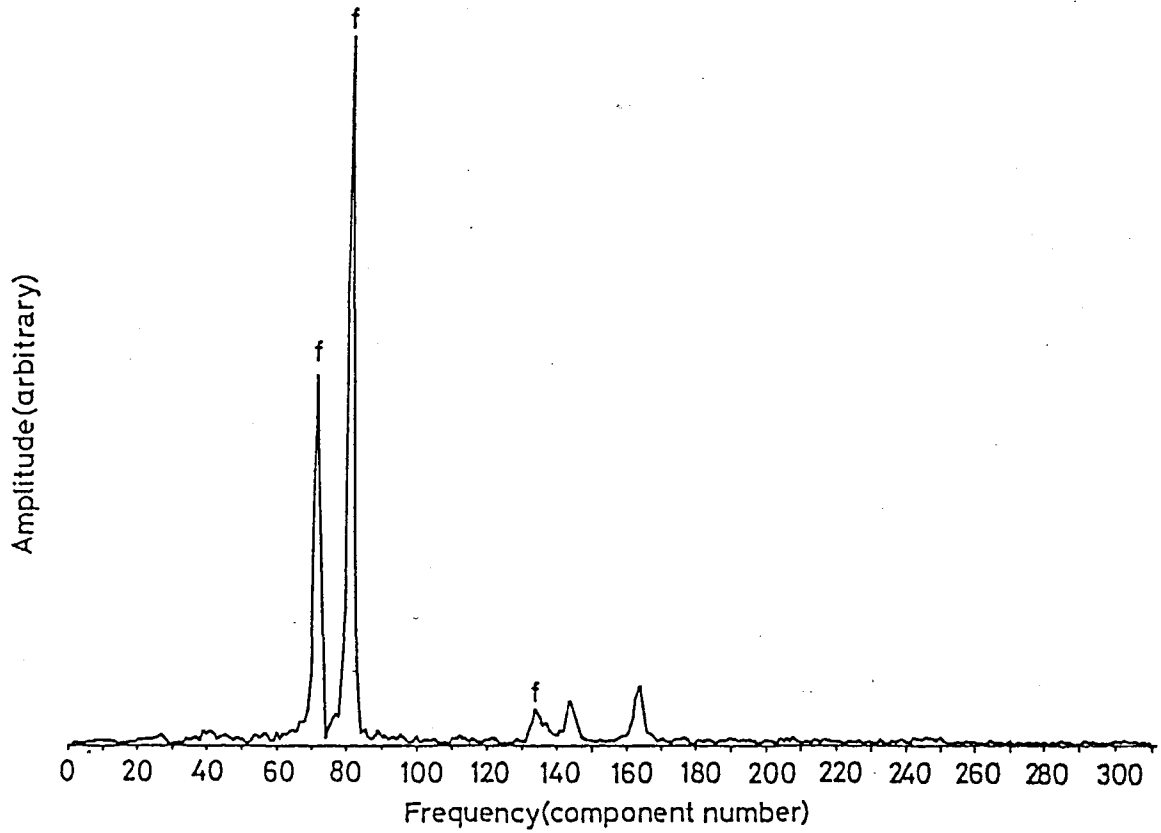
Fig.3-5. An example of the Fourier analysis of the dHvA oscillations of TiB_2. B tilts away about $20°$ from the $[10\bar{1}0]$ in the $(11\bar{2}0)$ plane.

(iii) Measurement of cyclotron mass

Temperature dependence of the dHvA oscillation amplitude a is expressed as,

$$log_e \frac{a}{T}[1-exp(-\frac{4\pi^2 k_B T}{\beta B})]=const.-\frac{2\pi^2 k_B T}{\beta B},$$

where $\beta=\frac{e\hbar}{m^*}$. The measurement of the temperature dependence of the a can give the value of cyclotron mass m^*. The observed a and T are plotted with $log_e \frac{a}{T}$ vs. T. β_1 is calculated from

the tangent of this plot. β_2 is obtained by the tangent of

$log_e \frac{a}{T}[1-exp(-4\pi^2 k_B T/\beta_1 B)]$ vs. T plot. By iteration, $\beta=\beta_n=\beta_{n+1}$

is obtained.

(iv) Measurement of magnetic field strength and temperature

The magnetic field was calibrated with the dHvA oscillation

frequency of the [100] "belly" of copper whose value is

5.98905×10^4 T at 4.5° from the [100] axis in the (010) plane[44].

The specimen temperature was measured by Ge resistance

thermometer which was calibrated with the vapor pressure of He

using temperature scale of He^4 since the specimen is in equi-

librium with surrounding liquid He.

(v) Specimen

Specimens for the measurement had the RRR value of 720

for LaB_6, 25 for ZrB_2 and 12 for TiB_2. Chemical composition

of LaB_6 must be stoichiometric as mentioned in chap.2. The

boron-added crystals of both ZrB_2 and TiB_2 which approximated

more to the stoichiometric composition, were used for the

measurement. These specimens were cut by spark errosion so

as to have dimensions of 1.5 mm^2 x 3.5 mm for LaB_6 and cube

of 8 mm^3 for ZrB_2 and TiB_2. For the case of diborides, each

cube face was parallel to the $(10\bar{1}0)$, $(11\bar{2}0)$ and (0001)

plane, respectively. After the spark errosion the specimen

was etched to remove the surface damage.

The specimen was mounted on top of a thin glass rod, and

the orientation of the specimen was determined by back reflection

Laue method. After the crystal axis for the measurement was

oriented so as to coincide with X-ray beam direction, the specimen

was transfered to the sample holder whose rotation axis was also

aligned to the X-ray beam direction. The error in orientation

between the crystal axis and the rotation axis was checked after

the specimen was fixed on the sample holder by varnish(GE 7031).

The dHvA measurement was done only if the error in orientation

was less than $\pm 0.5°$.

3-1-2. The elastic constant

A pulse overlapping method[45] was used to measure the

transit time of an acoustic wave in the sample. The block

diagram of the measurement system is shown in Fig.3-6[46].

A sinusoidal signal produced by the c.w. signal generator is

transformed to a master synchronous signal of rectangular wave

whose frequency coincides with the sinusoidal signal and to

a divided synchronous signal whose frequency is one tenth or one hundredth of the sinusoidal signal. The master signal produces the sweep for the oscilloscope on X-Y
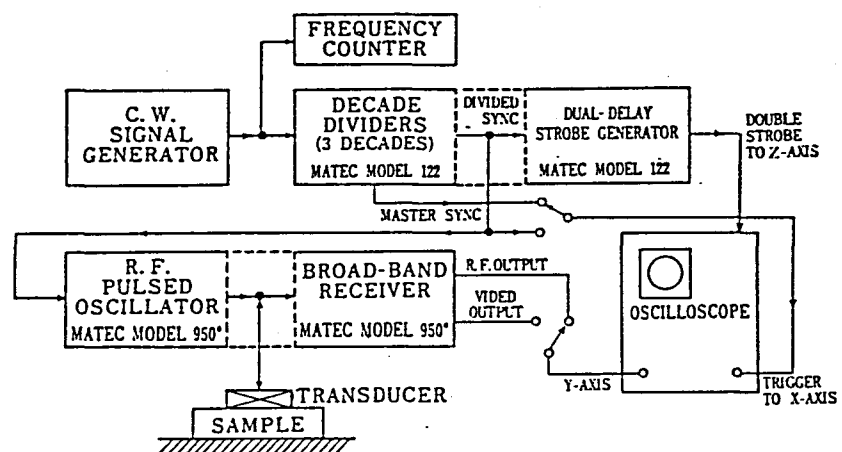

Fig.3-6. Block diagram of the sound velocity measurement[46].

operation, while the divided signal produces the trigger for the rf pulsed generator and the dual delay strobe generator. The output of the pulsed generator drives the transducer which excites the sound waves in the crystal. The returning echoes go to the Y-axis of the oscilloscope after amplification by the broad band receiver. The dual delay strobe generator actuates an intensity gate which is attached to the Z-axis of the oscillo-scope. The delays were set so that a selected pair of echoes are intensified. For the X-Y operation, the two echoes of interest are the only ones visible and are matched up cycle for cycle by making the period of the master signal to the time delay between the echoes. When the period τ of the master signal equals the delay between neighboring echoes, the sound velocity c is

$$c = \frac{2L}{\tau}$$

where L is the specimen length.

To generate the acoustic wave in the specimen, X- or Y-cut quartz transducers were used, whose fundamental freq-uency was 20 MHz for both longitudianl and transverse modes. Nonaq stopcock grease was used as the bonding material.

The crystals used were 3-fold zone passed ones. The grown crystals of LaB_6 were oriented in the [001], [110] and [111] directions and cut by the diamond cutter. The dimensions of the specimens were 8 mm diameter and 5~7 mm long. The surfaces were finished with abrasive powder of No.5000.

The length of the sample was measured at several points and averaged.

Because of unknown reasons, only some particular polarizations could be excited for each propagation direction. The measured ones are longitudinal waves in the [100] and [111] directions and shear waves in the [001] directions and waves propagating in the [110] direction polarized in the [1$\bar{1}$0] and [001] directions.

All measurements were made at room temperature.

3-1-3. Heat capacity

Measurement of heat capacity was carried out using laser flash method developed by Parker et al.[47]. The advantages of this method are (1) short time required for the measurement and (2) small sample size. However, there was a disadvantage of low accuracy of the absolute value owing to the difficulties of (1) measurement of the absorbed laser pulse energy and (2) accurate measurement of the temperature raise at high temperature.

Takahashi[48] has overcome these problems and has improved the total accuracy of the measurement to ± 0.5 %. The present measurement has followed Takahashi's method.

The schematic diagram of the apparatus is shown in Fig. 3-7. The specimen kept in vacuum is irradiated by a ruby laser. A part of the laser pulse is divided by a half mirror to a photo-cell in order to measure the relative intensity
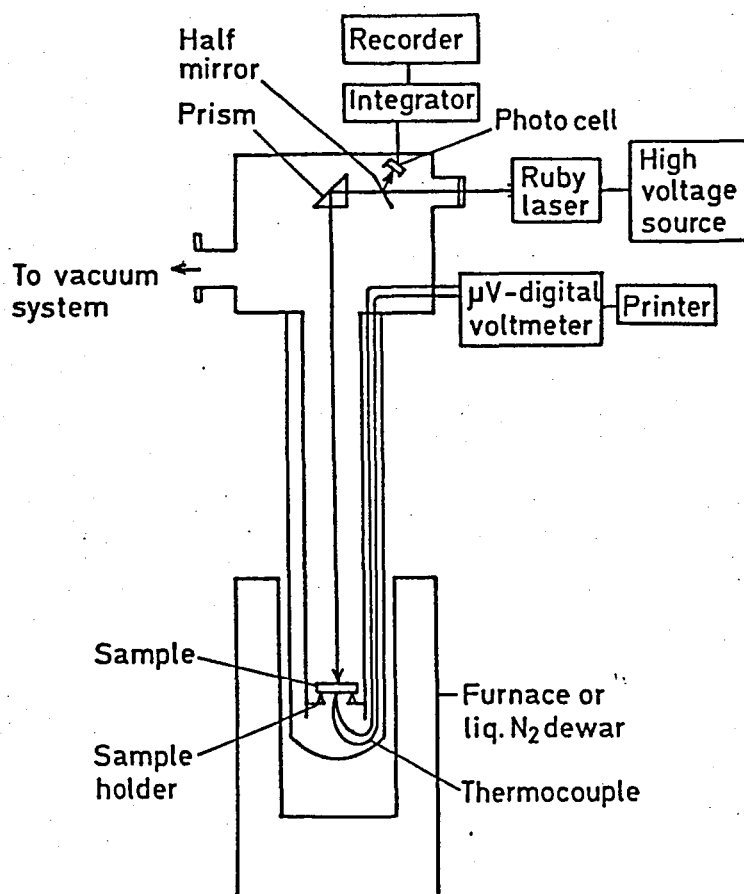
Fig.3-7. Schematic drawing of the
heat capacity measurement system.

of the laser power.
Rise in temperature
of the specimen is
measured by a thermo-
couple and a digital
μV meter.

The measurement
was divided into two
steps of (1) measure-
ment of the temperature
dependence of heat
capacity and (2) absolute
value measurement at
room temperature. At
the first measurement,
the disk specimen was
used solely. Heat

capacity c_p is obtained by the equation,

$$c_p = QM/\rho L \Delta T$$

where Q is the energy per unit surface area absorbed from the
heat pulse, ρ the sample density, M the molecular weight of the
sample and L the thickness of the sample. Absorption co-
efficient of the laser power of the specimen is assumed to be
a constant independent of the temperature. Therefore, Q is
proportional to the laser power measured by the photo-cell.

-90-

Since the accurate measurement of the absolute value of Q is difficult in this experiment, only the temperature dependence of c_p was obtained by the relation between the relative intensity of Q and ΔT.

Absolute value of c_p at room temperature was obtained using a Al_2O_3 crystal as a standard sample. In this case, a glassy carbon disk mounted on the specimen is irradiated with laser pulse. The glassy carbon disk is used as an absorption disk in order to eliminate the dependence of the absorption coefficient on the specimen materials. Heat capacity of the specimen is

$$c_p = \frac{M}{m} (\frac{E}{\Delta T} - C) ,$$

where E is the total energy of the laser power absorbed by the glassy carbon, m the quantity of the sample and C the heat capacity of the glassy carbon. Using a standard sample of Al_2O_3, the value of E was calibrated. At every measurement, the heat capacity of the glassy carbon was less than 5 % of the total heat capacity and the value was obtained from literature[48]. The glassy carbon was contacted with the specimen by silicon grease to ensure good thermal contact.

The dimension of the LaB_6 specimen was about 8 mm diameter and 2 mm thick. Thermocouple used above the room temperature was alumel-chromel wire of 0.05 mm diameter and below the room temperature was Cu-constantan of the same diameter. The thermo-emf of the thermocouple which was welded to the specimen, was

calibrated by comparing with that of another thermocouple used for the temperature measurement of the sample vessel.

Sample holder is made by Al_2O_3 ceramics. The specimen was supported by three knife edges of Al_2O_3 ceramics to lower the heat loss by conduction.

3-1-4. Electrical resistivity

Electrical resistivity was measured by standard four-point method. To ensure low-resistance contact, current contacts to the specimen were made by soldering 0.1 mm copper wire to the specimen which was electrolytically plated by copper. Furthermore the contacts was strengthened by a silver conductive paint. Potential leads of 0.1 mm copper wire were directly pasted to the specimen by the silver conductive paint. Dimension of the specimen and the interval of the potential leads were measured by the measuring microscope.

The specimen was cut by spark errosion with dimensions of about 1.5 mm^2 x 10 mm. Long axis of every specimen of hexaborides is along the [100] direction. The temperature was measured by a germanium resistance sensor below 100 K, and above 100 K a chromel-alumel thermocouple was used.

3-1-5. Thermal conductivity

(i) Thermal diffusivity

The thermal diffusivity measurements were carried out by a modulating electron beam heating method which was proposed

theoretically by Cowan[49] and followed practically by Wheeler
[50]. A thin plate specimen mounted in vacuum is heated
uniformly by bombardment of the surface with an electron beam.
If the intensity of the electron beam is sinusoidally modulated
with a frequency ν, the phase difference $\Delta\theta$ of the temperature
variation between the bombarded and the back surface is related
to the thermal diffusivity α by an equation,

$$\alpha = \frac{2.9 d^2 \nu}{\Delta\theta}$$

where d denotes the thickness of the specimen. The apparatus
shown schematically in Fig.3-8, is improved in two respects
as compared to that of Wheeler's apparatus. Wheeler controlled
the cathode temperature to modulate the intensity of electron
beam, while in this experiment the electric current in the
focussing coil was controlled by a low frequency oscillator.
The modulation circuit can be separated from the high voltage
circuit, resulting in an easy handling of the apparatus.

The phase difference measurement was improved from the
Lissajous figure method to a time interval counting method. In
the former method, a Lissajous figure was obtained by supplying
sinusoidal electric signals transformed from the top and the
bottom surfaces temperature variations by photo-cell to the
X- and Y-axis of an oscilloscope. The phase difference of
the temperature variations of both surfaces was measured by
a necessary phase shift to obtain a line Lissajous figure of
zero phase. In this method it was difficult to obtain phase

difference values of high precision.

In the improved apparatus, the sinusoidal electric signal obtained by the same method was transformed into a rectangular wave, and further it was differentiated to obtain a pulse signal. A time interval which corresponds to the

Fig.3-8. Apparatus for thermal diffusivity measurement at high temperature.

phase difference, is measured digitally by an electronic counter which is regulated so as to start counting on receiving the pulse signal from the bombarded surface and to stop on receiving the pulse signal from the other surface. Reproducibility of measurements was improved from ±10 % of the former method to less than ±4 % of the present method.

(ii) Electrical resistivity

The electrical resistivity was measured using the same apparatus as for the thermal diffusivity measurement. The specimen was heated by electron beam bombardment. This produced a dc potential drop through the specimen, thus making dc meas-
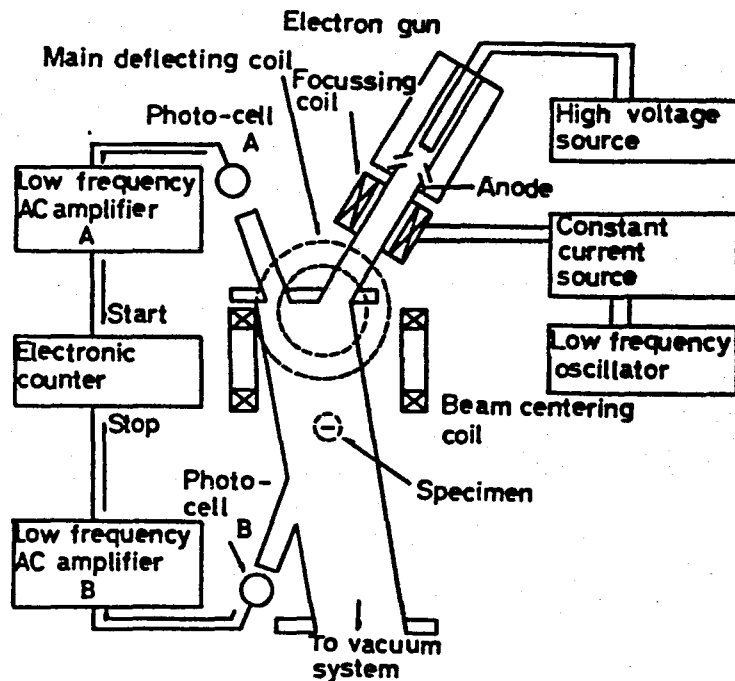
urement difficult. The resistivity measurement was made by the

ac four-point method, the current for which was supplied from a

power amplifier stimulated by an oscillator. The value of the

current was 100 mA
and the frequency
was chosen at 20 Hz,
so that an induction
emf did not occur
between the leads
of the voltage
detection system
and those of the
current supply.
The ac voltage drop
through the specimen
was detected by a
lock-in amplifier

Fig.3-9. Measurement system of high temperature
electrical resistivity.

whose output was displayed on a digital voltmeter. Good contact

between the electrodes and the specimen was achieved by using

0.3 mm diameter tungsten wire electrodes elastically attached

to the specimen. A schematic diagram of the measurement
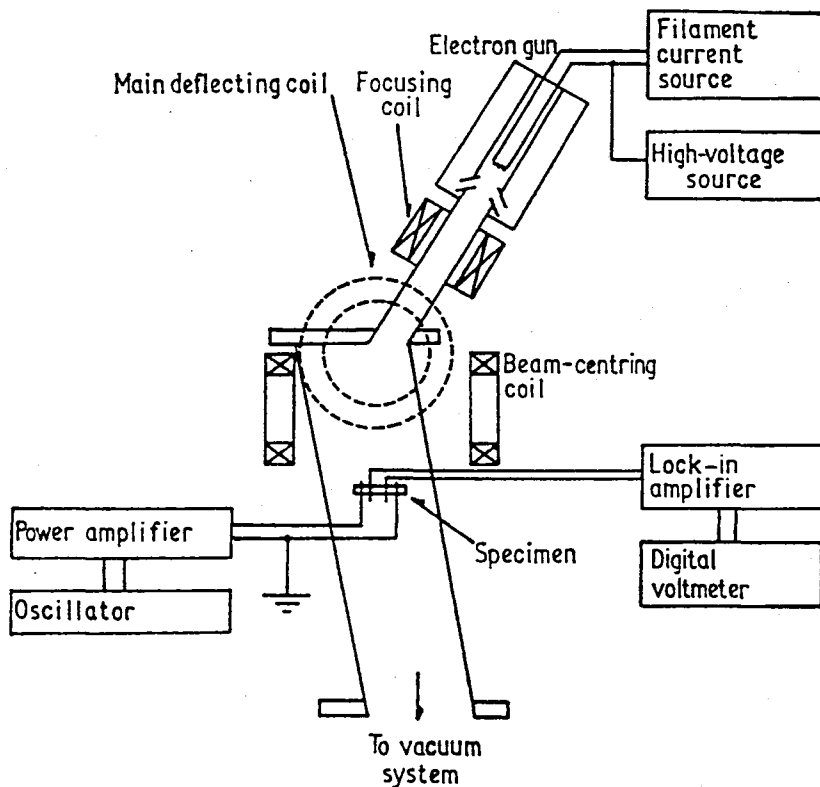
system is shown in Fig.3-9.

(iii) Thermal conductivity

    The thermal conductivity was calculated from the product

of the thermal diffusivity, the density of the specimen and

the heat capacity. Heat capacity data for LaB_6 in this temperature range of the measurement are not available. The heat capacity was calculated from the Debye function by fixing the Debye temperature of LaB_6 to be 1300 K, since the heat capacity measurement up to 1000 K(sec.3-2-4) showed that the Debye temperature of LaB_6 at high temperature is 1200∿1300 K. The electronic component of the heat capacity was calculated using a γ-value of 2.6 mJ/mole·K^2 and assuming a linear temperature dependence of the electronic heat capacity. The γ-value was obtained by the heat capacity measurement at low temperature. Total heat capacity value obtained by the summation of the lattice and electronic heat capacity is very close to the classical Dulong-Petit value of 174.6 J/mole·K and is almost independent of the Debye temperature value used.

(iv) Measurement of temperature

The temperature of the specimen was determined by the optical pyrometer with a correction of 0.8 for the emissivity [51].

(v) Specimen

In this measurement a hot-pressed LaB_6 specimen was used. Powdered LaB_6 of nominal purity 98 % up, particle size of 325 mesh, and density 4.75 x 10^3 kg/m^3, was purchased from Cerac Inc. A pellet was made from the powder by the Government Industrial Research Institute, Osaka, using the hot-press

technique(2 x 10^7 Pa, 2100°C, 0.5 h).   The apparent density of

the pellet was 92.2 %.   The hot-pressed pellet was cut down

to a disk of 8 mm diameter and 1.3 mm thick for the thermal

diffusivity measurement, and then shaped to a parallelpiped

7 x 2.5 x 1.3 mm^3 for the electrical resistivity measurement.

3-2.   Results and analysis

3-2-1. The dHvA effect on LaB_6

(i) Results

The dHvA oscillations were observed in the frequency range

of 2.13 x 10^2 T to 1.63 x 10^4 T.   The oscillations labelled α

were most easily detected because of its large amplitude.   The

oscillations having frequencies of the order of 10^3 T are

shown in Fig.3-10.   The α oscillations have three branches in

the (010) plane.   The α_1 and α_2 branches are degenerate in the

($1\bar{1}0$) plane.   The minimum frequency of the α oscillations is

7.89 x 10^3 T of the α_3 branch at the [001] direction.   The

maximum value should be observed at the [001] direction for the

α_1 and α_2 branches, however, these branches disappear in the

vicinity of the [001] direction.   Though the α oscillations

can be observed at most of the angular region and have large

amplitudes, they disappear suddenly at some angular regions

shown by the hashed(vertical) lines in Fig.3-10.   Moreover,

they could not be observed at the angular regions shown by the

dashed lines.

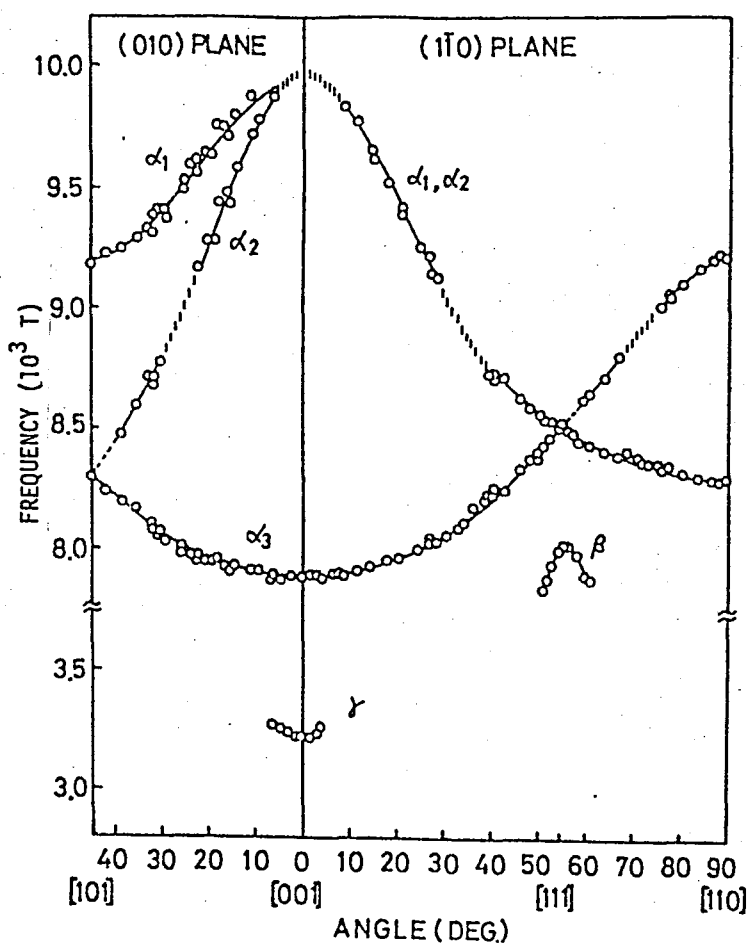The angular dependence of the oscillation amplitudes

Fig.3-10. Angular variations of the dHvA frequencies of the order of 10^3 T for field directions in the (010) and (1$\bar{1}$0) planes.

are shown in Fig.3-11 for the α_1, α_2 and α_3 branches in the (010) planes, where the amplitude which is the largest one in all of the dHvA oscillations observed, is normalized at 20. The disappearance region of the α oscillations (vertical hashed line region in Fig.3-10) are summarized in Table 3-1. As will be mentioned later, in the angular regions shown by the dashed lines in Fig.3-10, that is, for (1) the α_2 branch from 40° to 50° in the (010) plane and (2) the α_3 branch from the [111] direction to 59° in the (1$\bar{1}$0) plane, it will be explained that α oscillations do not disappear but decrease their signal intensity so much that they could not be observed.

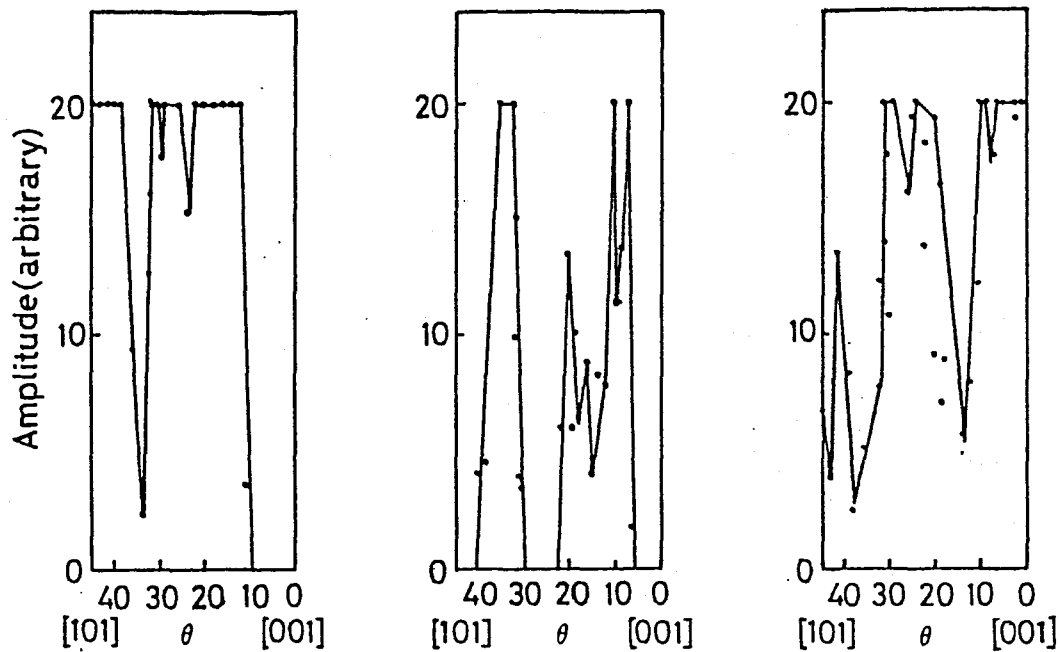In addition to the α oscillations, the β oscillations

-98-

Fig.3-11. Angular dependence of the oscillation amplitudes

for the α frequencies in the (010) plane.

Table 3-1

Angular regions where the   oscillations disappear.

Branch	(010) plane	(1$\bar{1}$0) plane
α_1	0 ∿ 6°	0 ∿ 9°, 30° ∿ 39°
α_2	0 ∿ 6°, 23° ∿ 30°	
α_3		68° ∿ 75°

were detected near the [111] direction, θ=51° ∿ 61°, in the (1$\bar{1}$0)

plane.   The β oscillations have the maximum frequency of

8.02 x 10^3 T at the [111] direction.   The γ oscillations whose

minimum value is 3.22 x 10^3 T at the [001] direction, were

observed in the vicinity of the [001] direction in both planes.

The low frequency oscillations of the order of 10^2 T

are shown in Fig.3-12.   The ε oscillations can be observed

within 6° from the [001] direction in both planes. Their minimum frequency of 8.45×10^2 T is observed at the [001] direction. The δ oscillations are observed near the [110] direction. The minimum value at the [110] direction is 5.25×10^2 T. The variation of the δ oscillations is much steeper in the $(1\bar{1}0)$ plane than in the (010) plane. The ζ oscillations were detected from $\theta = 29°$ to $65°$ in the $(1\bar{1}0)$ plane. They have a nearly constant value of 2.13×10^2 T near and beyond the [111] direction.

The μ, ν, ξ and λ oscillations have frequencies of the order of 10^4 T. Their angular dependences
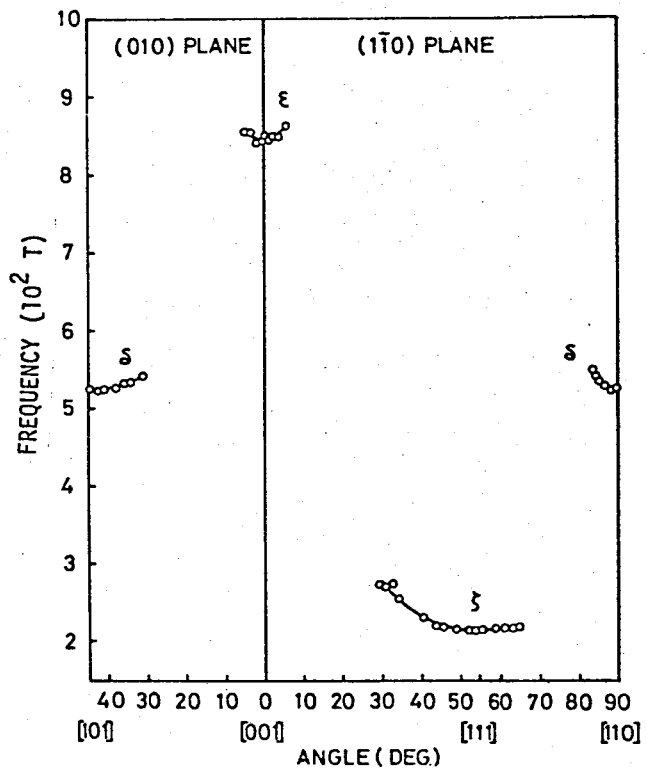
Fig.3-12. Angular variations of the dHvA frequencies of the order of 10^2 T.
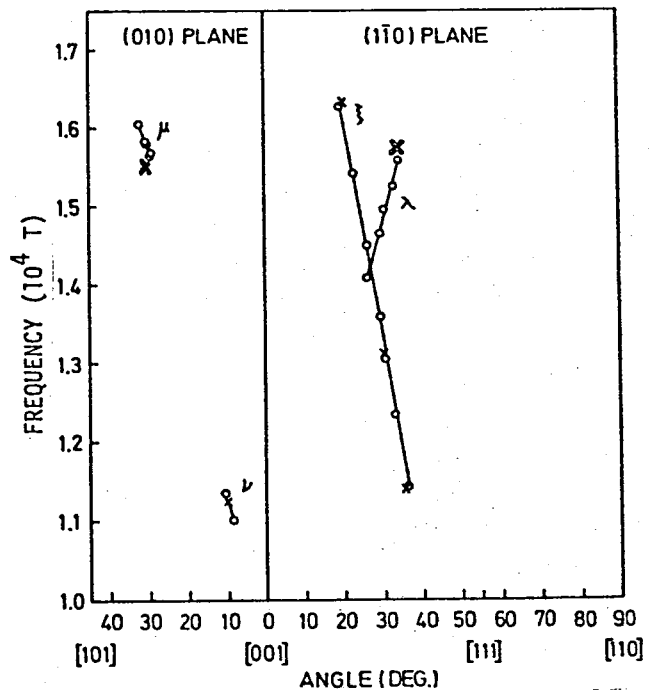
Fig.3-13. Angular variations of the dHvA frequencies of the order of 10^4 T.

are shown in Fig.3-13. Though many sum frequencies and higher

harmonics were observed in this frequency region, they are

omitted in this figure. Both the μ and ν oscillations were

observed at very narrow angular region in the (010) plane,

i.e. $\theta=29°\sim32°$ for the μ oscillations and $\theta=8°\sim11°$ for the

ν oscillations. Both oscillations increase their frequencies

when the magnetic field tilts away from the [001] direction.

In the $(1\bar{1}0)$ plane, the ξ and λ oscillations were observed.

The observed angular region of the ξ oscillations is relatively

wide and is $\theta=19°\sim36°$. The ξ oscillations decrease their

frequency when the magnetic field tilts away from the [001]

direction. On the other hand, the λ oscillations have opposite

angular dependence with the ξ oscillations. All oscillations

having the frequencies of the order of 10^4 T have very weak

signal intensities so that it is possible that they are observed

at wider angular regions under a different experimental condition.

In fact, Arko et al.[52] detected the λ, ν and ξ oscillations

at wider angular regions in magentic fields up to 7.2 T or

13.2 T and at temperatures down to 0.3 K.

The cyclotron mass of the α orbits was measured for B

along $\theta=7°$ and $52°$ in the $(1\bar{1}0)$ plane. The observed oscillation

amplitudes are tabulated in Table 3-2 and the case for $\theta=7°$

is shown in Fig.3-14 as a function of a/T vs. T. The values of

the cyclotron mass are 0.64 ± 0.02 m_0 for $\theta=7°$ and 0.67 ± 0.02 m_0

for $\theta=52°$, respectively.

Table 3-2

Temperature dependence of the dHvA oscillation amplitudes in the (1$\bar{1}$0) plane.

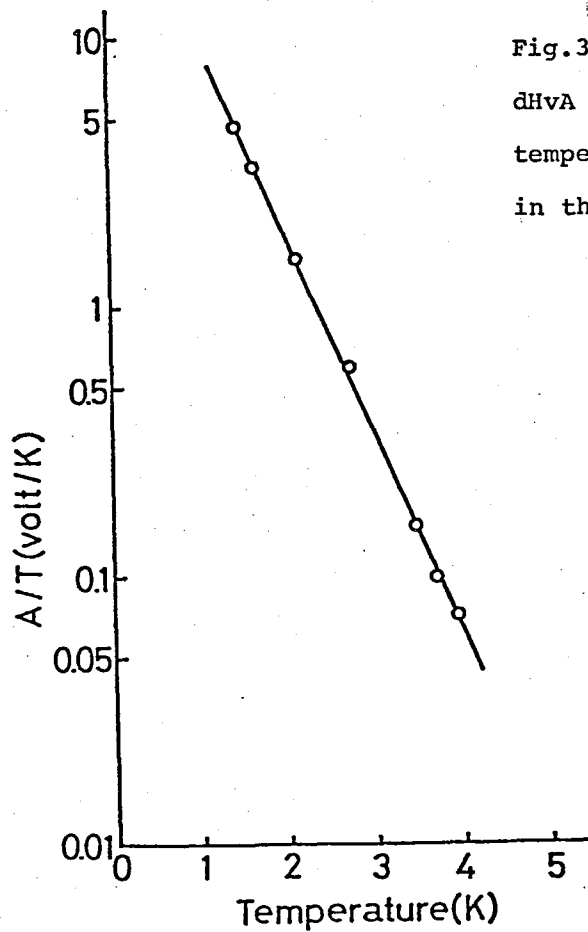| $\theta=7°$ from [001]				$\theta=52°$ from [001]		
T(K)	a(volt)	a/T		T(K)	a(volt)	a/T
1.47	6.83	4.64		1.45	2.37	1.63
1.66	5.46	3.29		2.09	1.00	0.479
2.14	3.19	1.49		2.63	0.65	0.247
2.73	1.61	0.590		∿2.75	0.37	0.135
3.47	0.522	0.150		∿3.39	0.17	0.050
3.68	0.349	0.095		∿3.88	0.08∿0.12	0.021∿0.031
3.94	0.272	0.069				

Fig.3-14. Temperature dependence of the dHvA oscillation amplitude divided by temperature. B is along $\theta=7°$ from [001] in the (1$\bar{1}$0) plane.

(ii) Fermi surface

Before constructing the Fermi surface, it is instructive to compare the observed dHvA frequencies and the cyclotron mass with that of free electron model. This is done in Table 3-3 by comparing LaB_6 with alkali metals and noble metals. LaB_6 is expected to have one conduction electron per unit cell, which will be confirmed in the later section. Alkali metals and noble metals resemble LaB_6 as regards the conduction electron concentration. It is well known that the behavior of the conduction electrons of both metal groups are quite similar to that of free electrons. In fact, the Fermi surfaces of alkali metals are almost spherical. In the cases of noble metals, their Fermi surfaces are closely spherical except that their Fermi surfaces contact with the hexagonal faces of the first Brillouin zone of the fcc lattice. Using the extended zone scheme, the Fermi surfaces in the neighboring Brillouin zones are interconnected by necks, i.e. the Fermi surface of the noble metals consists of the multiply-connected spherical Fermi surfaces. In the table, F_s is defined as the dHvA frequency which is proportional to the cross section of the Fermi sphere whose volume is just half of the 1st Brillouin zone. F_s is $(\frac{3}{2\pi})^{2/3}\frac{\pi h}{a^2 e}$ for fcc metals. The numerical factor should be changed to $(3/4)^{2/3}$ and $(3/8)^{2/3}$ for bcc metals and simple cubic LaB_6, respectively, where a is the lattice constant. For calculating F_s of LaB_6, the lattice constant near 0 K was estimated to be 0.41533 nm using the lattice

Table 3-3

Comparison of the observed dHvA frequencies and effective masses of one electron conductor with free electron values.

	$N(\sim0K)$ $(10^{28} m^{-3})$	$E_F(eV)$	$F_S(10^4 T)$	$F(10^4 T)$	F/F_S	observed mass(m_0)	thermal effective mass(m_0)*	Ref.
Na	2.65	3.23	2.80(bcc) 2.794(hcp)	2.818	1.01	1.24	1.27	[53,54]
K	1.40	2.12	1.832	1.828	1.00	1.21	1.28	[53,54]
Rb	1.15	1.85	1.603	1.592	0.99	1.28	1.36	[53,54]
Cu	8.55	7.05	6.115	5.828**	0.953	1.49***	1.38	[53,55]
Ag	5.94	5.53	4.795	4.570**	0.953	1.03***	1.00	[53,55, 56]
Au	5.95	5.54	4.804	4.501**	0.937	1.09***	1.14	[53,55]
LaB$_6$	1.40	2.12	1.83	0.9****	0.5	0.64 0.67	1.56	

*Thermal effective mass is defined by γobs./γfree electron, where γ is γ-value of electronic heat capacity.

F[111] value.   *[111] direction.   ****Average of the α frequency.

constant of 0.41568 nm at room temperature and thermal expansion coefficient data.

Both alkali metals and noble metals have their F/F_s values of nearly equal to unity. Since the neck Fermi surface exists in the Fermi surface of the noble metals, the F/F_s value is slightly smaller than unity. The observed cyclotron masses of these metals are from 20 % to 50 % larger than that of free electron, which is caused by the mass enhancement by the electron-phonon interaction. The Fermi surface of Ag is least distorted from the free electron sphere in the noble metals and one can expect the nearly free electron mass.

On comparing with these metals, the electron concentration of LaB_6 coincides with that of K. LaB_6 should have the same dHvA frequency as that of K according to the free electron model. In practice, however, the F/F_s value of LaB_6 is only about 0.5, indicating that the volume of the α-Fermi surface of LaB_6 is about one third that of the free electron Fermi sphere. In fact, the Fermi surface of LaB_6 consists of three equivalent α-Fermi surfaces per Brillouin zone as will be mentioned later. The thermal effective mass $(\gamma_{obs.}/\gamma_{free\ electron})$ has the original meaning as the effective mass only if the Fermi surface consists of one nearly spherical surface. The tabulated value of the thermal effective mass of LaB_6 reflects not only the real effective mass but also the shape of the Fermi surface so that it differs appreciably from the cyclotron mass.

Assuming the electron energy E to be a quadratic function of wavenumber k, the Fermi energy E_F is expressed as $E_F = \frac{\hbar^2}{2m^*} k_F^2$, where k_F is the magnitude of the Fermi wavevector. The k_F^2 is proportional to the dHvA frequency F through the Onsager's relation. Since both m^* and k_F^2 is about half of the free electron values, the real Fermi energy of LaB_6 should be close to the free electron Fermi energy of about 2.1 eV.

Since a detailed band structure calculation of LaB_6 whose result can be compared with the Fermi surface experiment was not available at the time when this experiment was done, an experimental Fermi surface was constructed using the present dHvA results.

At first, let us consider the simple cubic Brillouin zone shown in Fig.3-15. As can be seen from Fig.3-10, 12 and 13, the α oscillations were observed within the widest angular region. It is reasonable to expect that dominant Fermi surface of LaB_6
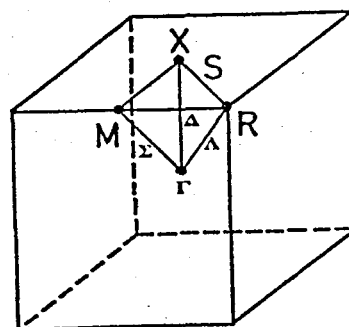

Fig.3-15. Brillouin zone of LaB_6.

should be determined by the α oscillations and all other oscillations can be assigned by the Fermi surface model constructed.

The symmetry of the α-Fermi surface can be determined from the angular dependence of the α oscillations also. This serves to estimate at which position in the Brillouin zone the center of the Fermi surface is located. As shown in Fig.3-10, the

α oscillations have three branches so that they correspond to at least three or six equivalent Fermi surfaces. The symmetry of the Fermi surface comes out from the symmetry of the α oscillations in the (010) plane assuming the inversion symmetry. The angular dependence of the α_1 branch shows that the Fermi surface has a fourfold symmetry around the symmetry axis along the [010] direction. Moreover, the angular dependence of the α_2 and α_3 branches show that there are two twofold symmetry axes perpendicular to the fourfold axis. This symmetry consideration indicates that the center of the α-Fermi surface should be located at the point X or M in the simple cubuc Brillouin zone. Thus Fermi surface of LaB_6 is found to consist of three equivalent Fermi surface pieces, being consistent with the observation of the three α branches. It is impossible to determine from the results of the dHvA experiment at which point (X or M) the α-Fermi surface should be centered. Tentatively, the α-Fermi surface is assumed to be located at the point X.

The neighboring α-Fermi surfaces appear to almost touch each other if their dimensions are calculated using the α oscillations and they are pictured. This suggests that the neighboring α-Fermi surfaces are connected by necks, forming a multiply-connected Fermi surface. The disappearance of the α oscillations at particular angular regions: (1) the α_1 and α_2 oscillations in the vicinity of the [001] direction in both the (010) and ($1\bar{1}0$) planes, (2) the α_2 oscillations around $\theta = 25°$ in the (010) plane, (3) the $\alpha_1(\alpha_2)$ oscillations

around θ=35° in the (1$\bar{1}$0) plane and (4) the α$_3$ oscillations
around θ=70° in the (1$\bar{1}$0) plane, supports the multi-connective
property of the α-Fermi surface and teaches where they are
connected. Thus, the Fermi surface of LaB$_6$ was deduced experi-
mentally to consist of a multiply-connected Fermi surface
whose anisotropy was obtained from the angular dependence of
the α oscillations. This multiply-connected Fermi surface
explains other observed γ, β, δ, ζ and ξ branches well. Fig.3-16
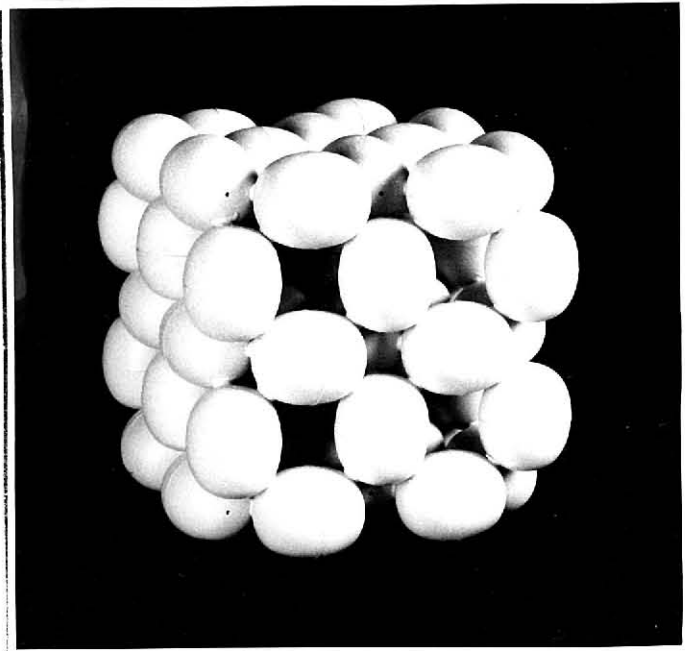shows a three dimensional Fermi surface model of LaB$_6$ (the
Fermi surface shape in the photo is a little different from the proposed one).

Recently Ishizawa et al.[57] succeeded in observing the dHvA oscillations which corresponds to the neck Fermi surface. According to their result, the neck Fermi surface has approximately a

Fig.3-16. Fermi surface model of LaB$_6$.

cylindrical shape whose axis is along the [110] direction. The
frequency corresponding to the neck Fermi surface is of
order of 5 T. They estimated the neck diameter to be 2.1×10^8
m^{-1} and the length to be 4.4×10^8 m^{-1}.

The cross section of the Fermi surface in the ΓXM and

XRM planes are illustrated in the Fig.3-17(a) and (b), where the

cross sections are close to the real shape of the Fermi surface

calculated from the angular dependence of the dHvA frequencies.

Apparently the α oscillations correspond to the electron

orbit running around the α-Fermi surface. The α oscillations

disappear when the extremal electron orbit running around the

α-Fermi surface comes across the neck Fermi surface and the

electron orbits become an open orbit. This disappearance

corresponds to the angular regions summarized in Table 3-1

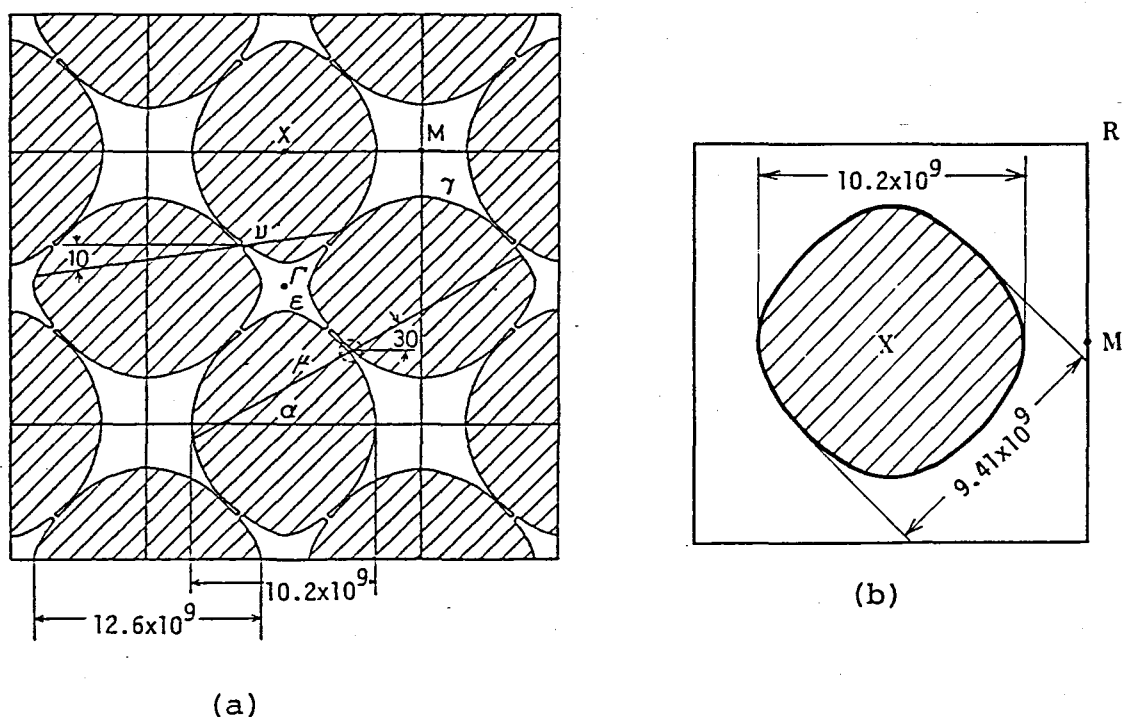(hashed vertical line regions in Fig.3-10). However, the neck

(a)

(b)

Fig.3-17. Cross sections of the Fermi surface of LaB_6 in (a)
the ΓXM plane and (b) the XRM plane. The dimension is in m^{-1}.

diameter is so thin that the α-orbits come across the neck

Fermi surface within a narrow angular region of about 2°.

Since the angular regions tabulated are much wider, the signal

intensity of the α oscillations seems to decrease rapidly as

the α-orbits come near the neck Fermi surface. In fact, Arko

et al.[52] could detect the α oscillations more closely to

the [001] direction than the present experiment by using the

stronger magnetic field of 7.2 T. This decrease of the signal

intensity is presumably caused by a magnetic breakdown effect.

As can be seen in Fig.3-17(a), the γ and ε oscillations

come out from the hole-like orbits running around the points

M and Γ, respectively. Since both the γ and ε orbits pass

through the neck, their observed angular regions are narrow.

The frequencies of the γ and ε oscillations are calculated

using the cross section shown in the figure when the magnetic

field $\vec{B}$ is along the [001] direction. The calculated values

are compared with the observed ones in Table 3-4 in which the

calculated and the observed frequencies of other oscillations

are compared also. The calculated γ and ε frequencies agree

quite well with the observed ones.

The β oscillations observed near the [111] direction in

the (1$\bar{1}$0) plane are assigned to come out from the electron orbit

which runs through six necks and six α-surfaces around the Γ

point. The estimated frequency of 5.2∿9.2 x 10^3 T at $\vec{B}$// [111]

covers the observed value of 8.02 x 10^3 T. The orbit shape is

shown in Fig.3-18(a). The ζ-orbit is assigned to the hole-like

Table 3-4

dHvA frequencies in LaB_6 for high symmetry directions.

$\vec{B}$	Orbit	observed frequency (T)	calculated frequency (T)
[001]	α	7.89×10^3	7.89×10^3
	γ	3.22×10^3	3.27×10^3
	ε	8.45×10^2	8.49×10^2
[110]	α	9.21×10^3	
	α	8.30×10^3	
	δ	5.25×10^2	5.6×10^2
[111]	α	8.51×10^3	
	β	8.02×10^3	$5.2 \sim 9.2 \times 10^3$
	ζ	2.13×10^2	2.2×10^2

orbit surrounded by three α-surfaces. The shape of the ζ-orbit is a three cornered rosette whose center lies on the ΓR line and is shown in Fig.3-18(b). The estimated frequency of 2.2×10^2 T at $\vec{B} //$ [111] is close to the observed one of 2.13×10^2 T. The δ oscillations observed near the [110] direction are considered to come out from the hole-like orbit shown in Fig.3-18(c), whose center is on the ΓM line. The estimated freqency of 5.6×10^2 T at $\vec{B} //$ [110] is close to the observed value of 5.25×10^2 T.

Since the frequencies of the λ, μ, ν and ξ oscillations exceed the maximum frequency of the α oscillations, these oscillations are assigned to come out from orbits running around at least two α-Fermi surfaces. The ξ-orbit in the $(1\bar{1}0)$ plane is a typical extremal orbit through the neck. The ξ-orbit at $\theta=30°$ is illustrated in Fig.3-19. The calculated

frequencies at three positions are shown by the sign x in Fig.3-13. Agreement between the observed and calculated frequencies is quite good. The ν oscillations in the (010) plane come out from the electron orbit running around two α-surfaces through the neck as shown in Fig.3-17(a).
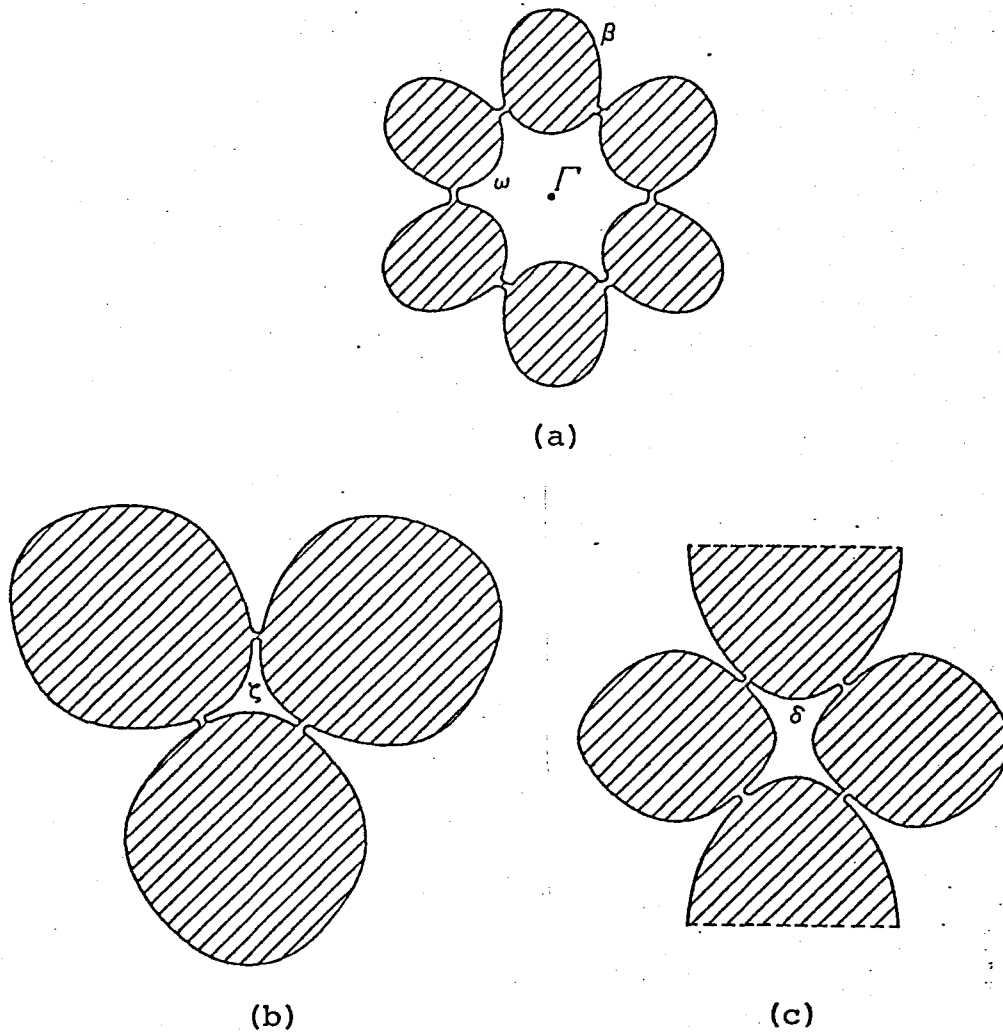
Difficulty occurs for the μ and λ orbits because there

(a)

(b)

(c)

Fig.3-18. Observed orbits on the Fermi surface of LaB$_6$. (a) β orbit, $\vec{B}$// [111], (b) ζ orbit, $\vec{B}$// [111] and (c) δ orbit, $\vec{B}$// [110].

are no extremal orbits
at such magnetic field
directions where the μ
and λ oscillations
were observed. To
overcome this
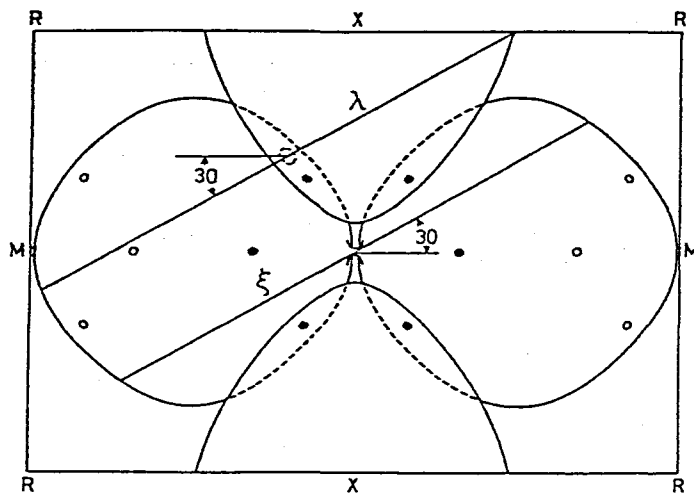difficulty, the
following experimental
facts should be con-
sidered. There are
other angular regions
where the α oscilla-

Fig.3-19. Possible orbits corresponding to
the ξ and λ oscillations. $\vec{B}$// (1$\bar{1}$0) plane.

tions could not be observed except in the angular regions where
the α-orbit becomes open by crossing the neck. The angular
regions are (1) the α_2 branch of θ=40°∿45° in the (010) plane
and (2) the α_3 branch from the [111] direction to θ=59° in the
(1$\bar{1}$0) plane. At such angular regions, the α oscillations are
considered to have so weak signal intensity that they could
not be observed. A position on the α-Fermi surface corresponding
to the above angular region, is specified approximately by the
point where the α-Fermi surface and the XX line cross each
other in the ΓXM plane. It is expected that the neighboring
α-Fermi surfaces come very close at that position and the gap
between them is so narrow that the magnetic breakdown can
happen even under the magnetic field of 6 T.

It is worthwhile to describe some aspects of the magnetic

-113-

breakdown. The magnetic breakdown is known as a transition of an electron in a magnetic filed from one classical orbit to another. The cause of this effect is the same as that of the tunnel effect: the wave nature of the electron. However, in the effect considering, the motion in a magnetic field is of special importance. In particular, the quantum nature of this motion becomes more pronounced as the intensity of the magnetic field increases. Therefore, the probability of magnetic breakdown increases with the magnetic field intensity. The onset of magnetic breakdown is another important feature of the α-Fermi surface shown in Fig.3-17(a), though it is not mentioned till now.

The above model can explain the decrease of the signal intensity of the α oscillations in the following manner. When the direction of the magnetic field is tilted and the α-orbit comes close to the position above mentioned, some conduction electrons rotating in the α-orbit break through the neighboring α-orbit by the magnetic breakdown. It decreases the number of the conduction electrons rotating in the closed α-orbit, resulting in a decrease of the signal intensity of the α oscillations.

On the other hand, the magnetic breakdown gives rise to the possibility of occurence of new extremal cross sections which extend over more than two α-Fermi surfaces. In fact, the μ- and λ-orbits can be assigned as such type of the orbits. The μ-orbit in the (010) plane is shown in Fig.3-17(a).

The magnetic breakdown occurs at the position shown by a dot circle. The frequency was calculated for the orbit shown in the figure. A sign x in Fig.3-13 indicates the calculated value which agrees well with the observed one. The λ oscillations come out from the orbit shown in Fig.3-19. A dot circle also denotes the position of the magnetic breakdown. In this case, however, the plane shown by the solid line in the figure cuts three α-Fermi surfaces; they are one vertical Fermi surface and two horizontal ones lying back and forth the vertical surface, where the last one is not shown in the figure. The observed frequency corresponds to the sum cross sections of the vertical surface and one horizontal surface. This is attributable to the fact that in the case of the intraband transition, the probability w of the breakthrough approaches only 1/2 when the magnetic field intensity increases[58]. Therefore, only a very small fraction of the conduction electrons can rotate in the orbit running around three α-surfaces. In this study, the observed frequencies are limited to only those coming from the orbits running around two α-surfaces. (Arko et al.[52] observed the orbits running around three α-surfaces using a strong magnetic field of 13.2 T.) The estimated frequency of the λ oscillations (marked by a sign x in Fig.3-13) agrees well with the observed one. The angular dependence of the λ oscillations coincides with the expected one of the above assigned orbit.

The experimental results are well explained by the

present Fermi surface model, taking into account the effect

of the magnetic breakdown. The experimental results by Arko

et al.[52] should be necessarily explained by the present

model. The dHvA oscillations observed by them are shown in

Fig.3-20, where open circles show the data obtained in the

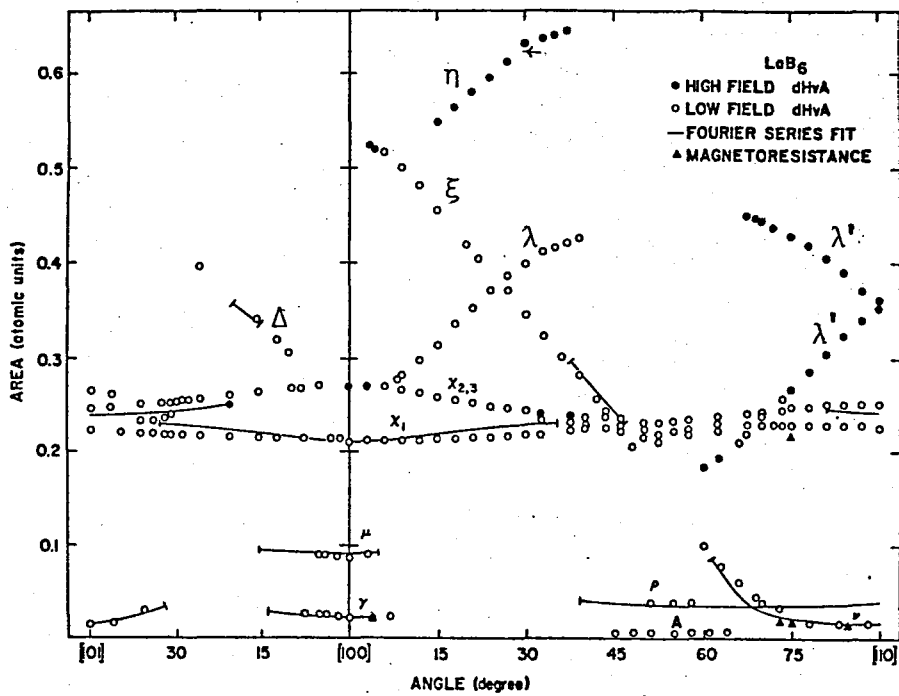magnetic field up to 7.2 T and solid circles show the data in

Fig.3-20. The observed dHvA extremal areas in atomic units of the Fermi surface of LaB_6 by Arko et al.[52].

the magnetic field up to 13.2 T. The present author labelled

those branches which were not labelled by them. Since the

magnetic field used by them is stronger than that used by the

present study, their observed angular regions of the dHvA

oscillations are wider especially at high frequency region.

*AREA(atomic units)=2.673 x 10^{-5}FREQUENCY(tesla units)

The correspondence between the labels of Arko et al. and of the present study are indicated in Table 3-5. They did not observe the β, δ and μ oscillations observed by the present study. On the other hand, the present study could not observe their ρ, ν, η and λ' oscillations. Moreover, their observed angular region of the ξ and λ oscillations are considerably wider than the present study. It is noteworthy that in their high field experiment they observed the α oscillations at the [100] direction where

Table 3-5
Labels of the dHvA oscillations.

Present study	Arko et al.[52]
α	χ
β	-
γ	μ
δ	-
ε	γ
ζ	A
-	ρ
-	ν
μ	-
ν	Δ*
ξ	ξ*
λ	λ*
-	η*
-	λ'*

*Labelled by the present author.

the α-orbit crosses the neck surface. This can be understood as the magnetic breakdown through the neck surface.

The essential feature of their Fermi surface model is the same as the present model. However, they approximated the α-Fermi surface as a "sphere" and their estimated neck Fermi surface seems too large. They did not assign orbits for all of the oscillations observed by them, especially for the oscillations of high frequency region. Their assignment for

the χ, γ and μ orbits agrees with the present author's. They

assigned the ρ oscillations near the [111] direction to corres-

pond to the three cornered rosette which corresponds to the ζ

oscillations in the present study. The frequency of the ρ

oscillations seems too high for the three cornered rosette,

which corresponds better with A oscillations. The ρ oscillations

may come out from a hole-like ω orbit shown in Fig.3-18(a).

According to their assignement for the ν oscillations, the ν

and ξ oscillations come out from the same orbit but at different

angular regions. Certainly those two branches can be extra-

polated from one another.

The λ' and η oscillations were observed only under their

high field condition. The λ' oscillations are understood as

a branch of the λ oscillations observed near the [110] direction.

The η oscillations have the highest frequency in the observed

dHvA oscillations. Since the frequency of the η oscillations

is higher than those of the ξ and λ oscillations which come

from the orbits running around two α-surfaces, the η orbit

must run around three α-surfaces. The angular dependence of

the η oscillations is similar to the λ oscillations. As

mentioned in the assignment for the λ branch, there is an orbit

running around three α-surfaces cut by a plane which is almost

the same plane containing the λ orbit. That orbit corresponds

to the η oscillations. The estimated frequency of the η oscilla-

tions at $\theta=30°$ is shown by a sign $\leftarrow$ in Fig.3-20. The value

agrees well with the observed one. Therefore, the present Fermi

surface model explains well also the experimental results by Arko et al.

The closest gap between the neighboring α-Fermi surfaces can be estimated in the following manner. According to the experiment of Arko et al., the magnetic breakdown through the neck surface was observed at the magnetic field of 13.2 T. Taking into account the neck diameter to be 2.1×10^8 m^{-1} and the magnetic field of the present study to be 6 T, the gap is about half of the neck diameter, i.e. 1×10^8 m^{-1}. A critical field B_c for the intraband magnetic breakdown is expressed as[58],

$$B_c = \Delta\varepsilon/\mu,$$

where $\Delta\varepsilon$ is the potential barrier and $\mu = e\hbar/2m^*$. Under present experimental condition, the gap Δk is estimated to be 0.95×10^8 m^{-1} assuming $\Delta\varepsilon = \hbar^2\Delta k^2/2m^*$. Both estimated values are within the same order of magnitude.

Some conclusion can be drawn for the conduction band structure of LaB$_6$ using the present multiply-connected Fermi surface model. The carrier density of the conduction band of LaB$_6$ is calculated to be 1.39×10^{28} m^{-3} which corresponds to just one conduction electron per unit cell. The value agrees well with the measured Hall coefficient of 4.5×10^{-10} m^3/coul. The band structure calculation by Longuet-Higgins and Roberts is correct as far as the carrier concentration is concerned.

Since the observed Fermi surface which is not centered at Γ but at X(or M) cannot be described by the nearly free electron

model, the conduction electrons are considered to have almost no s-character. The La-5d character should be the main in the conduction band, considering the electron configuration of La atom.

The conduction band is relatively wide as mentioned before though its character is d-like. In LaB_6 the distance between La atoms is so wide as compared to its metallic radius of 1.88 Å. It is unlikely that neighboring La-5d orbitals overlap each other. The spreading of the conduction band of LaB_6 may be due to mixing of B-2s2p orbitals into the La-5d orbitals.

(iii) Comparison of Fermi surface with theoretical calculation

The first calculation of the Fermi surface of LaB_6 was carried out by Perkins et al.[59] using a LCAO approach, however, their Fermi surface does not even agree qualitatively with the experimental Fermi surface. Such a disagreement might have occured through neglecting the excited d-state of the metal atoms from their calculation.

Recently several quantitative calculations of the band structure of LaB_6 which can be compared with the experimental Fermi surface, were carried out, being stimulated by the present experiment. The first quantitative calculation was carried out by Arko et al.[52] followed by Walch et al.[60]. The former authors constructed the Fermi surface by correcting the parameters of the band structure calculation to fit it

with the results of their own dHvA experiment. Their Fermi

surface consists of a "sphere" enclosing one third of an

electron per unit cell. The "sphere" is located at the point

X in the Brillouin zone. Each "sphere" is connected by a

thin plate-like neck surface along the [110] direction.

Their Fermi surface model agrees qualitatively with the present

model, though, their Fermi surface model is rather crude so

that the angular variation of the dHvA frequency cannot be

explained well by their model. They calculated effective mass

of the conduction electron to be 0.3 m_0. As already noticed

by them, the calculated value is too small as compared with the
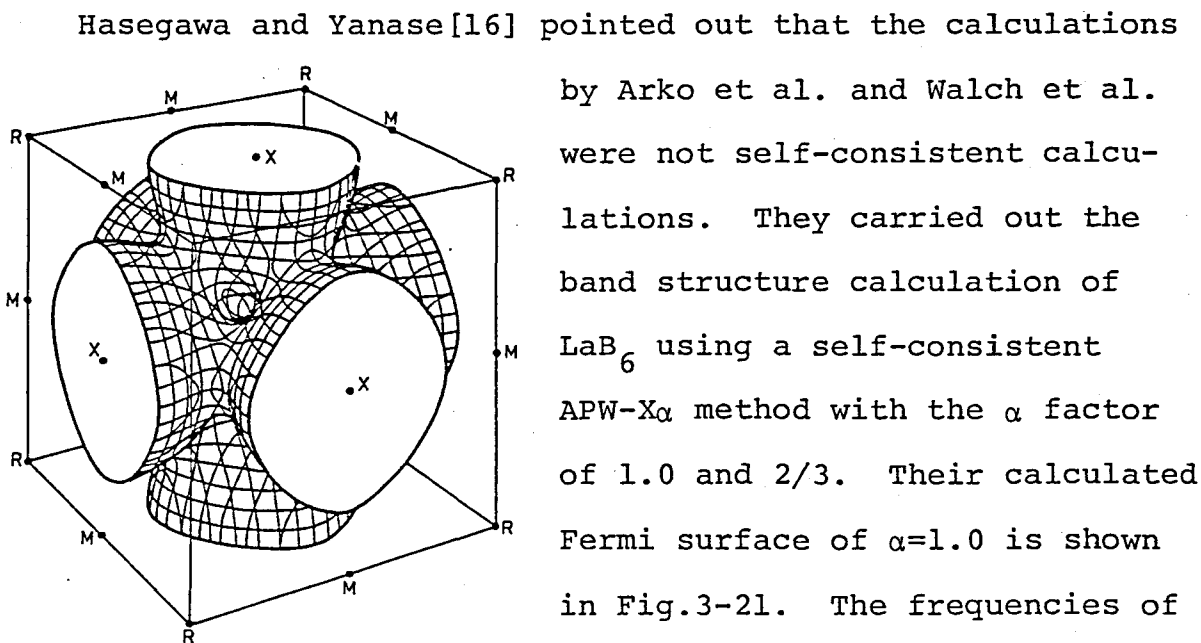
observed cyclotron mass of 0.6 m_0.

Hasegawa and Yanase[16] pointed out that the calculations
by Arko et al. and Walch et al. were not self-consistent calculations. They carried out the band structure calculation of LaB_6 using a self-consistent APW-$X\alpha$ method with the α factor of 1.0 and 2/3. Their calculated Fermi surface of $\alpha=1.0$ is shown in Fig.3-21. The frequencies of the selected extremal cross sections are compared with the experimental frequencies in Table 3-5. It is found from Fig3-21 and Table 3-5 that the shape of the α-Fermi surface agrees well

Fig.3-21. Fermi surface model calcu-
lated by Hasegawa and Yanase[16].

Table 3-5

Fermi surface cross sections at the symmetry axes.

$\vec{B}$	Branch	Cross section obtained by dHvA measurement (in units of 10^{19} m^{-2})		Cross section calculated theoretically (in units of 10^{19} m^{-2})			
		Present study	Arko et al.	Hasegawa et al. $\alpha=1.0$	$\alpha=2/3$	Walch et al. $\alpha=1.0$	$\alpha=0.7$
[001]	α	7.54	7.54	7.11	7.15	7.5	5.4
	γ	3.08	3.07	3.22	3.41		4.3
	ε	0.808	0.82	0.850	0.725		2.1
[111]	α	8.14					
	β	7.65					
	ζ	0.204					
[110]	α	8.79					
	α	7.93					
	δ	0.50	0.54				

with the experimental α-Fermi surface. However, the calculated neck-Fermi surface is considerably larger than the experimental one. Later they improved their band structure calculation by taking into account the effect of La-4f states[61]. In fact, the mixing between B-2p states and the La-4f states distorts the B-sp bands and La-5d bands appreciably, resulting in a markedly thin neck Fermi surface. The agreement between the calculation and the experimental result is considerably improved. The structures of the conduction and valence bands and the bonding nature of LaB_6 will be discussed in a later section refering to this band structure calculation.

3-2-2. The dHvA effect on ZrB_2 and TiB_2

(i) Results for ZrB_2

The dHvA oscillations were observed in the frequency range of 0.76×10^2 to 6.05×10^3 T. The oscillations labelled α and β were most easily detected because of the large amplitudes. The observed oscillations α, β, γ and δ in the $(10\bar{1}0)$, $(11\bar{2}0)$ and (0001) planes are shown in Fig.3-22. In the $(10\bar{1}0)$ plane the α oscillations have four branches in the vicinity of the [0001] direction, which degenerate at the [0001] direction. The highest and the 2nd highest frequency branches disappear at 78° and at 49°, respectively. The remaining two branches can be observed at the whole angular region. The α frequency branch which can be observed from the [$11\bar{2}0$] direction up to 19°, degenerates into the lowest frequency branch at the [$11\bar{2}0$]

direction. The α oscillations degenerate into two brancches

in the (0001) plane. In the (11$\bar{2}$0) plane, the higher frequency

branch near the [10$\bar{1}$0] direction can be observed up to 20° and

the lower frequency branch can be observed in the whole

angular region of the (11$\bar{2}$0) plane. Two other branches can be

observed again from 30° and 60° up to the [0001] direction,

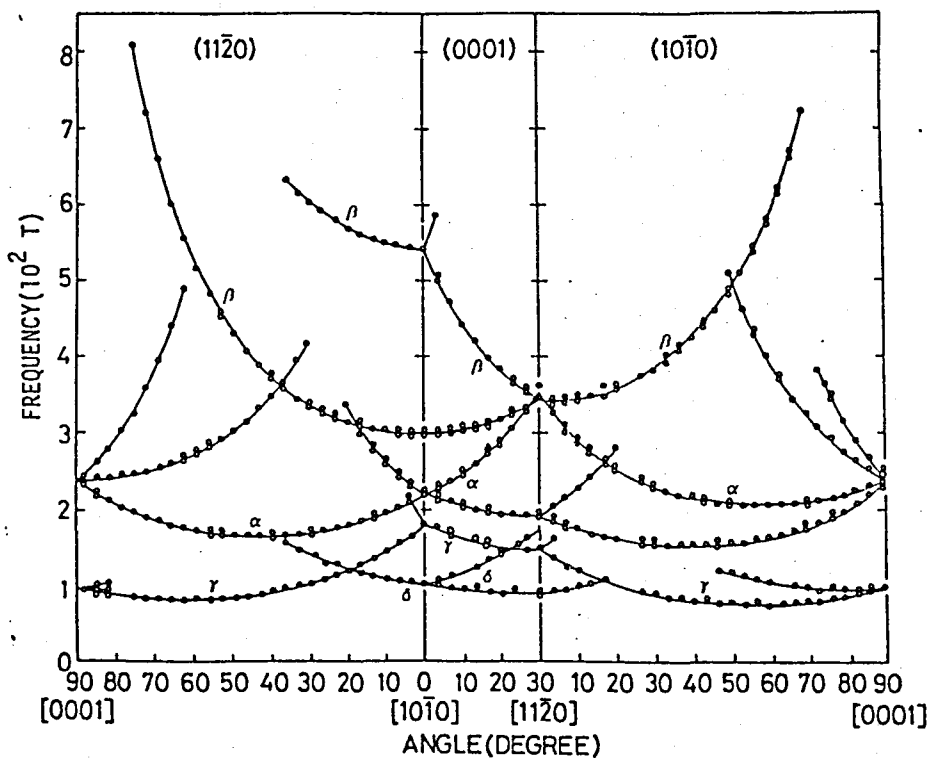respectively, and degenerate at the [0001] direction with their

Fig.3-22. Angular variations of the dHvA frequencies of
ZrB$_2$ of the order of 10^2 T.

frequencies decreasing. The α oscillations have a minimum value

of 1.54 x 10^2 T at 38° from the [11$\bar{2}$0] direction in the (10$\bar{1}$0)

plane.

The β oscillations have one branch in the (10$\bar{1}$0) plane,

which can be observed from the [11$\bar{2}$0] direction up to 70°.

In the (0001) plane, the β oscillations split into two branches
from the [11$\bar{2}$0] direction. The lower frequency branch
decreases its frequencies and reaches a minimum whose value is
3.00 x 10^2 T at the [10$\bar{1}$0] direction. The higher frequency
branch increases and degenerates with the decreasing frequency
branch at the [10$\bar{1}$0] direction, which can be observed only from
the [10$\bar{1}$0] direction to 3°. In the (11$\bar{2}$0) plane, the higher
frequency branch disappears at 37° and the lower frequency
branch can be observed till 75°.

The γ oscillations have rather similar behavior with the
α oscillations; however, some branches of the γ frequencies
can be observed in the very narrow angular regions and some
others are completely absent. For example, only two frequency
branches can be observed in the vicinity of the [0001] direction
in the (10$\bar{1}$0) plane. The minimum value of 0.76 x 10^2 T was
observed at 55° from the [11$\bar{2}$0] direction in the (10$\bar{1}$0) plane.

For the δ oscillations only one branch was observed from
the [10$\bar{1}$0] direction up to 37° in the (11$\bar{2}$0) plane and from the
[11$\bar{2}$0] direction up to 17° in the (10$\bar{1}$0) plane. The minimum
value of 0.94 x 10^2 T was observed at the [11$\bar{2}$0] direction.

The ε, μ, ν, ξ and ζ oscillations which have higher freq-
uencies of the order of 10^3 T are shown in Fig.3-23. The ε
oscillations have a minimum frequency of 1.81 x 10^3 T at the
[0001] direction. Their frequencies increase as the magnetic
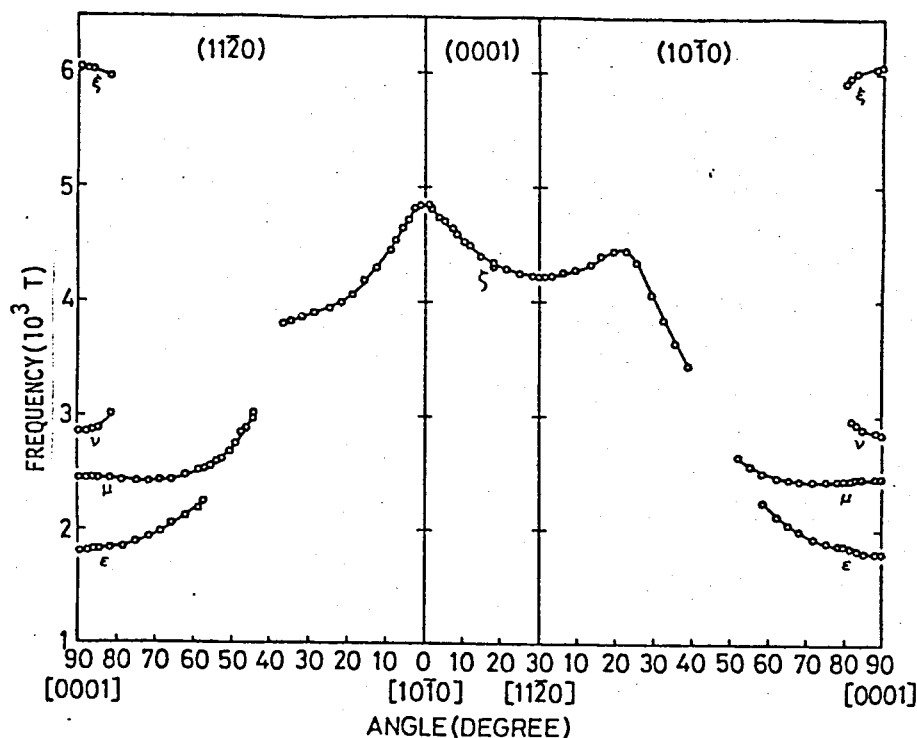field tilts away from the [0001] direction to 59° in the

Fig.3-23. Angular variations of the dHvA frequencies of ZrB$_2$ of the order of 10^3 T.

(10$\bar{1}$0) plane and to 57° in the (11$\bar{2}$0) plane. The μ oscillations whose frequency is 2.46 x 10^3 T at the [0001] direction, decrease their frequencies slightly as the field tilts away from the [0001] direction. Their frequencies increase rapidly after having a minimum value at about 20° from the [0001] direction in both planes, and they disappear suddenly at 51° and 44° in the (10$\bar{1}$0) and (11$\bar{2}$0) planes, respectively.

The ν and ξ oscillations were observed only from the [0001] direction to 81° in both (10$\bar{1}$0) and (11$\bar{2}$0) planes. The ν oscillations have a minimum frequency of 2.84 x 10^3 T at the [0001] direction. The ξ oscillations have a maximum frequency

-126-

of 6.05×10^3 T at the [0001] direction.

The ζ oscillations which have a maximum frequency of 4.86×10^3 T at the [10$\bar{1}$0] direction, decrease their frequencies rapidly as the angle increases from the [10$\bar{1}$0] direction in both the (11$\bar{2}$0) and (0001) planes. They disappear at 38° in the (11$\bar{2}$0) plane. Moreover, in the (10$\bar{1}$0) plane, their frequencies show a steep decrease after passing through a maximum value near 22° from the [11$\bar{2}$0] direction and disappear at 39°.

(ii) Results for TiB$_2$

The dHvA oscillations have been observed only in the frequency range of 0.7×10^2 to 4.6×10^2 T. The oscillations labelled α and β were most easily detected because of the large amplitudes. The observed oscillations in the (10$\bar{1}$0), (11$\bar{2}$0)
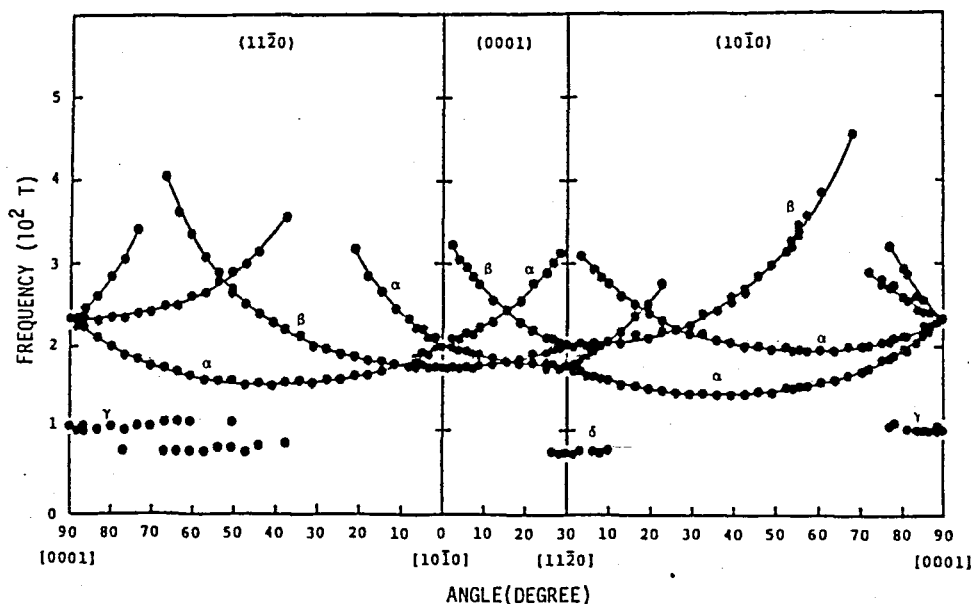
Fig.3-24. Angular variation of the dHvA frequencies of TiB$_2$ for field direction in the (10$\bar{1}$0), (11$\bar{2}$0) and (0001) planes.

-127-

and (0001) planes are shown in Fig.3-24. The α oscillations have four branches in the vicinity of the [0001] direction in the (10$\bar{1}$0) plane. However, only three branches were observed for nearly the same direction in the (11$\bar{2}$0) plane. Near the [11$\bar{2}$0] direction in the (10$\bar{1}$0) plane, three branches were observed and for almost the whole of the remaining region two branches were observed. A minimum frequency, 1.41 x 10^2 T, of the α oscillations was observed at 38° from the [11$\bar{2}$0] direction in the (10$\bar{1}$0) plane.

Two branches could be observed for the β oscillations in the (0001) plane. However, in both the (10$\bar{1}$0) and (11$\bar{2}$0) planes only one branch could be observed. Their frequencies have a minimum value of 1.75 x 10^2 T at the [10$\bar{1}$0] direction.

The γ oscillations have a frequency of 1.0 x 10^2 T at the [0001] direction. They were observed in both the (10$\bar{1}$0) and (11$\bar{2}$0) planes within the angular regions of 50° and 10° from the [0001] direction, respectively.

The δ oscillations could be observed only in the vicinity of the [11$\bar{2}$0] direction. Their value stays at about 0.75 x 10^2 T.

(iii) Fermi surface

Before constructing the whole Fermi surface, it is instructive to compare the observed dHvA frequencies with that expected from the previous experiment or the electron transfer theory.

Piper[14] estimated the electron and hole concentrations of ZrB_2 to be 0.06 per unit cell according to the two band model. Assuming a spherical Fermi surface having electron(hole) concentration of 0.06 per unit cell, the dHvA frequency is expected to be about 5×10^3 T. This value seems to be rather high as compared with the observed frequencies. However, there are many branches in the dHvA oscillations of ZrB_2 and their angular dependences are so complicated that the Fermi surface must be complicated. Therefore, each piece of the Fermi surface may have a rather small cross section and the corresponding dHvA frequency is expected to have a lower value than the above estimated value. The carrier concentration expected from the dHvA frequencies observed may be of the same order of magnitude as Piper's estimation.

On the other hand, as described in chap.1, it has been believed that the electron transfer model is applicable to the case of the diborides; two valence electrons of each metal atom are donated to the boron aggregate in order to make the characteristic two dimensional boron network isoelectronic with a monolayer of carbon atoms in graphite. Therefore the conduction electron concentration of both ZrB_2 and TiB_2 is two electrons per unit cell. The volume of the free electron Fermi sphere coincides with the volume of the Brillouin zone. Both ZrB_2 and TiB_2 have the hexagonal Brillouin zone. The free electron Fermi sphere fills almost the whole of the 1st zone and terminates outside the 1st zone. Any pieces of the

sphere which lie outside the 1st zone can be reduced to lie
within the 1st zone through a suitable reciprocal lattice
vector. The detailed shapes of the Fermi surfaces by the
reduced zone scheme depend on the geometry of the crystal
lattice. Their dHvA frequencies can be estimated by assuming
that a radius of some extremal cross section of the Fermi
surface on the reduced zone scheme is approximated by the
distance between the zone boundary of the 1st zone and the
surface of the free electron Fermi sphere. The estimated
frequency of ZrB_2 ranges $8 \sim 23 \times 10^2$ T which is comparable to
the experimental frequency. It is difficult to judge at this
stage which model gives better agreement with the results of
the dHvA experiments. Construction of the Fermi surface is
necessary.

For convenience, a hexagonal Brillouin zone is shown in
Fig.3-25.

ZrB_2: Let us begin to note the charac-
teristics of each dHvA oscillation.
In the observed angular regions, the
frequencies of α and β oscillations
obey a proportionality relation:
$1/F^2 = A + B\cos^2\theta$ having a positive A,
where F means the dHvA frequency, so

Fig.3-25. Hexagonal Brillouin
zone.

that it was concluded that they come from a set of nearly
ellipsoidal Fermi surfaces. A major axis of the α-Fermi

-130-

surface points to a direction of 38° from the [11$\bar{2}$0] in the

(10$\bar{1}$0) plane. That of the β-Fermi surface points to the

[10$\bar{1}$0] direction. The ε, μ and ζ oscillations seem to come

from a dumbbell Fermi surface which has anisotropy. That is,

the ε and μ oscillations arise from orbits around the hyperbolic

part and the lobes, respectively, and the ζ oscillations can

be assigned to arise from the orbit running around the

"dumbbell". The δ oscillations give a set of rod-shaped

surfaces along the [11$\bar{2}$0] direction.

At first, it was tried to construct the Fermi surface

refering to the band structure calculation of CrB_2 by Liu et

al.[62] since there were no band structure calculations of ZrB_2

at the time when this experiment was done. In the case of the

transition metal diborides, it seems that their band structures

can be approximated by applying the rigid band model to the

band structure of CrB_2, because the density of states curve of

CrB_2 can explain their γ-values of the electronic heat capacity

by simply making an appropriate shift of the Fermi level.

In the case of ZrB_2 such a shift of the Fermi level indicates

that the electron Fermi surfaces exist on KM and ΓK lines and

a hole Fermi surface exists at the A point. Then it was

tentatively assumed that the ellipsoidal Fermi surfaces

corresponding to the β oscillations cut across the KM line and

are connected to each other by δ-Fermi surfaces, forming a

ring-like electron surface around the K point, then the ν and

ξ oscillations can be assigned to come from the orbits running

around the inner and outer parts of this ring, respectively.

On the other hand, the dumbbell-like Fermi surface correspond-

ing to the ε, μ and ζ oscillations are assigned as the hole

Fermi surface around the A point.   If ZrB_2 is expected to be

a compensated semi-metal as Piper pointed out and also as

it is supported by the band structure above inferred, con-

centrations of electrons and holes must coincide each other. The

hole concentration estimated from a model of the dumbbell-like

Fermi surface was considerably higher than that of electrons

estimated from the ring-like Fermi surface consisting of the β-

and δ-Fermi surfaces.   In order that both concentrations of

electrons and holes coincide, the α-Fermi surface must be an

electron Fermi surface.   Judging from the angular dependence

of the α oscillations, they correspond to at least six or

twelve equivalent Fermi surfaces.   However, six α-Fermi surfaces

are sufficient in order to satisfy the requirement of compensa-

tion.   Apparently, each piece of the α-Fermi surface does not

form a closed Fermi surface so that they are expected to be

joined together with the ring-like electron Fermi surface.

The joining points were estimated to be at points where the

ring-like Fermi surface crosses ΓK line, taking into account

the symmetry of the α-Fermi surface.

For further confirmation of the estimated Fermi surface

of ZrB_2, a detailed band structure calculation is needed.

Fortunately, Ihara et al.[63] calculated the band structure

of ZrB_2 using APW method, which explains relatively well the

X-ray photoelectron spectrum of the valence band, the available

experimental data of a low temperature heat capacity and a

reflectance measurement. He was stimulated to calculate the

Fermi surface of ZrB_2 by the present experimental results.

His results[17] showed the existence of a ring-like electron

Fermi surface around the K point to which the nearly ellipsoidal

Fermi surfaces are joined together at the point where the ring-

like Fermi surface crosses the ΓK lines, and of a wrinkled

dumbbell-like hole Fermi surface at the A point which has an

anisotropy between the [$10\bar{1}0$] and [$11\bar{2}0$] directions. There-

fore, the Fermi surfaces estimated experimentally are correctly

confirmed. Then the γ oscillations are assigned to come out

from the orbit of the connection part between the α-Fermi

surface and the ring-like Fermi surface.

A proposed Fermi surface model of ZrB_2 is shown in Fig.3-26
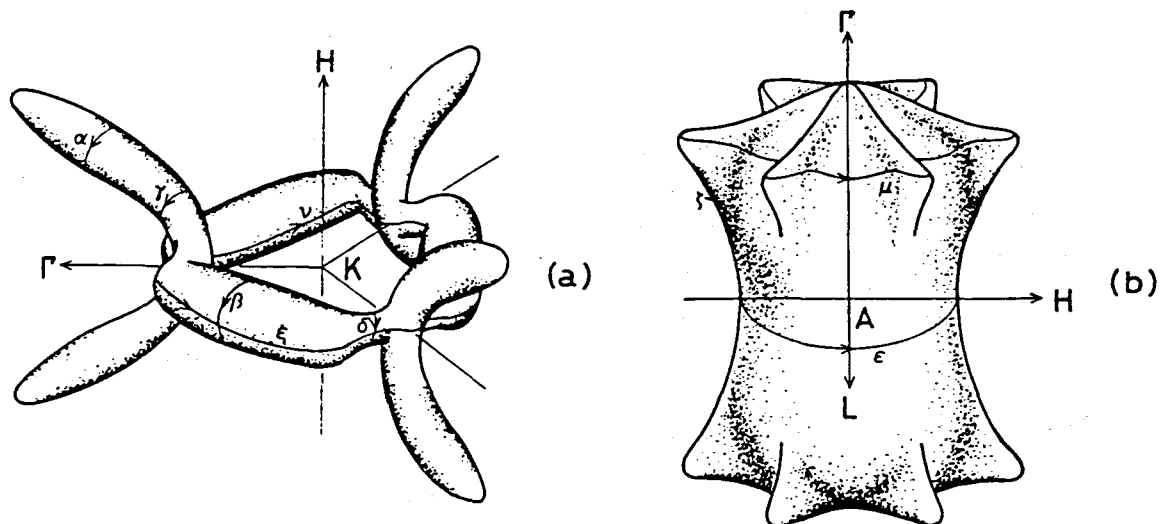
Fig.3-26. Fermi surface model of ZrB_2.

(a) Electron and (b) hole surfaces.

where the theoretical Fermi surface by Ihara was modified to fit the cross sectional areas of Fermi surface to those obtained by dHvA measurements at several particular directions. No other Fermi surface seems to exist since the dHvA oscillations which could not be assigned to the present Fermi surface model, have not been observed. This is supported also by the theoretical calculation. By using the Fermi surface model in Fig.3-26, the electron and hole concentrations were roughly estimated to be 0.038 and 0.043 per unit cell, respectively. This indicates that the electrons and holes are almost compensated by each other. In conclusion, ZrB_2 is a semi-metal with electron (hole) concentration of about 0.04 per unit cell.

TiB_2: The APW calculation by Ihara[17] showed that the band structure of the isostructural TiB_2 and ZrB_2 closely resemble each other. Their bands cross the Fermi level at almost the same positions in the Brillouin zone. It is reasonable to consider that TiB_2 has a similar Fermi surface with that of ZrB_2. The angular dependence of the observed oscillations in TiB_2 resembles that of those oscillations in ZrB_2 whose frequencies are of order of 10^2 T and which have been assigned to corresond to the electron Fermi surface. The frequency of the $\alpha (TiB_2)$ oscillations whose angular dependence almost coincides with that of the $\alpha (ZrB_2)$, is only 8 % smaller than the $\alpha (ZrB_2)$ frequency at the minimum cross section direction. The number of the frequency branches is the same as that of

the $\alpha(ZrB_2)$. The $\beta(TiB_2)$ oscillations have a 58 % smaller minimum frequency than that of the $\beta(ZrB_2)$ at the $[10\bar{1}0]$ direction. The $\beta(TiB_2)$ oscillations have fewer frequency branches than the $\beta(ZrB_2)$. It may be due to the relatively low RRR value of the TiB_2 specimen so that higher β frequencies could not be observed for TiB_2. The frequency of the $\gamma(TiB_2)$ oscillations is just equal to that of the $\gamma(ZrB_2)$ at the $[0001]$ direction. The $\delta(TiB_2)$ frequency is 75 % of the $\delta(ZrB_2)$ frequency at the $[11\bar{2}0]$ direction.

An electron Fermi surface of TiB_2 can be constructed by modifying the electron Fermi surface of ZrB_2. As mentioned in the last section, ZrB_2 has a ring-like electron Fermi surface around the K point. Nearly ellipsoidal Fermi surfaces are joined together with it on ΓK lines. In the case of ZrB_2, the ν and ξ oscillations near the $[0001]$ direction were observed and were assigned to the inner and outer orbits running around the ring. Therefore, the dimensions of the ring could be determined. In the case of TiB_2, however, the corresponding oscillations could not be observed, making it difficult to determine the dimensions of a ring as a whole. The observed angular region ($0°$ to $67°$) of the $\beta(TiB_2)$ oscillations in the $(11\bar{2}0)$ is slightly narrower than that ($0°$ to $75°$) of the $\beta(ZrB_2)$ oscillations. Furthermore, it is found that the observed β-Fermi surfaces of TiB_2 and ZrB_2 have an ellipsoidal shape, judging from the fact that the β frequencies are expressed as $1/F^2 = A + B\cos^2\theta$ ($A > 0$, F means frequency).

Tentatively, it was assumed that the β (TiB$_2$) oscillations could be observed within the same angular region of the β (ZrB$_2$) oscillations. That is, the data on β (TiB$_2$) was extrapolated to cover the same angular region as the corresponding β (ZrB$_2$). A length along the long axis of the β-Fermi surface of TiB$_2$ was estimated to be about 3.9×10^9 m^{-1} under this assumption. This value is about 80 % of that of ZrB$_2$. The electron Fermi surface of TiB$_2$ constructed by the above procedure is shown in Fig.3-27. Cross section of the Fermi surface at high symmetry planes in the Brillouin zone is shown in (a) and the whole shape of the Fermi surface is

(a)

(b)
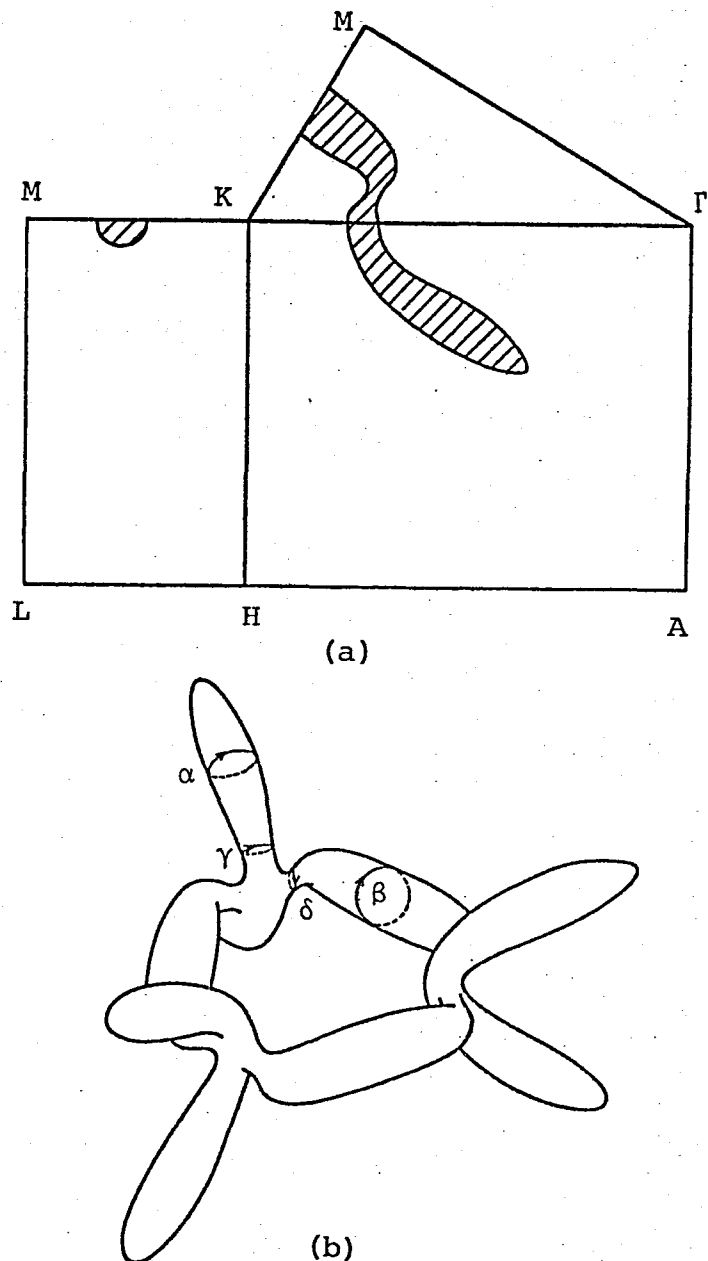
Fig.3-27. Fermi surface model of TiB$_2$.
(a) Cross section and (b) whole shape.

-136-

shown in (b). By using this Fermi surface model, the electron

concentration was estimated to be about 0.023 per unit cell.

This value is about half of that of ZrB_2. TiB_2 is considered

to be a semi-metal because of the small carrier concentration

and the similarity of energy band structure and Fermi surface

with those of ZrB_2. In conclusion, TiB_2 is a semi-metal with

electron (hole) concentration of about 0.02 per unit cell.

The frequencies of the selected extremal cross sections of

both ZrB_2 and TiB_2 are summarized in Table 3-6. The present

Table 3-6

The selected extremal cross section of both ZrB_2 and

TiB_2.

Branch	Direction	Cross section(10^{18} m^{-2})		
		ZrB_2	TiB_2	
α	38° from [11$\bar{2}$0] in (10$\bar{1}$0) plane	1.47	1.35	
β	[10$\bar{1}$0]	2.87	1.67	
γ	55° from [11$\bar{2}$0] in (10$\bar{1}$0) plane	0.73	0.96	[0001] direction
δ	[11$\bar{2}$0]	0.90	0.72	
ε	[0001]	17.3		
μ	[0001]	23.5		
ν	[0001]	27.1		
ξ	[0001]	57.8		
ζ	[10$\bar{1}$0]	46.4		

Fermi surface experiment were explained well by the Ihara's

band structure calculation, then his band structure calculation

is sufficiently reliable. However, his calculation is not

a self-consistent one, causing a difficulty of estimating the contribution of various atomic states to each band. Recently, Johnson et al. [64] carried out the self-consistent calculation for ZrB_2. The correspondence between their band structure calculation and the present Fermi surface experiment is obscure because they did not calculate the Fermi surface. Though, the energy dispersion relation of their band structure resembles that of Ihara's calculation rather well. On the other hand, the tight binding calculation by Perkins and Sweeney on TiB_2 [65] does not agree with the present dHvA result. The conduction band and valence band structures and the bonding nature of the diborides will be discussed at sec.3-3 refering to both the calculations by Ihara and Johnson et al.

3-2-3. The elastic constant of LaB_6

The observed sound velocities are summarized in Table 3-7 together with the calculated elastic constants using the least square method. The anisotropic factor $A=2C_{44}/(C_{11}-C_{12})$ is 0.41. LaB_6 has considrably high elastic constants corresponding to its high hardness. The elastic constants of LaB_6 are compared with those of the refractory materials having cubic symmetry in Table 3-8. Little data on the elastic constants have been reported for other borides. The C_{11} value of LaB_6 is about half of that of diamond and is comparable with the values for the refractory metals Mo and W and the refractory carbide of TiC. The elastic constants of the refractory oxides are

-138-

Table 3-7

Sound velocities and elastic constants of LaB_6

1. Sound velocity

Propagation direction	Type	Polarization	Observed velocity (m/sec)	rms velocity (m/sec)
[001]	L		9793	9810
	T	[1$\bar{1}$0]	4362	
[110]	T_1	[001]	4335	4374
	T_2	[1$\bar{1}$0]	6830	6796
[111]	L		7779	7756

2. Elastic constant (N/m)

$$c_{11}=45.33 \times 10^8, \quad c_{12}=1.82 \times 10^8, \quad c_{44}=9.01 \times 10^8$$

$$A=2c_{44}/(c_{11}-c_{12})=0.41$$

Table 3-8

Comparison of the elastic constants of LaB_6 with other refractory materials (in units of 10^8 N/m).

Material	c_{11}	c_{12}	c_{44}	Reference
LaB_6	45.33	1.82	9.01	
Diamond	107.6	12.5	57.6	[66]
Mo	44.1	17.2	12.2	[67]
W	52.1	20.2	16.0	[68]
TiC	50.0	11.3	17.5	[69]
UC	32.0	8.4	6.5	[70]
MgO	28.9	8.8	15.5	[71]
$Y_3Al_5O_{12}$	29.0	11.7	11.5	[72]

slightly lower than those of LaB$_6$.

The Debye temperature Θ is a convenient quantity to use in discussing the elastic property of solids and the interactions of phonons with other excitations. Betts et al.[73] gave a detailed expression for the Debye temperature of cubic crystals using the elastic constants. Their six-term approximation gives an error of no more than 3 % when the Debye temperatures of some metals and alkali halides were calculated, as long as their anisotropy factors fall in the range of 0.25< A< 4. The Debye temperature is expressed as

$$\Theta = (h/k_B) \, (9s/\Delta)^{1/3} J^{-1/3},$$

where Δ is the unit cell volume, s the number of atoms per unit cell and h and k_B have their usual meanings. J is a numerical function of the crystal density and the elastic constants.

The Θ$_{elast.}$ obtained for $s=7$ is 773 K. This value differs far from the calorimetric Debye temperature Θ$_{calor.}$ of 407 K measured by Etourneau et al.[11] at low temperature. This difference will be ascribed to the peculiarity of the crystal structure of MB$_6$.

The bonding between the metal atom and the boron framework is believed to be weak. The lattice vibration modes of hexaborides can be classified into three types; (1) boron lattice solely vibrates, (2) metal atom vibrates coincidently with boron lattice and (3) metal atom almost solely vibrates in the boron framework. The second type corresponds to the

acoustic type vibrations. The $\Theta_{elast.}$ is reflected mainly by the frequency of the second type vibration.

Since dominant bonding in LaB_6 is the covalent B-B bond, the Debye temperature of LaB_6 can be compared with that of elemental borons and compounds rich in boron content if the mass and density effects are taken into account. Those elemental borons and boron compounds are expected to have the same type of covalent B-B bond with LaB_6.

The $\Theta_{elast.}$ of LaB_6 is connected with that of elemental borons and boron compounds using a scaling law: $\Theta = b(\bar{M}\delta^3)^{-1/2}$ [74] where b is some constant, $\bar{M}$ the average atomic mass and δ^3 the average volume per atom. This scaling law says that the Debye temperature of the compounds having the same type of dominant bonding is proportional to $(\bar{M}\delta^3)^{-1/2}$ having equal b.

Table 3-9

Debye temperature and related parameters of LaB_6, elemental borons and boron compounds.

Material	$\bar{M}$ (g)	δ (10^{-1} nm)	Θ (K)
LaB_6	29.1	2.17	773
α-boron	10.81	1.94	1430
β-boron	10.81	1.99	1300
$B_{12}C_3$	11.05	1.94	1300
$B_{12}P_2$	13.69	2.06	1160
$B_{12}As_2$	19.97	2.10	940
YB_{66}	11.98	2.00	1300

Each parameter of LaB_6, α-boron, β-boron, $B_{12}C_3$, $B_{12}P_2$, $B_{12}As_2$ and YB_{66} [75] is summarized in Table 3-9.

The Θ values of LaB_6, β-boron, $B_{12}C_3$ and YB_{66} are the observed ones. Those of α-boron, $B_{12}P_2$, $B_{12}As_2$ are the estimated ones using the scaling law assuming that their b value coincides with that of β-boron, $B_{12}C_3$ and YB_{66}. Such an estimation is reliable because their lattice thermal conductivities calculated using the Debye temperatures thus estimated agree well with the observed thermal conductivities [75]. The Θ values are plotted in Fig.3-28 as function of $(\bar{M}\delta^3)^{-1/2}$. The $\Theta_{elast.}$ of LaB_6 is well expressed by the scaling law. In conclusion, the B-B bonding in LaB_6 has a comparable bonding force with the B-B bonding in those elemental borons and boron compounds. LaB_6 has heavier average atomic mass so that the $\Theta_{elast.}$ of LaB_6 is low as compared with those of the elemental borons and the boron compounds.

Fig.3-28. Debye temperatures of LaB_6, elemental borons and boron compounds are plotted according to the scaling law of $\Theta=b\,(\bar{M}\delta^3)^{-1/2}$.

The strength of the B-B bonding in LaB_6 appears directly in the first type vibration modes in which the boron lattice solely vibrates. Several of them are Raman active and were

observed by Ishii and Tanaka[76]. The Raman active modes of
A_{1g}, E_g and F_{2g} have wave number of $1.258 \times 10^5 \text{ m}^{-1}$, 1.120×10^5
m^{-1} and $6.58 \times 10^4 \text{ m}^{-1}$. These frequencies lie in the same
energy region of the Debye temperatures of the elemental borons
and the boron compounds. These Raman frequencies should have
a correlation with the elastic constants. This can be done
through Young's modulus. Ishii[77] obtained the force constant
of the B-B bonding in LaB_6 by analyzing the Raman frequencies
using the molecular vibration model. He found the force
constants of the intra- and inter-boron octahedron B-B bondings
to be $K_{intra}=1.28 \times 10^2$ N/m and $K_{inter}=2.18 \times 10^2$ N/m,
respectively. According to a method developed by Shimanouchi
et al.[78], the Young's modulus E along the [100] direction is

$$E= (F_d/A) (\Delta d/d)$$

where d is the lattice constant along the [100] direction, i.e.
0.41568 nm, Δd the increment of d, A the effective cross
sectional area, $F_d=\partial V/\partial d$ the force constant along the [100]
direction and V is the potential energy expressed by the
equation;

$$V=\frac{1}{2}K_{inter} (\Delta r_{inter})^2 + \frac{8}{2}K_{intra} (\Delta r_{intra})^2$$

and

$$\Delta d = \Delta r_{intra} + \Delta r_{inter}$$

Assuming that A is cross section of the octahedron perpendicular
to the [100] direction and calculating the [100] component of
K_{intra}, the Young's modulus was estimated to be 4.0×10^{11} N/m^2.

The Young's modulus $E_{[100]}$ is calculated from the elastic

constants to be 4.52 x 10^{11} N/m^2 using the expression of

$$E_{[100]} = (C_{11} + 2C_{12})(C_{11} - C_{12})/(C_{11} + C_{12}).$$

Both agree relatively well. Thus the elastic property of LaB$_6$

is mainly determined by the B-B bonding. The vibration frequency

of the metal-boron bonding is about one tenth of those of the

B-B bondings as will be described in the next section. The

metal-boron bonding contributes little to the elastic property

of LaB$_6$.

3-2-4. Heat capacity of LaB$_6$

The measured heat capacity above 120 K is shown in Fig.3-29

together with the low temperature value below 77 K which was

measured by Fujita
[79] using the LaB$_6$
crystal prepared in
this study. Between
77 K and 120 K, the
values of the heat
capacity were inter-
polated. The
difference of the
constant pressure
heat capacity and
the constant volume
one is expressed as
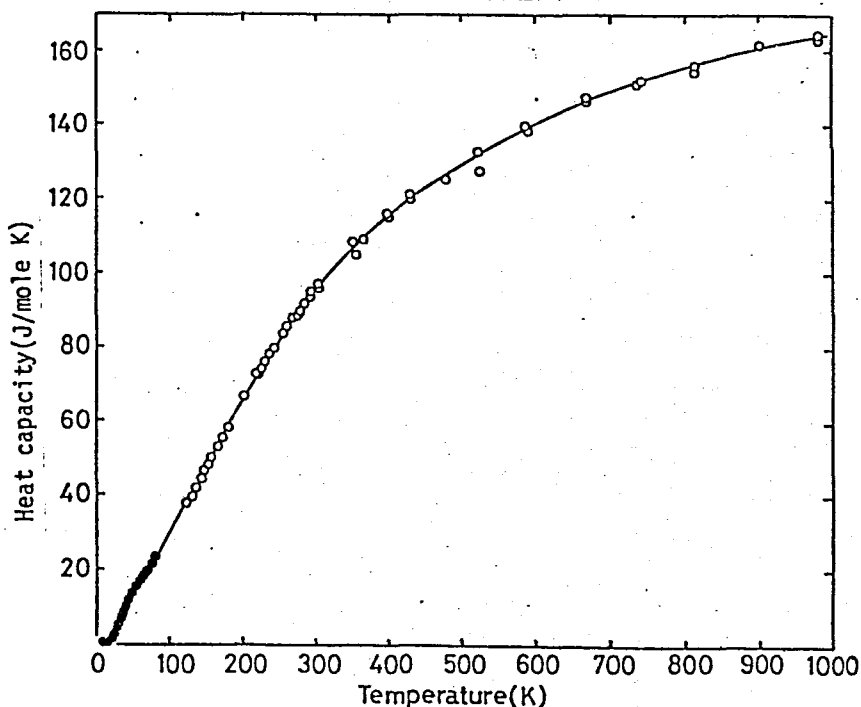
Fig.3-29. Heat capacity of LaB$_6$.

$C_p - C_V = 9\alpha^2 BVT$, where α is linear thermal expansion coefficient, B the bulk modulus and V the volume. Since α is about 5×10^{-6}/K and B is 5×10^8 N/m at room temperature, $C_p - C_V$ is of the order of 10^{-3} J/mole·K and is neglible.

The lattice part of the heat capacity which is shown as a solid line in Fig.3-30 was obtained by subtracting the electronic heat capacity from the measured values. The electronic heat capacity was calculated by assuming that it has a temperature dependence of γT in the whole temperature region. The γ value was estimated to be 2.6 mJ/mole·K^2 from a C/T vs. γT^2 relation in the low temperature region. The estimated γ-value agrees with the value by Etourneau et al.[11].
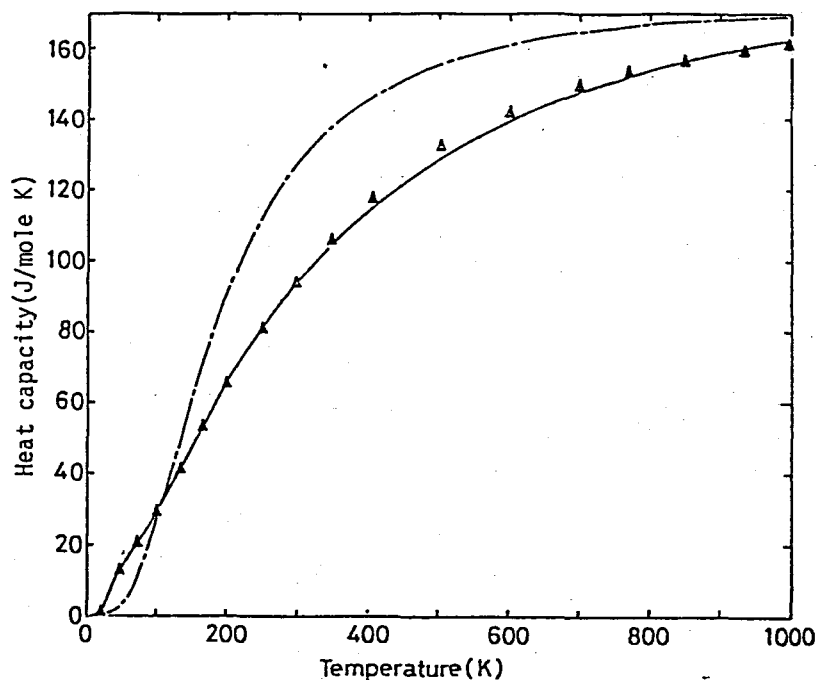
Fig.3-30. Lattice heat capacity of LaB$_6$(solid line), Debye's heat capacity curve with Θ_D=773 K(dash-dot line and the calculated value(solid triangular).

The lattice heat capacity has a little hump at about 50 K. For other magnetic hexaborides, the Schottky anomalies are observed in this temperature range; however, in LaB$_6$ apparently it must be a phonon contribution. On increasing

the temperature, the lattice heat capacity curve raises rapidly
in the low temperature region. In that temperature region
there is a large difference between the observed lattice heat
capacity and the Debye's heat capacity curve (dash-dot line in
Fig.3-30) of single parameter Θ=773 K which is the elastic
Debye temperature. However, the measured heat capacity decreases
the inclination at about 50 K and crosses the Debye function at
about 100 K. The lattice heat capacity above the room temperature
is far below the Debye function.

The characteristic feature of the temperature dependence
of the lattice heat capacity can be understood more clearly by figuring the temperature dependence of the calorimetric Debye temperature as shown in Fig.3-31.

Fig.3-31. Temperature dependence of the calorimetric
Debye temperature of LaB_6. Solid line and dotted line
show the experimental and the calculated Debye tempera-
ture, respectively.
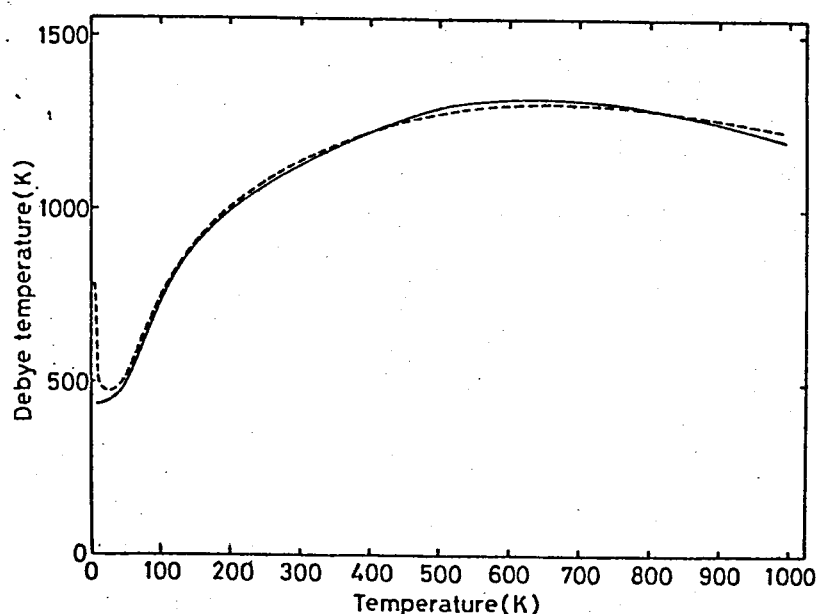
The value of calorimetric Debye temperature is over 1000 K in the wide temperature range from 200 K to 1000 K.
The high-hardness property of LaB_6 due to the strong B-B
bonding appears clearly in this temperature region.

The low value of the calorimetric Debye temperature is observed only in the temperature range below 100 K. This fact suggests that there are some energetically low-lying frequency modes in the lattice vibrations of LaB_6.

Kasuya et al.[80] presented a model; the rotational mode of B_6 octahedron has a large dispersion in the Brillouin zone. The rotational mode is of out-phase for neighboring octahedra at the Γ point. The frequency is relatively high (about 5×10^4 m^{-1}). The mode links to the in-phase rotational motion of neighboring octahedra at the zone boundary. They supposed that the energy of the in-phase rotational mode must be quite low, because such a mode does not contain a change of the inter-octahedron B-B distance in the first approximation. They estimated the frequency of the in-phase mode to be about 700 m^{-1} (10 K) at the zone boundary from the observed heat capacity value.

Such a rotational mode is the oscillational mode only of the boron lattice, i.e. a motion of the La ion does not take part in the mode. As mentioned in the last section, the Raman active modes which are two B-B stretching modes

Fig. 3-32. Observed Raman frequencies of metal hexaborides plotted against the lattice constant.

of A_{1g} and E_g symmetries and a boron lattice deformation mode of F_{2g} symmetry, are also the oscillational modes only of the boron
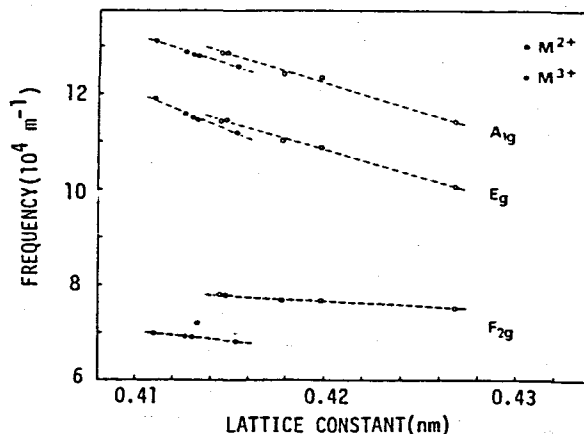
lattice. Ishii et al.[81] plotted the relation between the frequencies of those modes and the lattice constants for several hexaborides as shown in Fig.3-32. They found that the oscillation frequency is inversely proportional to the lattice constant. Thus the calorimetric Debye temperature at low temperature should be inversely proportional to the lattice constant since the rotational mode is thought to cause the low value of the calorimetric Debye temperature. As shown in Fig.3-33, $\Theta_{calor.}$ of some hexaborides does not seem to have any direct correlation with the lattice constant, where $\Theta_{calor.}$ values are those obtained by Etourneau et al.[11]. There is some doubt about the in-phase rotational mode model. Since the B-B bonding is covalent, it is resistive to bond angle bending. It is unlikely that the frequency of the in-phase rotational mode falls down so low even though it does not change the bond distance.

Fig.3-33. Debye temperatures of some hexaborides are plotted against their lattice constant.

By way of trial, $\Theta_{calor.}$ (~ 0 K) of those hexaborides is plotted with respect to $(\bar{M}\delta^3)^{-1/2}$ in Fig.3-34. It is found that $\Theta_{calor.}$ (~ 0 K) is linearly dependent on $(\bar{M}\delta^3)^{-1/2}$.
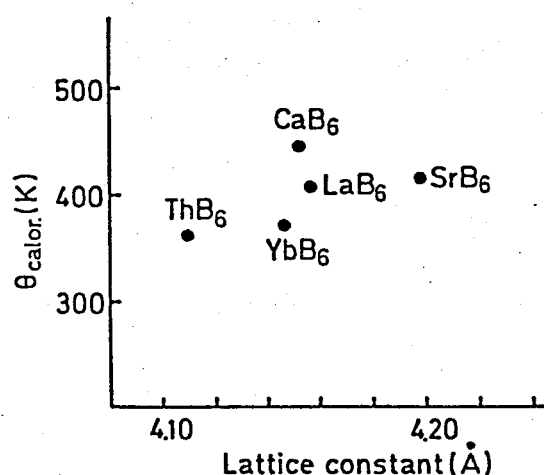
The change of the lattice
constant between each
hexaboride is relatively
small. δ^3 is nearly
constant. The change of
$\Theta_{calor.}$ ($\sim$0 K) is almost
dependent only on $(\bar{M})^{-1/2}$.
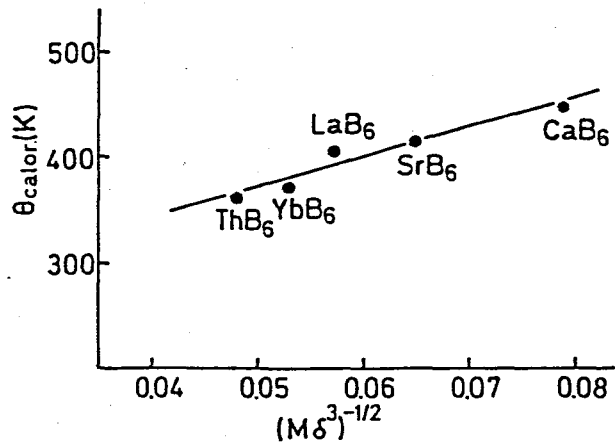Thus the energetically
low lying mode which is
the cause of the low value
of $\Theta_{calor.}$ ($\sim$0 K), is the

Fig.3-34. Debye temperatures of some
hexaborides are plotted against
$(\bar{M}\delta^3)^{-1/2}$.

mode containing cation motion, that is the M-B relative motion

mode. It is noteworthy that the M-B relative motion mode is

infrared active provided the bonding between metal atom and

boron atom is partly ionic. This mode becomes important for

the analysis of the electrical resistivity in the next section.

Phonon dispersion relation of LaB_6 is not clarified yet

though there are some experimental facts with respects to the

phonon frequency. Those are the elastic constants, the Raman

frequencies and the phonon density of states. Both the first

and second results are described in the last section. The

phonon density of states of LaB_6 was measured by Gumpf et al.

[82] in the energy region below 100 meV using the inelastic

neutron scattering experiment. They found that the energetically

lowest peak of the phonon dnesity of states lies at 13 meV

(150 K), followed by the peak at 36 meV(400 K) and the large

peak around 60∿70 meV(average 800 K). Ishii[83] calculated

the phonon dispersion relation of LaB$_6$ based on these results.

However, the known data are so little that some ambiguities

still remain in the calculation, especially at the region from

the middle to the boundary of the Brillouin zone.

It is necessary to correlate the calculated phonon

dispersion relation to other physical properties containing

the interactions between the phonons and other excitations.

However, it is difficult to analyze rigorously, for example,

the electrical resistivity and the lattice thermal conductivity

using the fully determined phonon dispersion relation. In

such cases, the analysis has been carried out usually using

the Debye model and/or the combination of the Debye model and

the Einstein model. The present heat capacity data are

analyzed by the latter method since there are so many phonon

modes in the lattice vibrations of the MB$_6$ crystal structure.

As described in the last section, the phonon modes of

LaB$_6$ are classified into three kinds of vibration modes.
The frequency and the mode number of each mode are assigned

refering to the experimental data and Ishii's analysis. The

frequency values will be expressed by the Debye temperature or

the Einstein temperature. The first vibration modes in which

the boron lattice solely vibrates, have frequencies around

Θ_E=800 K and around Θ_E=1500 K as seen from, for instance, the

Raman active modes. Mode number of each vibration mode is

nine and six, respectively. The second type of modes in which

the metal atom and the boron lattice vibrate coincidently,
corresponds to the acoustic modes. They can be expressed by
the Debye model whose Debye temperature is 400 K which is
reduced from the elastic Debye temperature by the factor of
$7^{1/3}$, since the mode number is three. In the last type of
modes, the metal atom vibrates almost solely in the boron frame-
work. Their frequencies must be very low because of the heavy
mass of the La atom and the weak bonding between the La atom
and the boron lattice. These M-B relative motion modes are
tentatively assigned to the energetically lowest peak of the
phonon density of
states. Their
Einstein temperature
is 150 K and the
mode number is
three. The above
assignments are
summarized in
Fig.3-35(a) (shown
as solid lines).

The numeral on each
mode shows their
mode number.
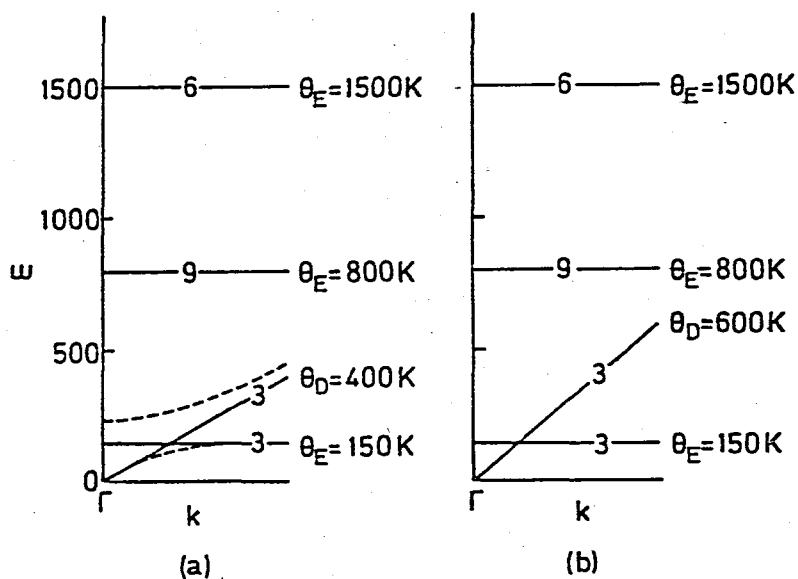
Fig.3-35. Phonon dispersion model of LaB_6. (a)Below
50 K and (b) above 50 K. Dotted curve in (a) shows
Ishii's analysis[81].

If the heat capacity is calculated using the vibration
model shown in Fig.3-35(a), the calculated heat capacity agrees
well with the observed one in the temperature range from 20 K

-151-

to 40 K. Beyond this temperature range, the calculated heat capacity increases faster than the observed one, indicating that the phonon frequencies assumed are too low for the phonons which begin to be excited as the temperature rises up beyond about 50 K. In fact, Ishii's analysis showed that the acoustic modes and the lowest energy optical modes mix with each other and they split as shown in Fig.3-35(a) with dotted line. This raises the frequencies of the upper mode, resulting in a slow increase of the heat capacity curve. It is not certain that such a phonon dispersion relation is the true one; however, the phonon dispersion relation in (a) shown as a solid line must be corrected to a certain extent. Better fit is obtained by setting the Debye temperature to be 600 K above 50 K. The latter model is shown in Fig.3-35(b). Two lattice vibration models are used separately in the two temperature regions; the former model is used below 50 K and the latter one above 50 K. The heat capacity thus obtained is shown in Fig.3-30 with triangular marks.

The calculated heat capacity shows good agreement with the observed one throughout the whole temperature region. The maximum deviation from the experimental data is observed around 500 K and the error is only about 5 %. This deviation is ascribed to the present over-simplified dispersion model in which many different optical modes are represented simply by only two modes of Θ_E=800 K and 1500 K. The phonon dispersion relation in (b) explains well not only the heat capacity curve but also the phonon contribution to the electrical resistivity and the lattice

thermal conductivity as will be discussed in the following
sections. It seems that the present simplified model approx-
imates the true phonon dispersion relation of LaB_6.

There remained a problem below 20 K. The contribution of
the optical phonons of $\Theta_E=150$ K to the heat capacity decreases
rapidly below 15 K. Correspondingly, the Debye temperature
calculated using the above lattice vibration model raises up
steeply in this temperature region as shown in Fig.3-31 with
a dotted curve. Finally it approaches and coincides with the
$\Theta_{elast.}$ of 773 K. The $\Theta_{calor.}$ obtained experimentally does
not increase even in this temperature region. It is unlikely
that there is some other oscillation mode whose frequency is
lower than the M-B relative motion modes of $\Theta_E=150$ K. This
phenomenon cannot be explained so long as the above lattice
vibration model is independent of temperature. There must
exist some phonon mode whose frequency decreases with decreasing
temperature

Tentatively the M-B relative motion modes of $\Theta_E=150$ K are
assigned to this temperature dependent frequency mode. The
variation of Θ_E can be estimated by the observed heat capacity
if the Debye temperature of the acoustic modes is fixed at 400 K.
The estimated Θ_E is 145 K at 20 K, 137 K at 15 K, 113 K at 10 K
and 65 K at 5 K. The variation of Θ_E is steep at low temperature.
Such a variation of Θ_E has not been confirmed experimentally yet.
Though the modes are infrared active, their energy ranges lie
within the far-infrared region. Moreover, LaB_6 is metallic

so that the infrared absorption experiment must be very difficult for reasons of both sample preparation and measurement. In fact, a trial of detecting this mode has failed. This experimental verification is a problem that still remains.

3-2-5. Electrical resistivity of LaB_6

The resistivity ρ of LaB_6 is shown in Fig.3-36 as a function of temperature. The resistivity at 300 K is 8.90×10^{-8} Ωm. Near room temperature, ρ varies as $T^{1.5}$, and below 70 K the inclination becomes steeper.
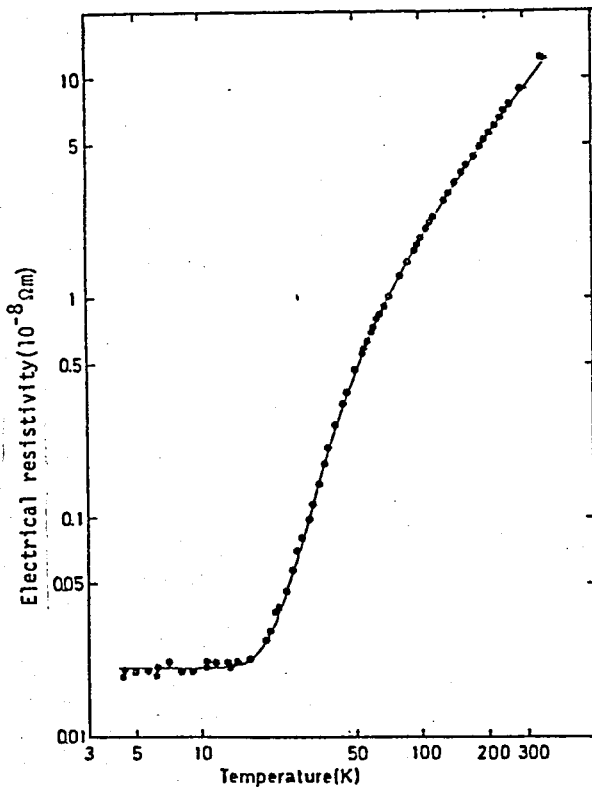
The intrinsic resistivity of the usual metals is caused by scattering of conduction electrons by acoustic phonons. Its temperature dependence is expressed as the Bloch-Grüneisen equation,

$$\rho = \rho_0 \left(\frac{T}{\Theta_R}\right)^5 J_5 \left(\frac{\Theta_R}{T}\right) \quad (1)$$

$$J_5(x) = \int_0^x \frac{z^5 \, dz}{(e^z - 1)(1 - e^z)} \quad (2)$$

where ρ_0 is a constant, Θ_R is defined as the Debye temperature of the electrical resistivity. Equation (1) is plotted as a function of ρ/ρ_0 vs. T/Θ_R in

Fig.3-36. Electrical resistivity of LaB_6.

Fig.3-37 as a solid line, wehre ρ_Θ is the resistivity at the Debye temperature. Experimental resistivities of Au, Na, Cu, Al and Ni are also plotted[82]. Their agreement with the equation (1) is quite good. The resistivity of LaB_6 is also

A Au θ=175K
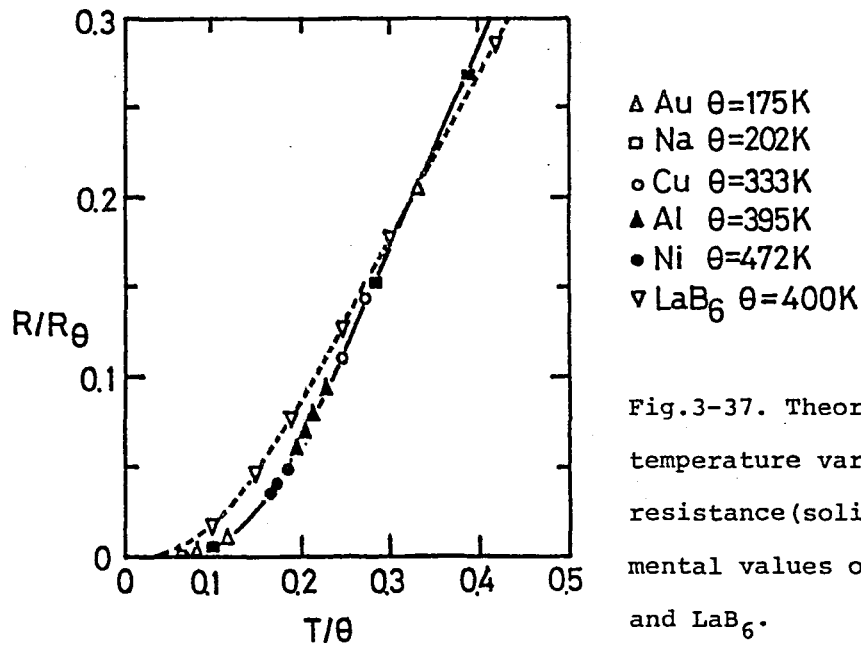□ Na θ=202K
○ Cu θ=333K
▲ Al θ=395K
● Ni θ=472K
▽ LaB₆ θ=400K

Fig.3-37. Theoretical(Grüneisen) temperature variation of electrical resistance(solid line), and experimental values of various metals[84] and LaB_6.

shown in Fig.3-37 as a dotted line assuming Θ_R=400 K. Since the resistivity at 400 K was not measured in this experiment, the value was interpolated from both the resistivities below 360 K and above 1100 K; the latter resistivities are shown in Fig.3-42. Apparently the temperature dependence of the resistivity of LaB_6 is different from that of the Bloch-Grüneisen equation. If Θ_R is assumed to be 773 K which is the elastic Debye temperature, this difference increases, that is, at Θ_R=400 K the difference from the Bloch-Grüneisen equation is rather small than that at Θ_R=773 K though the temperature dependence cannot be expressed by both Θ_R values. The former value is close to

the calorimetric Debye temperature obtained from low temperature
heat capacity. This suggests that the curious behavior of the
resistivity originates from the same phenomenon which causes
the calorimetric Debye temperature at low temperature to differ
from the elastic Debye temperature.

LaB$_6$ has the characteristic that as compared with the
common metals, it has many optical phonon modes. There is the
ionic character in the bonding between metal ion and boron
lattice. Phonon modes accompanying M-B relative motion cause
a change of the dipole moment. Such modes must scatter the
conduction electrons much more. An expression for the scatter-
ing has already been given for degenerate semiconductors by
Howarth and Sondheimer[85],

$$\rho_{op.} = \rho_0 [\frac{T}{\Theta_E} sinh^2 (\frac{\Theta_E}{2T})]^{-1}$$

where ρ_0 is a constant. Θ_E is the Einstein temperature of the
optical phonons. Equation (3) is proportional to T at high
temperature and rapidly approaches zero as $T^{-1} exp(-\Theta_E/T)$ at low
temperature. In the derivation of equation (3), the screening
effect of electrons on the optical phonons was not taken into
account. The screening effect will decrease the polar-mode con-
tribution to the resistivity through a dielectric constant but it
does not contribute so much to the temperature dependence. There-
fore, equation (3) is still a dood approximation for the temper-
ature dependence of the metallic compounds.

The present data were analyzed using the expression,

$$\rho(T) = A + B\left(\frac{T}{\Theta_R}\right)^5 J_5\left(\frac{\Theta_R}{T}\right) + C\left[\frac{T}{\Theta_E}sinh^2\left(\frac{\Theta_E}{2T}\right)\right]^{-1} \qquad (4)$$

where the constant A is the residual resistivity. In this equation Θ_R is correlated only with the acoustic phonons. Equation (4) was fitted to the data using a least-squares method which minimized $S(\Theta_R, \Theta_E)$, where $S(\Theta_R, \Theta_E)$ is defined as,

$$S(\Theta_R, \Theta_E) = \frac{1}{N-3}\Sigma_i\left[\frac{\rho_{obs.}(T_i) - \rho_{calc.}(T_i)}{\rho_{calc.}(T_i)}\right]^2$$

where $\rho_{obs.}(T_i)$ and $\rho_{calc.}(T_i)$ are the observed and calculated resistivities at a temperature T_i, respectively. N is the number of data. This procedure can determine A, B and C in equation (4) for given values of Θ_R and Θ_E. In order to determine the best fit values of (Θ_R, Θ_E), the contour map of S was written as function of Θ_R and Θ_E. The S map is shown in Fig.3-38.
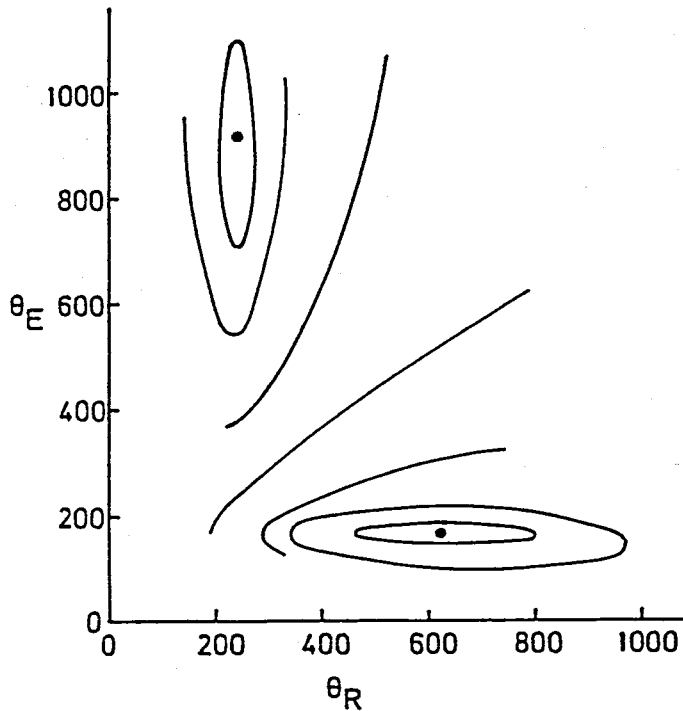

Fig.3-38. Contour map of S. Minimum points are located at $(\Theta_R, \Theta_E) = (620 \text{ K}, 165 \text{ K})$ and $(245 \text{ K}, 920 \text{ K})$.

The figure shows that there are two minimum points in the s map; $(\Theta_R, \Theta_E) = (620\ K,\ 165\ K)$ and $(245\ K,\ 920\ K)$. Parameters obtained are tabulated in Table 3-10. Both combinations of (Θ_R, Θ_E) fit data within the same order of magnitude.

The combination $(620\ K,\ 165\ K)$ agrees well with the combination of $(\Theta_{acoustic}, \Theta_{M-B}) = (600\ K, 150\ K)$ used for the heat capacity analysis above 50 K. Since the temperature dependence of the equation (1) and the equation (2) resemble each other except in the low temperature region, there is a minimum near the exchanged combination of (Θ_R, Θ_E). That is the

Table 3-10

Best fit parameters of the resistivity analysis.

Parameters	(Θ_R, Θ_E)			
	620 K	165 K	245 K	920 K
A	2.07×10^{-10} Ωm		1.99×10^{-10} Ωm	
B	3.35×10^{-7} Ωm		2.41×10^{-7} Ωm	
C	7.9×10^{-9} Ωm		3.48×10^{-8} Ωm	
S	1.24×10^{-3}		1.26×10^{-3}	

combination of $(245\ K,\ 920\ K)$, but this is of no practical value.

Contributions of the acoustic phonon term and the optical phonon term are shown in Fig.3-39. It is found that optical phonon scattering is dominant at low temperatures. As temperature increases, the acoustic phonon contribution appears. However, the optical phonon term is still larger than the acoustic phonon term even at room temperature. The fact that the resistivity due to the optical phonon scattering is dominant in the electrical resistivity of LaB_6, may not be taken

seriously, because the "real" phonon dispersion relation of LaB_6 is probably like that indicated by the dotted line in Fig.3-36(a). The distinction between the acoustic modes and the optical modes is ambiguous except near the Γ point in the Brillouin zone.
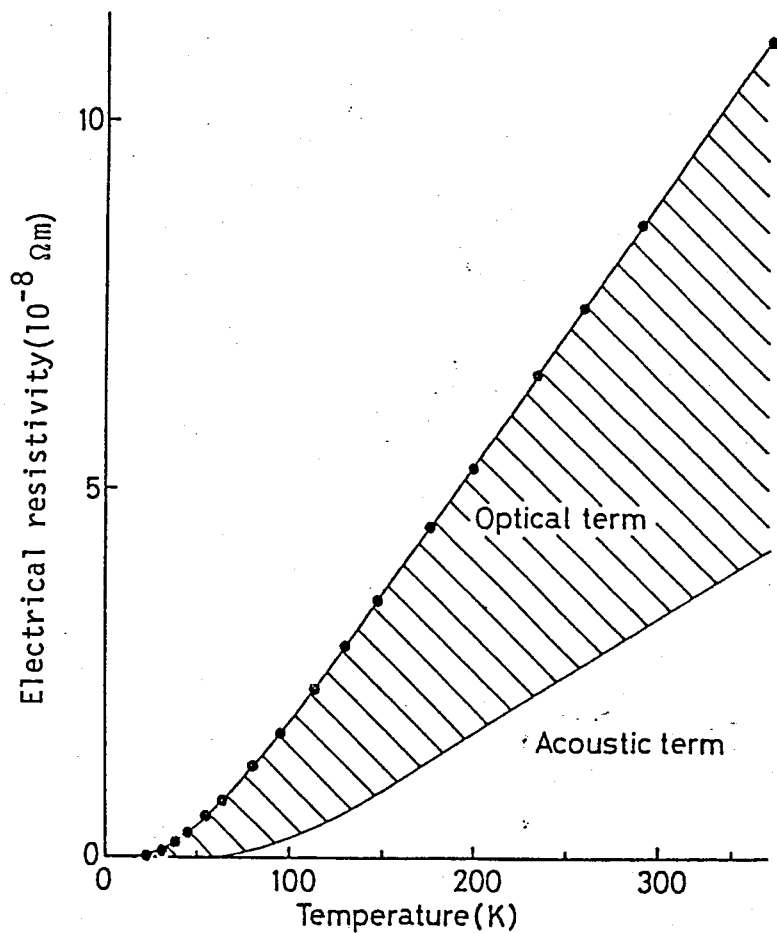
Fig.3-39. Contributions of the optical phonon term and the acoustic phonon term.

In conclusion, the combination of the M-B relative motion modes and the acoustic modes modifies the temperature dependence of the resistivity of LaB_6.

One should analyze the resistivity of LaB_6 using other scattering mechanisms. In the case of RuO_2 and IrO_2[86], the temperature dependences of their resistivity were analyzed using the electron-phonon and electron-electron interband scatterings. However, the Fermi sruface of LaB_6 consists of a multiply-connected surface of single band. The interband scatterings

ought not to exist. For confirmation, the resistivity of LaB_6 was analyzed using an expression,

$$\rho(T) = \rho_1 + \rho_2 T^2 + \rho_3 T^3 [J_3(\Theta_R/T) - J_3(\Theta_G/T)] + \rho_5 T^5 J_5(\Theta_R/T) \qquad [87]$$

where J_3 is the standard transport integral and Θ_G is a parameter characterizing a momentum gap between heavy and light mass bands. The ρ_2 and ρ_3 terms are attributed to the interband scattering and ρ_5 term is the acoustic phonon term. The ρ_3 term is a linear function of temperature at high temperatures and varies as T^3 at temperatures below $\Theta_R/5$. If the interband scattering contributes mainly to the resistivity, the temperature dependence of the resistivity at a relatively low temperature should become T^2 and/or T^3. However, the temperature dependence of the ideal resistivity of LaB_6 is steeper than T^3 at low temperatures. The values of Θ_R and Θ_G were estimated by fitting $\rho(T)$ to the experimental data, resulting in $\Theta_R = 400$ K and $\Theta_G = \Theta_R$. For such a combination of (Θ_R, Θ_G), the ρ_2 and ρ_3 terms became very small. Therefore, there are no interband scatterings.

A least-squares fit was also tried by adding a T^2 term to the right hand side of equation (4). But the coefficient of the T^2 term became negative as a result, implying that there is no possibility of an electron-electron intraband scattering in this temperature range.

There are two other examples of ReO_3 (Tanaka et al.[88] and King et al.[89]) and PdH[90] where the optical phonon scattering plays appreciable contribution to the resistivity. In these

compounds, since the values of Θ_E are higher than Θ_R, the optical phonon term is negligible at low temperature. However, in the ReO_3, it exceeds the acoustic phonon term at room temperature. This is reasonable because the bonding of ReO_3 is considerably ionic.

It has been suggested in the last section that the phonon frequency Θ_E of the M-B realtive motion mode changes as the temperature decreases below 20 K. In the present analysis of the resistivity, the combination (Θ_R, Θ_E) is fixed at (620 K, 165 K). The calculated intrinsic resistivity below 10 K is far smaller than the residual resistivity. Therefore, the calculated resistivity is almost constant in this temperature region, coinciding with the value of A. However, as can be seen in Fig.3-36, the experimental resistivity seems to decrease slightly with decreasing temperature from 10 K to 4.2 K though there are some scatterings in the observed data. If Θ_E varies as suggested in the last section, the optical phonon term can have an appreciable value till 4.2 K. The calculated resistivity will fit the temperature dependence of the observed data better. This supports the possibility of the temperature dependent behavior of the phonon frequency of the M-B relative motion mode.

3-2-6. Thermal conductivity of LaB_6

The plot of the thermal diffusivity against temperature is shown in Fig.3-40. The calculated thermal conductivity is

inversely proportional to temperature as shown in Fig.3-41, while the electrical resistivity of LaB_6, which is shown in Fig.3-42, is proportional to temperature.
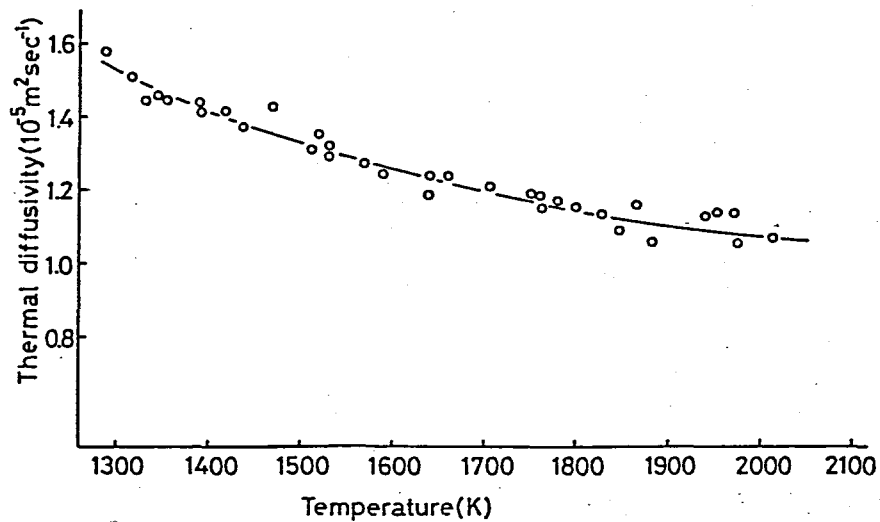

Fig.3-40. Thermal diffusivity of LaB_6 plotted against temperature.
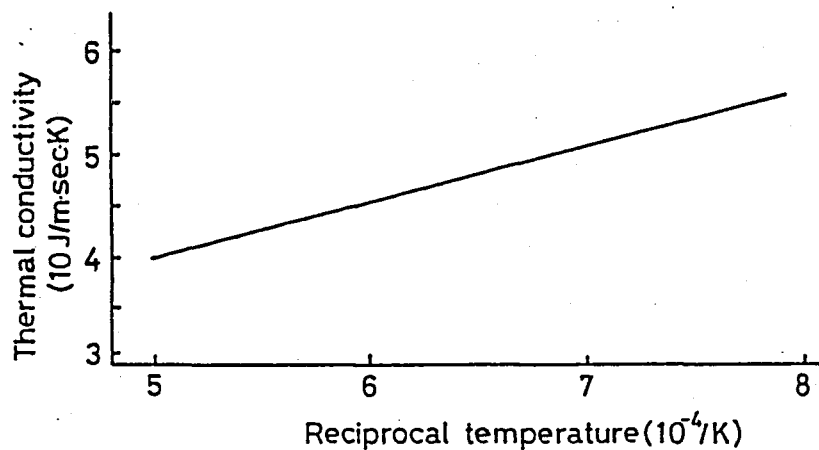

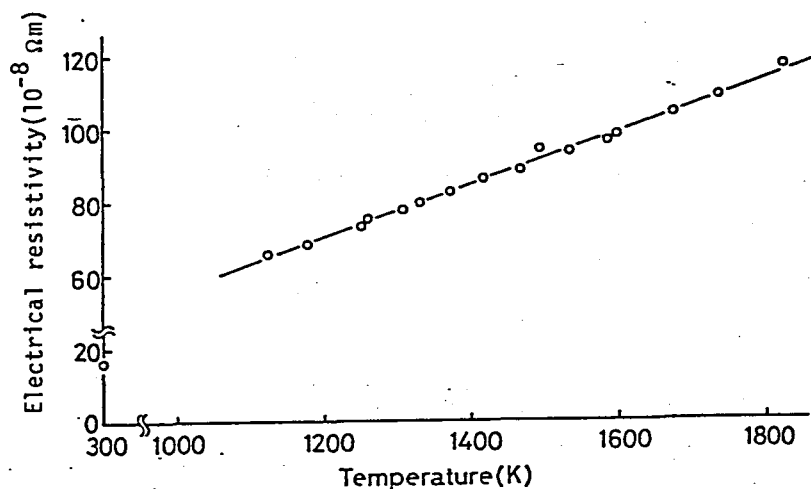Fig.3-41. Thermal conductivity of LaB_6 calculated from the thermal diffusivity data.

Fig.3-42. Electrical resistivity of LaB$_6$ at high temperature.

In general, most of the thermal energy in metal is carried by the conduction electrons. The thermal conductivity of such a metal is constant at temperatures above about one fifth of the Debye temperature. The temperature dependent behavior of the thermal conductivity of LaB$_6$ may be explained by an appreciable contribution of the lattice thermal conductivity because the thermal conductivity of insulators is also inversely proportional to temperature above the Debye temperature.

The mean free path of the phonons is limited by the electron-phonon scattering and the phonon-phonon scattering. Above the Debye temperature the latter is dominant; then in this temperature region the lattice thermal conductivity of a metal is nearly identical with that of insulators whose crystal lattice is similar to that of the metal with respect to the parameters such as the Debye temperature, a mean atomic mass and a mean atomic volume which determine the magnitude of the lattice thermal

-163-

conductivity. The Debye temperatures of common metals are at most about 400 K. The lattice thermal conductivity of such metals is about two orders of magnitude smaller than the electronic thermal conductivity at temperatures above 1000 K. On the other hand, the Debye temperature of LaB_6 is considerably higher than that of the common metals. The lattice thermal conductivity can have an appreciable value even above 1000 K.

The lattice part of the thermal conductivity of LaB_6 requires to be distiguished from the electronic thermal conductivity. The latter can be estimated using the Wiedemann-Franz law. The Wiedemann-Franz law: $K/\sigma T=L$ holds in the common metals at high temperatures, where K is the thermal conductivity, σ the electrical conductivity and L, a constant named the Lorenz number. The Wiedemann-Franz law should hold precisely at high temperatures, regardless of the shape of the Fermi surface, the form of the scattering matrix element, etc.[91]. Therefore, the Wiedemann-Franz law should be obeyed in LaB_6.

Lorenz function $L=K/\sigma T$ was calculated and is compared with L_0 in Fig.3-43, where $L_0=\pi^2/3(k_B/e)^2$ has the value of 2.44 x 10^{-8} V^2/K^2. There is a large deviation of L from L_0 which is attributed to the contribution of the lattice thermal conductivity. Then the lattice thermal conductivity $K_{lattice}$ can be calculated from the equation $K_{lattice}=K_{obs.}-L_0\sigma T$. For example, $K_{lattice}$ at 1300 K is 15 J/m·sec·K.

It must be checked whether the value calculated above is reasonable or not. Slack et al.[75] calculated the lattice
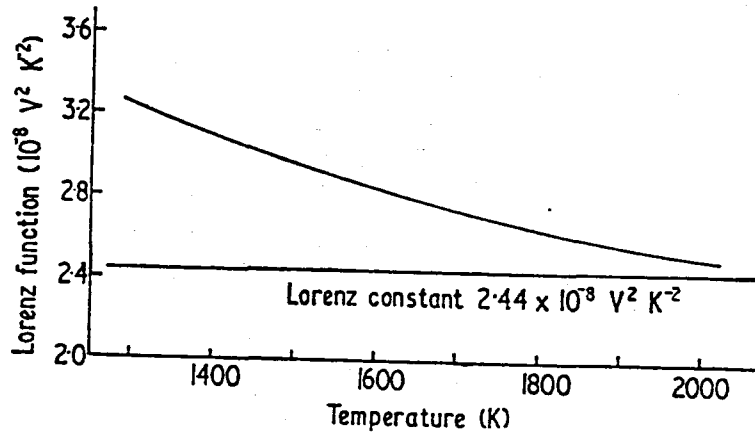
Fig.3-43. Lorenz function of LaB$_6$.

thermal conductivity of β-boron, B$_{12}$C$_3$, B$_{12}$P$_2$, B$_{12}$As$_2$ and YB$_{66}$

at the Debye temperature and compared with the experimental

value. They used the equation:

$$K_{calc.} = 5.72 \times 10^{-6} \bar{M} \Theta_{cut-off}^2 \delta \gamma^{-2} \quad J/m \cdot sec \cdot K,$$

where γ is the effective Grüneisen constant, $\bar{M}$ and δ^3 are

already defined in the section on the elastic constant, and

$\Theta_{cut-off}$ the cut-off energy of the acoustic mode. This equation

was proposed by Leibfried and Schlömann[92] using the Debye

temperature. For deriving the theoretical model, the latter

authors assumed that the crystal is a simple, monatomic cubic

solid where the acoustic phonon cut-off energy is just Θ.

According to the former authors' presentation, the acoustic

phonon cut-off energy must be used instead of the Debye tempera-

ture for complex crystals, because the thermal energy is

-165-

brought only by the acoustic phonons. The optical phonons have so small group velocities that they do not contribute to the thermal conduction.

In the case of LaB_6, the cut-off energy of the acoustic phonons is 600 K according to the lattice vibration model. The effective Grüneisen constant is assumed to be equal to 2 because a better agreement has been achieved for other elemental boron and boron compounds using that value. The calculated thermal conductivity may be the value at the Debye temperature of 773 K. Then the value at 1300 K can be estimated using a relation that the lattice thermal conductivity is inversely proportional to temperature above the Debye temperature. The calculated and the experimental lattice conductivities of LaB_6 are tabulated in Table 3-11 together with those of β-boron and other boron compounds. The agreement with the experimental value is

Table 3-11

The experimental and the calculated lattice thermal conductivities of LaB_6, β-boron and other boron compounds[75].

Material	$\rho_{obs.}$ (J/m·sec·K)	$\rho_{calc.}$	Cut-off energy of acoustic mode (K)
LaB_6	15 (1300 K)	14	600
β-boron	8 (1300 K)	8.5	180
$B_{12}C_3$	14 (1300 K)	14	340
$B_{12}P_2$	16 (1160 K)	15	310
$B_{12}As_2$	20 (940 K)	14	240
YB_{66}	2 (1300 K)	5	110

quite good; however, the above calculation may not be taken
seriously because it contains some ambiguous adjustable pa-
rameters.

The lattice thermal conductivity of LaB_6 is comparable
with those of the other boron and boron compounds. It is reason-
able to consider that the boron lattice in LaB_6 is a some modifi-
cation of the elemental boron and boron compounds rich in boron.

3-2-7. Electrical resistivity of rare-earth hexaborides

(i) CeB_6

The temperature dependence of the resistivity is shown in
Fig.3-44. The room temperature resistivity is 2.7×10^{-7} Ωm.

The resistivity ρ decreases
with decreasing temperature
and has a minimum at about
150 K. Below 150 K, the
resistivity rapidly in-
creases, reaches a maximum
value of 7.3×10^{-7} Ωm at
3.5 K, and thereafter
gradually decreases until
2.4 K where CeB_6 orders
antiferromagnetically.
Below 2.4 K, ρ decreases
steeply. Subtracting an
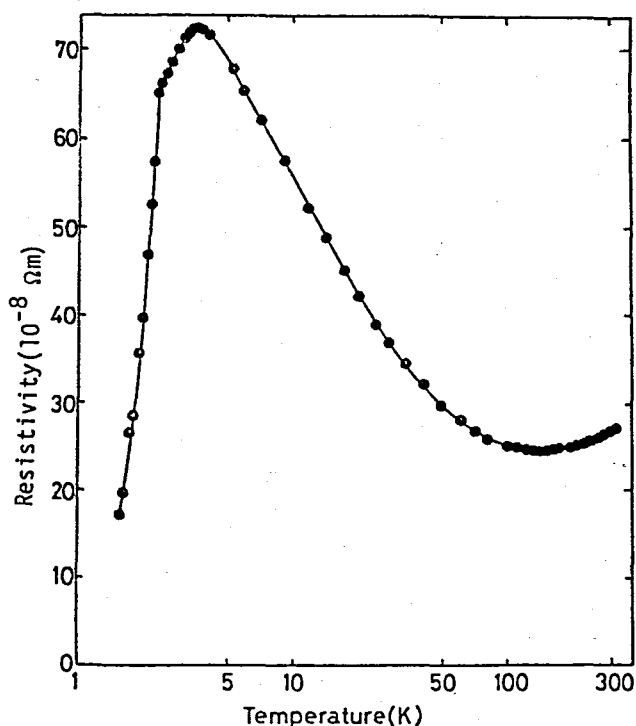estimate of the lattice

Fig.3-44. Electrical resistivity of CeB_6.

resistivity refering to the resistivity of LaB_6, the remaining resistivity is proportional to $-ln\ T$ for $5 < T < 25$ K.

It is well known that Ce ion in intermetallic compounds often gives rise to the Kondo effect[93]. Winzer[94] reported the giant Kondo effect of $La_{1-x}Ce_xB_6$. The compound CeB_6 may show a Kondo effect resembling that of $CeAl_3$[95]. Some investigations[96] of the magnetic properties of CeB_6 have been carried out, but little consideration was given to the Kondo properties of this system.

The general features of the resistivity vs. temperature curve of CeB_6 resembles that of $CeAl_3$, though there is a difference between the origins of the steep decrease of the resistivity at low temperature. In the case of $CeAl_3$, the decrease is due to the quenching of the magnetic moment in the dense Kondo state[97], while in the case of CeB_6 the sharp decrease is due to the occurence of the magnetic ordering[98]. However, it is possible that the cause of the increase of the resistivity which is proportional to $-ln\ T$, are the same for CeB_6 and $CeAl_3$. In fact, Komatsubara et al.[99] have measured the Kondo temperature by magnetoresistance experiments and have asserted that CeB_6 is a dense Kondo system. It appears that CeB_6 is an attractive compound for studying the dense Kondo state.

(ii) SmB_6

The resistivity of single crystal SmB_6 is shown in Fig.3-45

and the behavior is similar
to that previously observed
on polycrystalline specimens.

SmB_6 is a mixed valence
compound consisting of Sm^{2+}
and Sm^{3+} ions. Owing to the
fact that the metal ions in
hexaborides donate two
electrons to the valence
band, SmB_6 should exhibit
metallic conduction, but data
[100] indicate that the con-
duction is that of a semi-
conductor. The resistivity
saturates at about 4 K. The
room temperature resistivity
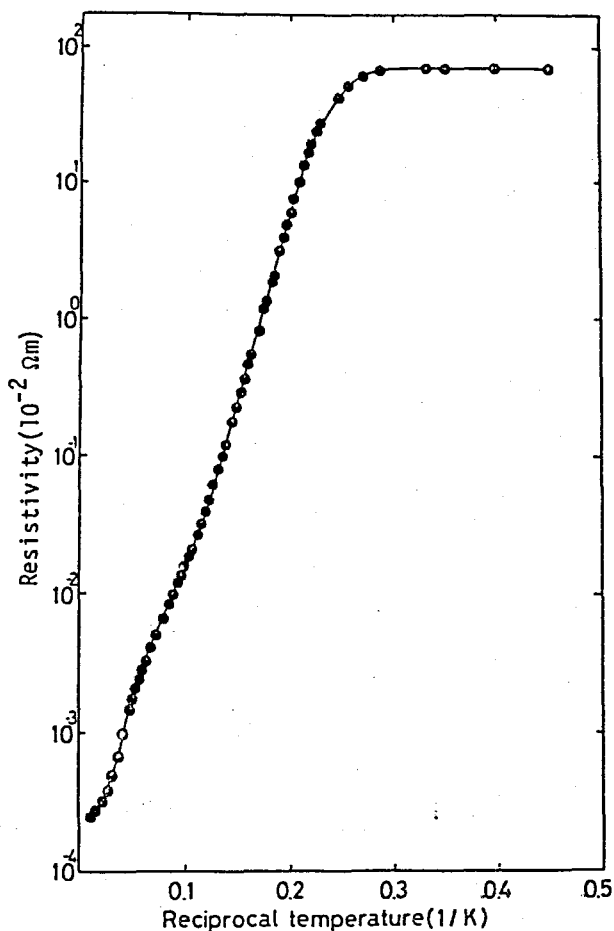is 1.88×10^{-6} Ωm and the

Fig.3-45. Electrical resistivity
of SmB_6.

saturated one is 0.707 Ωm. There is an activation region at
$10 > T > 5$ K, whose activation energy is 5.4×10^{-3} eV. It seems
that another activation region exists in the vicinity of 20 K;
however, it is difficult to estimate correctly the activation
energy because the measured temperature range is narrow. The
origins of these two processes are not understood sufficiently
yet. However, the mixed valence of SmB_6 is due to the location
of the 4f level at the Fermi level, i.e. the 4f level constructs
a very narrow band which is partly occupied and the interaction

between the 4f band and 5d band may characterize the property of SmB_6.

Both the saturated resistivity of 0.707 Ωm and the activation energy of 5.4 x 10^{-3} eV at low temperature obtained by the present study are the highest values observed until now. The saturation resistivity is very sensitive to the crystal purity as mentioned in the section on the single crystal preparation. Surface treatment of the specimen also affected the saturation value. Surface polishing by abrasive powder decreases the value by a factor of about 2. Aono et al.[101] pointed out that the ratio Sm^{3+}/Sm^{2+} at the surface is higher than that of the bulk crystal, causing surface metallic conduction since the Sm^{3+} ion donates conduction electrons. To eliminate the surface conduction, the surface of the specimen was oxidized resulting in the surface insulating layer having a resistance of the order of 10^7 Ω. The oxidation increases the saturation resistivity by a factor of 2 to 3, but the saturation behavior itself was not eliminated so that it comes partly from the bulk property of SmB_6. Kasuya et al.[80] proposed a model of a new type of Wigner lattice formation to explain the temperature dependence of the resistivity of SmB_6 and they suggested that surface metallic conduction is unimportant. The present experimental result suggests that surface conduction plays a partial role in the resistance saturation mechanism.

(iii) GdB$_6$

The temperature dependence of the resistivity of No.901 GdB$_6$ is shown in Fig.3-46. The resistivity decreases with decreasing temeprature above 30 K and steeply decreases below the Néel temperature of 15.4 K. GdB$_6$ has already been known to order antiferromagnetically at about 15 K[102]. A new anomaly at about 10 K is observed. This resistance anomaly has a hysteresis as shown in Fig.3-46. This hysteresis appears more clearly for No.904 GdB$_6$ crystal as shown in Fig.3-47. In the figure, the P-state, H-state, H'-state and L-state are defined to be the states above T_N, just below T_N, below $T_{N'}$ and T_P, respectively. Characteristic
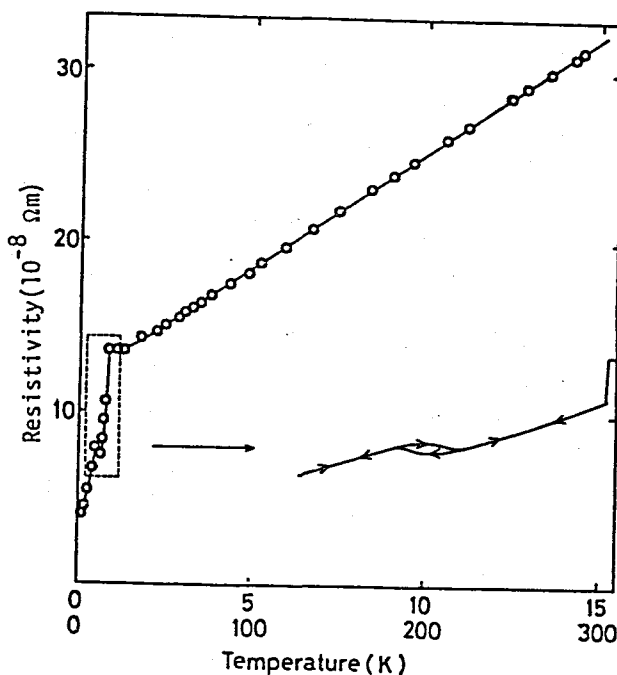

Fig.3-46. Electrical resistivity of No.901 GdB$_6$. An anomaly having a hysteresis can be observed at about 10 K.

features connected with each transition are the following,

T_N: The value is 15.4 K for No.901 and 15.25 K for No.904. The resistivity steeply changes at T_N with $\Delta\rho=0.02$ $\mu\Omega m$ ($\Delta\rho_{No.901}$ is slightly larger than $\Delta\rho_{No.904}$).

$T_{N'}$: $T_{N'}$ can be observed only for No.904. In the case of No.901, since T_P becomes higher than $T_{N'}$, a transition occurs directly

-171-

from the L-state to the
H-state. In a magnetic
field (used for both
torque meausurement at
0.5 T and magneto-
resistance measurement
at 0.9 T), T_N, disappear-
ed.

T_p: Hysteresis exists
with increasing and
decreasing temperature.

T_p and the hysteresis
are strongly sample
dependent, for instance, $\Delta\rho_{No.901}$ and $\Delta T_{No.901}$ are 0.006 $\mu\Omega m$ and

Fig.3-47. Electrical resistivity of No.904
GdB_6 crystal at low temperature.

2 K. $\Delta\rho_{No.904}$ and $\Delta T_{No.904}$ are 0.04 $\mu\Omega m$ and 3 K, respectively.
At the transition region, the crystal has an intermediate state
between L-state and H'-state. If the temperature variation is
changed from increasing (or decreasing) to decreasing (increasing),
the resistivity curve in the transition region does not follow
the hysteresis curve, but goes down (up) parallel to the
curve of L-state and/or H'-state from its initial position in
the transition region. The magnetic measurements[103] show
the L-state has three equivalent magnetic domains with colinear
antiferromagnetic spins along the equivalent <100> axes.
With increasing temperature through T_p, the spins flop into a
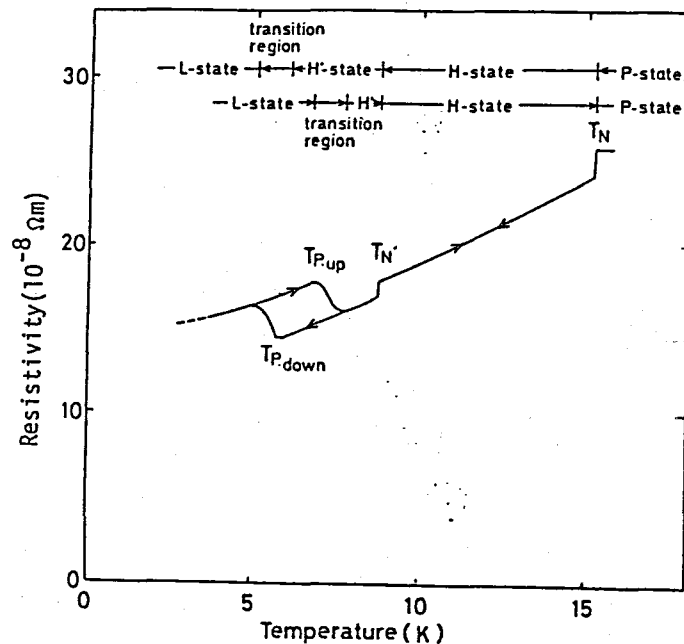plane perpendicular to the spin axis of the L-state. The crystal

symmetry at H-state is tetragonal. Since GdB_6 has cubic symmetry above T_N, there must exist a structural phase transition near T_N which is induced by the magnetic ordering at H-state. Hysteresis has not been observed at T_N by the present resistance measurement. Since there is a large hysteresis at T_p, another structural phase transition occurs between the H'-state and the L-state. The transition between the H-state and the H'-state may be caused by a change in the magnetic structure. For further understanding, it is necessary to investigate the effects that the magnetic field has on the resistivity of GdB_6.

Additional X-ray measurements are required to determine the structure of each state and to ascertain whether these observed phenomenoa are due to an intrinsic property of GdB_6 or an extrinsic one which is induced by impurities or imperfections in the crystal.

According to the lattice vibration model of LaB_6, the metal ion is loosely bound in the boron framework. Atomic radius or ionic radius of the rare-earth elements decreases with increasing atomic number. It is the so-called lanthanide contraction. In the MB_6 structure, the lattice constant hardly decreases when the ionic radius of the metal ion decreases. The binding force of the metal ion becomes weaker in the boron framework as the atomic number increases, which decreases the stability of the MB_6 structure. It is likely that the phase transition of GdB_6 at low temperature is caused by such an

instability of the MB_6 structure. In fact, though the MB_6 structure is the most stable phase in the RE-B systems from La to Eu, the MB_4 structure becomes the most stable phase instead of the MB_6 structure beyond Eu. Therefore, the ionic radius of Gd^{3+} ion has already exceeded some critical value representing the stability limit of the MB_6 structure.

For both cases of SmB_6 and EuB_6, part of the metal ions or most of the metal ions become divalent, which increases the ionic radius of metal ions as an average. Thus the stability of the MB_6 structure is held in SmB_6 and EuB_6. The location of the unoccupied 4f-levels near the Fermi level enables the above situation. The temperature dependence of the resistivity of such rare-earth hexaborides must be understood by considering the existence of this unoccupied 4f-levels. This problem has been remained unsolved.

In conclusion of this section, though the M-B bonding in the MB_6 structure is considerably weak as compared with the B-B bonding, it takes part some important roles with respect to the stabilization of the MB_6 structure.

3-3. Discussion on band structure and bonding of MB_6 and MB_2
3-3-1. LaB_6

At first, the calculated energy band of LaB_6 by Hasegawa and Yanase[16] is shown in Fig.3-48 for the case of $\alpha=1$, in which the calculated Fermi surface represents better the experimental Fermi surface than the case of $\alpha=2/3$. The essence

of the band structure does not change when the 4f-levels are
taken into account for want of fitting the calculated neck
Fermi surface better to the observed one[61].

In Fig.3-48, three electron bands around -2.8 Ryd.*
consist mainly of La-5p states becuase whose Bloch states
contain mainly La-p components. Valence bands consist of B-2s2p
and La-6s states and are located above this La-5p band. A
valence band around -0.1 Ryd. which consists mainly of B-2s2p,
splits from above locating valence bands owing to the crystal
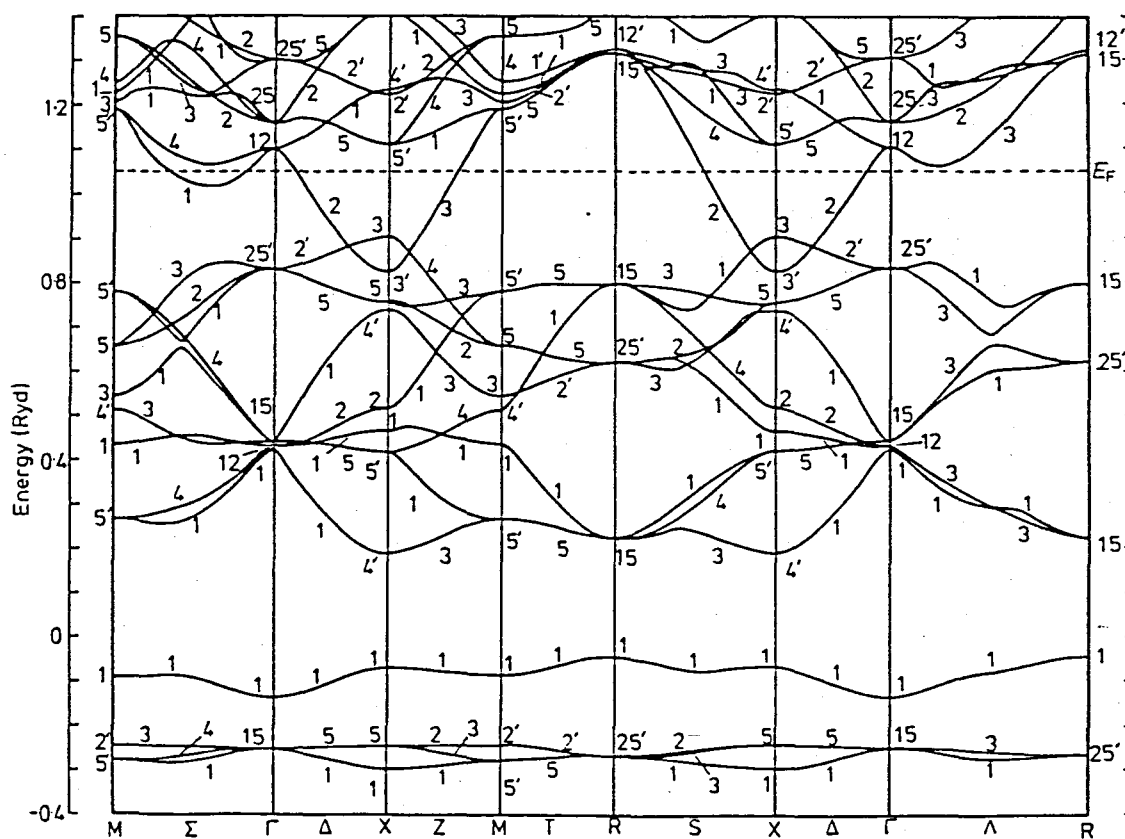field effect. Valence bands of from 2nd to 10th band are

Fig.3-48. Energy band structure of LaB_6 calculated by Hasegawa
and Yanase[16].

*1 Ryd.=13.6 eV

constructed also by B-2s2p states mainly and by La-6s states slightly. The width of this valence bands is about 0.6 Ryd.

The 11th band is a conduction band consists of mainly La-5d states and B-2s2p states mix considerably. This hybridization of B-sp states into La-5d states is a characteristic feature of metal hexaborides.

The Fermi energy is calculated to be 2.0 eV in the improved calculation. The calculation confirmed the forecasts from the experimental results; (1) the La-5d character is main in the conduction band and the B-2s2p states mix into the conduction band. (2) The Fermi energy is close to the free electron value of 2.1 eV.

The effective mass is one of the representatives of the conduction band structure. The calculated band mass are compared with the experimental ones in Table 3-12. It seems that the calculated effective masses are too small. The improved value of the effective mass can be obtained as follows. The conduction electron concentration is 1.39×10^{28} m^{-3}. The Fermi surface of LaB$_6$ is approximated by three equivalent nearly spherical Fermi surfaces. Each sphere contains one third of the total conduction electron. The average Fermi wave number k_F can be obtained by the equation:

$$1.39 \times 10^{28}/3 = (4\pi/3)k_F^3/4\pi^3 .$$

The obtained k_F is 5.16×10^9 m^{-1}. Assuming the parabollic band:

$$E_F = \frac{\hbar^2}{2m*}k_F^2 .$$

Table 3-12

Effective mass of LaB_6. $\vec{B}//(1\bar{1}0)$

Branch	Angle (deg)	dHvA mass $(m*/m_0)$ Present	Arko	Calculated mass $(m*/m_0)$ Hasegawa α=1.0	α=2/3	Walch α=1.0	α=2/3
α_3	0[001]		0.610	0.44	0.40	0.29	0.40
α_3	7	0.64±0.02					
α_3	37		0.642				
α_3	52	0.67±0.02					
α_3	90[110]		0.650				
$\alpha_{1,2}$	90[110]		0.650				
γ	0[001]			0.46	0.42	0.61	
ε	0[001]			0.23	0.22	0.37	
ζ	54.7[111]		0.234				
δ	90[110]		0.460				

Substituting E_F=2.0 eV and the value of k_F, the effective mass is 0.51 m_0. The value approximates the real band mass better than those calculated by Hasegawa and Yanase[16] and Walch et al. [60].

Such a relation holds for the electron density of states. The density of states of 1.10 states/eV·unit cell at the Fermi level is obtained from the measured γ-value of the electronic heat capacity whose value is 2.60 mJ/mole·K^2. The density of states calculated is too small as compared with the measured density of states as shown in Table 3-13. This is ascribed to too large a dispersion of the calculated conduction band. It is also the cause of too light an effective band mass above

Table 3-13

The DOS od LaB$_6$ at the Fermi level (in units of $\frac{states}{eV \cdot unit\ cell}$).

| Experimental | Hasegawa and Yanase | | Walch et al. |
	$\alpha=1.0$	$\alpha=2/3$	$\alpha=1.0$
1.10	0.70	0.64	0.37

mentioned. Assuming the parabollic band also, the density of states per spherical surface can be expressed as,

$$D(E) = \frac{3N}{2E}$$

where $D(E)$ is the density of states at energy E. Using the values of $E_F = 2.0$ eV and $N = 1.39 \times 10^{28}$ m^{-3}, the density of states per spherical Fermi surface is 0.35 states/eV·unit cell at the Fermi level, leading to the total density of states 1.05 states/eV·unit cell. The electron-phonon interaction increases the theoretical density of states in the same manner as the case of the effective mass. Thus the above estimated density of states approximates the observed one well.

Though the La-5d character is main in the conduction band, the mixing of B-2s2p states spreades out its width. The conduction band occurs as a light mass band having approximately the parabolic dispersion. This is one reason that LaB$_6$ has low electrical resistivity. High Debye temperature of LaB$_6$ ought to lower the resistivity much more but it is prevented by the existence of the energetically low lying M-B relative motion modes.

There is no essential alteration of the valence band

structure derived by Longuet-Higgins and Roberts. The valence

bands of LaB_6 consists of mainly the B-2s2p states. New

aspect is slight mixing of La-6s states into the valence bands.

This decreases the electron transfer from 2 electrons per unit

cell(Longuet-Higgins and Roberts result) to 1.5 electrons per

unit cell(Hasegawa and Yanase result using $\alpha=1.0$).

The Longuet-Higgins and Roberts aspects of the strong

B-B bonding can explain the observed values of the elastic

constants, Raman frequencies and the lattice thermal conduc-

tivities. The effect of the electron transfer can be connected

through ionic bond between metal atom and boron lattice to the

contribution of the "optical phonon scattering" on the electrical

resistivity. On the other hand, the effect of the weak M-B

bonding appears in the low calorimetric Debye temperature at

low temperature and the temperature dependence of the electrical

resistivity.

The force constant of the M-B bonding is about one tenth

of the B-B bonding. Because the frequencies of the lattice

vibrations are proportional to the square root of the force

constant divided by the atomic mass, that is, $\nu \propto \sqrt{f/M}$ where

ν is the frequency and f the force constant. The frequency of

the B-B stretching mode is about ten times larger than that of

the M-B relative motion modes. Moreover, the atomic mass

concerned to each mode differs about an order of magnitude

since the atomic mass concerned to the B-B mode is one boron

atom mass, while the atomic mass concerned to the M-B mode is

the reduced mass of one La atom mass and one boron octahedron

mass. The force constant f should differ an order of magnitude

between the B-B bonding and the M-B bonding.

The M-B bonding is partly ionic caused by the electron

transfer and partly covalent due to the mixing of La-6s states

into B-2s2p states. The latter contribution to the total

elastic energy seems to be very small, though, it takes part

in the stabilization of the MB_6 structure. When the atomic

number of the rare-earth metal increases with decreasing the

stability of the MB_6 structure, the M-B covalent bond is the most

variable one as compared with the B-B covalent bond and the

ionic bond, because the interatomic distances of the B-B bonding

and the M-B bonding hardly change though the ionic radius of the

metal ion changes considerably.

In conclusion, the B-B bonding in the MB_6 structure is

apparently dominant but the M-B bonding plays important roles

at boundary regions of some phenomena.

3-3-2. IVth group transition metal diborides

The energy band structure of ZrB_2 and TiB_2 by Ihara[17]

are shown in Fig.3-49(a) and (b). In both cases the α factor

is 2/3. The experimental indication that ZrB_2 and TiB_2 are

semi-metals, is confirmed by these energy band structures,

because a small overlap in energy of the conduction and valence

bands can be seen in these figures.

Both band structures resemble each other. However, every
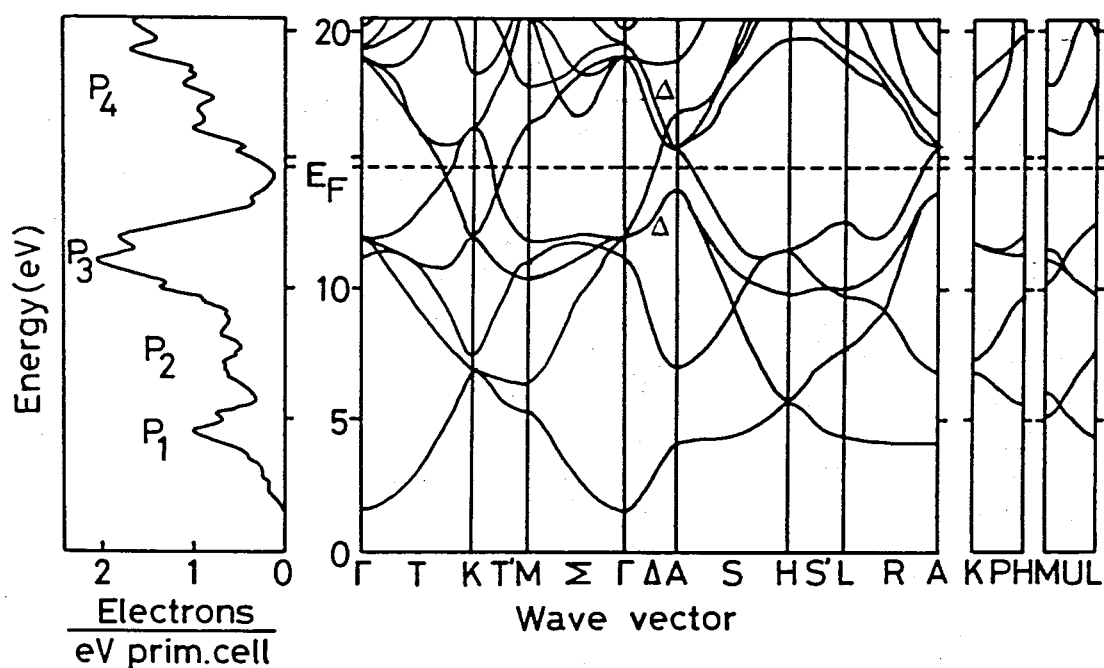
(a)
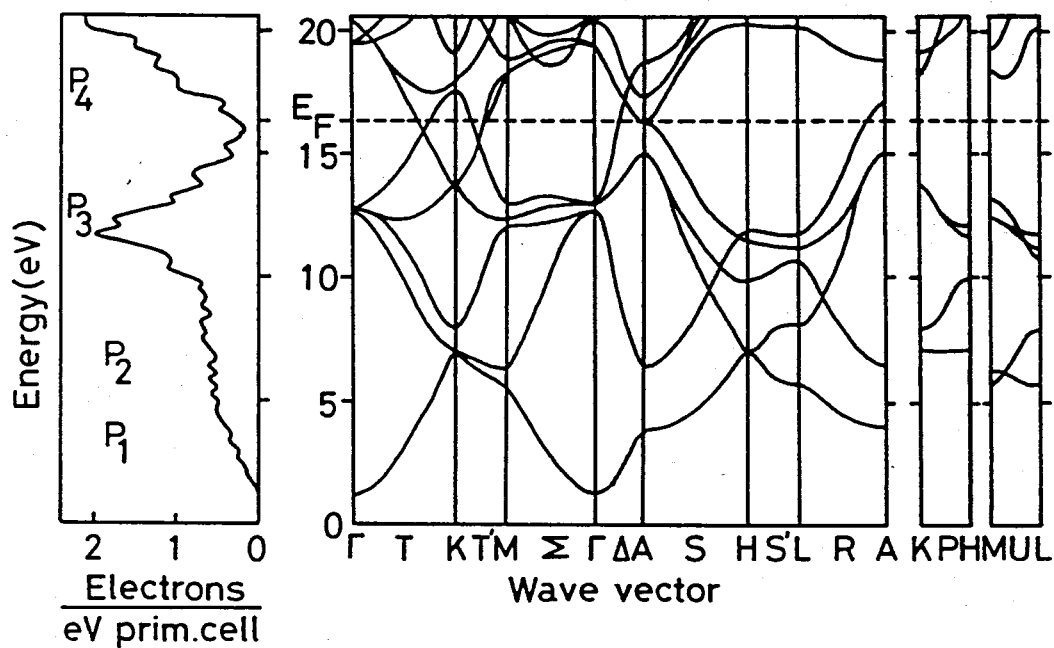
(b)

Fig.3-49. Energy band structure and density of states of (a)ZrB_2 and (b)TiB_2 calculated by Ihara[17].

peak of the density of states of TiB_2 is broader than those of ZrB_2 and correspondingly the band width of the valence band, 14.9 eV, of TiB_2 becomes wider than that of ZrB_2 (13.0 eV). Furthermore, TiB_2 has a deeper bonding band P_3 located 4.3 eV below from the Fermi level than that of ZrB_2 (3.3 eV).

The band structure is explained for the case of ZrB_2. The density of states curve of the valence band consists of three main parts, i.e. two marked peaks P_1 and P_3 and one between them, P_2. The peak P_1 corresponding to the first band, has a s-like character, consisting of B-2s state. The 2nd and part of the 3rd band contribute to the peak P_2 which is ascribed to the B-2p states. The peak P_3 and P_4 which are located just below and above the Fermi level, are bonding and antibonding parts constructed by the mixing of Zr-4d and B-2p states. Flat parts of these bands have d-like character. Moreover, according to Johnson's calculation[64], the Zr-4d states mix slightly with the bonding sp^2 band of borons which corresponds to the peaks P_1 and P_2, and retains still its identity. The band in the vicinity of the Fermi level consists of B-p_z state but it is strongly mixed with Zr-p_z and especially Zr-$d_{xz,yz}$ states. The band does not resemble at all the bonding π-band of graphite.

The characteristic features of the bonding nature of MB_2 are as follows,

(1) the dominant bonding is the M-B covalent bond.

(2) The B-B covalent bond is not so strong as graphite.

(3) There is little electron transfer.

-182-

A suitable indication of the first feature is the behavior of the Δ-band between the point A and Γ in the Brillouin zone as shown in Fig.3-49(a). The bonding Δ-band at A is purely B-p orbital. The anti-bonding Δ-band at A is purely Zr-4d orbital. Moving from A to Γ, the Zr-4d and B-p mix in-phase in the bonding Δ-band. As Γ is approached, the mixing increases, lowering its energy. This corresponds to the M-B covalent bond. On the other hand, the anti-bonding band increases its energy as the mixing increases. The bonding band is fully occupied and the anti-bonding band is unoccupied.

The bonding nature of the IVth group diborides is quite different from that of the MB_6. The previous bond model that the dominant bonding in the MB_2 is the B-B covalent bond and two valence electrons per formula weight transfer from the metal atom to the boron lattice, is not suitable for MB_2. Since the dominant bonding is along the inter-layer direction, the electronic properties of the diborides do not behave in a two-dimensional manner though they have a layer structure. The intra-layer B-B distance varies by a relatively large fraction as the atomic radius of the metal changes, since the sp^2-bonding is not completed.

The present model can explain the available experimental results. The γ-value of the electronic heat capacity is proportional to the electronic density of states at the Fermi level. Schematic density of states curve of diboride is shown in Fig.3-50, on which the γ-values of some transition metal

diborides are plotted[104].

They agree well with the
density of states curve.

The carrier concen-
trations of some diborides
have been estimated from
the Hall coefficient meas-
urement. IVth group
diborides have very small
concentrations of electrons
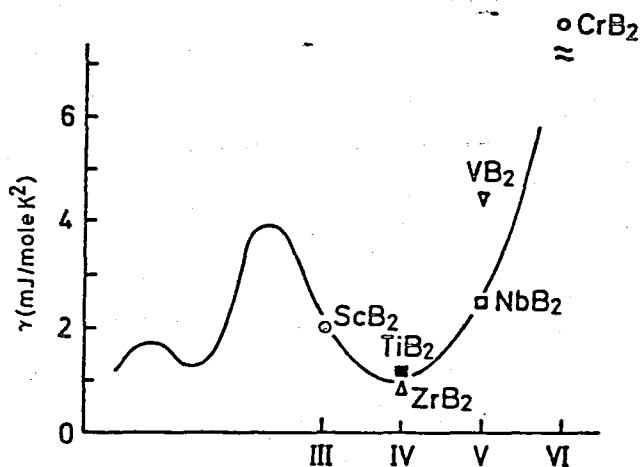and holes because they are
semi-metals. Therefore,

Fig.3-50. Schematic density of states of transition metal diborides and their γ-values of electronic specific heat.

IIIrd and IVth group diborides should have one electron per

Table 3-14

The expected and the observed carrier concentrations of transition metal diborides.

Material		Expected carrier concentration (N/unit cell)	Observed carrier concentration (N/unit cell)	Ref.
III	YB_2	1	1.1	[9]
	TiB_2		0.02	
IV	ZrB_2	0	0.04	
	HfB_2		0.11	[105]
	VB_2		1.4	[105]
V	NbB_2	1	1.7	[105]
	TaB_2		0.6	[105]

formula weight. The reported results are summarized in Table 3-14. The agreement is rather good since the above consideration does not take into account the effect of the band modification from the simple parabolic band.

The NMR measurement for ^{11}B in TiB_2 and ZrB_2 by Silver and Bray[10] has been considered as one of the basis of the electron transfer theory. They measured $|e^2 qQ|$=0.36 MHz for TiB_2 and $|e^2 qQ|$=0.12 MHz for ZrB_2. Those values are very small as compared with Townes-Dailey approximation which gives $|e^2 q_{T.D.} Q|$=5.4 MHz. This $|e^2 q_{T.D.} Q|$ value is based on the assumption that the three valence electrons of a boron atom form sp^2-bonds, i.e. the concentration of each p-orbital is $N(p_x)$= $N(p_y)$=1 and $N(p_z)$=0. Therefore, Silver and Bray concluded that the electric field gradient at the boron site must be nearly spherically symmetric by achieving closed shell configuration, i.e. $N(p_x)$=$N(p_y)$=$N(p_z)$=1. It requires the electron transfer from the metal atom. However, in the present model, it is considered that the sp^2-bonding band is not completed because of the mixing of the Zr-4d states, while the p_z-states constructs the bands near the Fermi level together with Zr-p_z and $d_{xz,yz}$ states. Since both ZrB_2 and TiB_2 are semi-metals, the bands near the Fermi level are only partially filled. The p_z-state is not completed. Therefore, any p-orbitals are partially filled and their concentrations are nearly equal to each other, i.e. $N(p_x) \approx N(p_y) \approx N(p_z) < 1$. In this case, the electric field gradient at the boron site becomes nearly spherically symmetric

also, leading to the small $|e^2qQ|$ value as observed.

In conclusion, the most striking picture of the bonding of the IVth group transition metal diborides is that the dominant bonding is the M-B covalent bond caused by the hybridization of the B-2p states and the metal-d states.

Chapter 4. Conclusions

The main conclusions obtained by this study are as follows.
(1) The single crystals of non-oxide refractory borides(rare-earth hexaborides and transition metal diborides) have been prepared by the floating zone method in an ambient pressurized gas atmosphere using induction heating method. The single crystals of most of the rare-earth hexaborides have been for the first time prepared in this study. The chemical composition of these crystals has been controlled to achieve the stoichiometric composition according to their melting behavior. The crystal purities have been markedly improved by the repetition of the zone refining which has not been successfully achieved by the previous investigators.

(2) The Fermi surface of LaB_6 consists of the multiply-connected ellipsoidal Fermi surface located at X point in the Brillouin zone. The conduction band is constructed mainly by the La-d states and there is a considerable admixture of the B-2s2p states in the conduction band. The latter spreads the conduction band width markedly, resulting in the light effective mass of the conduction electrons though the conduction band character is still d-like.

(3) The valence bands of LaB_6 consist mainly of the B-2s2p states and to a small extent the La-6s states. The dominant bonding in LaB_6 is the B-B covalent bond. There is a contribution of the M-B covalent bond in addition to the M-B ionic bond which is caused by the electron transfer from the metal atom to the

boron framework. The M-B covalent bond takes part in stabilizing the MB_6 structure.

(4) The lattice vibration of the MB_6 structure can be classified into three kinds of vibration modes; (1) the boron lattice vibrates solely, (2) the metal atom vibrates coincidently with the boron lattice and (3) the metal atom vibrates almost solely. The third mode effectively contributes to the temperature dependence of the heat capacity and the electrical resistivity at low temperature.

(5) The IVth group transition metal diborides are semi-metals. The Fermi surfaces of ZrB_2 consist of the ring-like electron surface around K point which is attached together with the ellipsoidal Fermi surfaces, and the wrinkled dumbbell-like hole Fermi surface at A point.

(6) The valence bands of the IVth group diborides are constructed by the p-d hybrid bonding band between the M-d states and B-p states. The bonding B-sp^2 bands which form the hexagonal boron layer, do not have the closed shell configuration like the graphite layer but are only partly occupied. The conduction bands of the diborides are the p-d hybrid anti-bonding bands. The valence bands are almost occupied and the conduction bands are not.

(7) The dominant bonding in the IVth group diborides is the M-B covalent bond. The B-B bonding is not so strong like in graphite. There is little electron transfer between the metal atoms and the boron atoms.

This study has served the development of the preparation methods for the non-oxide refractory compounds and the single crystal cathode of LaB_6 which is replacing the conventional tungsten filament cathode in some special fields such as electron beam lithography. Furthermore, many basic studies have been carried out on the surface structure of LaB_6 and on its dynamic properties using single crystals in order to support the development of the single crystal cathode. This study undertook the most basic part of the investigations of LaB_6 and other borides.

Acknowledgements

References

[1] B. Aronsson, "Borides, Silicides and Phosphides" Wiley, New York, 1965

[2] L. E. Toth, "Transition Metal Carbides and Nitrides" Academic, New York, 1971

[3] J. L. Hoard and R. E. Hughes, "The Chemistry of Boron and its Compounds" (E. L. Muetterties ed.) Wiley, New York, 1967

[4] K. E. Spear, "Phase Diagrams" vol.4 (A. M. Alper ed.) Academic, New York, 1976

[5] L. Pauling, "The Nature of the Chemical Bond" Cornell Univ., New York, 1960

[6] H. C. Longuet-Higgins and M. de V. Roberts, Proc. Roy. Soc.(London) A224 336(1954)

[7] W. N. Lipscomb and D. J. Britton, J. Chem. Phys. 33 275(1960)

[8] D. B. DeYoung and R. G. Barnes, J. Chem. Phys. 62 1726(1975)

[9] R. W. Johnson and A. H. Daane, J. Chem. Phys. 38 425 (1963)

[10] A. H. Silver and P. J. Bray, J. Chem. Phys. 32 288(1960)

[11] J. Etourneau, J. P. Mercurio, R. Naslain and P. Hagenmuller, J. Solid State Chem. 2 332(1970)

[12] G. V. Samsonov, "High-Temperature Materials and Technology" (I. E. Campbell and E. M. Sherwood ed.) Wiley, New York, 1965

[13] G. T. Meaden, "Electrical Resistance of Metals" Plenum, New York, 1965

[14] J. Piper, J. Phys. Chem. Solids 27 1907(1966)

[15] A. P. Cracknell, "The Fermi Surfaces of Metals" Taylor and Francis, London, 1971

[16] A. Hasegawa and A. Yanase, J. Phys. F 7 1245(1977)

[17] H. Ihara, Researches of the Electrotechnical Laboratory, No.775(1977)

[18] Selected from recent Issues of J. Crystal Growth, J. Materials Science, etc.

[19] T. Aita, U. Kawabe and Y. Honda, Japan. J. Appl. Phys. 13 391(1974)

[20] H. Koltz, Naturwissenschaften 52 451(1965)

[21] T. Niemyski and E. Kierzek-Pecold, J. Crystal Growth 3,4 162(1968)

[22] I. V. Zubeck, R. S. Feigelson, R. A. Huggins and P. A. Pettit, J. Crystal Growth 34 85(1976)

[23] D. Elwell, I. V. Zubeck, R. S. Feigelson and R. A. Huggins, J. Crystal Growth 29 65(1975)

[24] S. Muranaka and S. Kawai, J. Crystal Growth 26 165(1974)

[25] B. J. Curtis and H. Graffenberger, Mater. Res. Bull. 1 27(1966)

[26] P. H. Keck and W. V. Horn, Phys. Rev. 91 512(1953)

[27] W. G. Pfann, "Zone Melting" Wiley, New York, 1966

[28] W. G. Moffatt, "Binary Phase Diagrams Handbook" General Electric, New York, 1977

[29] J. S. Haggerty, J. F. Wenkus and D. W. Lee, Proc. 3rd Internat. Symp. High Temp. Technol., Butterworths, London, 1967 p.547

[30] W. Heywang and G. Ziegler, Z. Naturforsch. 9a 561(1954)

[31] W. Heywang, Z. Naturforsch. 11a 238(1956)

[32] N. Kobayashi, J. Crystal Growth 43 417(1978)

[33] D. M. Wroughton, E. C. Okress, P. H. Brace, G. Comenetz
      and J. C. R. Kelley, J. Electrochem. Soc. 99 205(1952)

[34] W. G. Pfann and D. W. Hagelbarger, J. Appl. Phys. 27
      12(1956)

[35] E. Storms and B. Mueller, J. Phys. Chem. 82 51(1978)

[36] K. Takagi and M. Ishii, J. Crystal Growth 40 1(1977)

[37] R. W. Johnson and A. H. Daane, J. Phys. Chem. 65 909
      (1961)

[38] J. D. Verhoeven, E. D. Gibson, M. A. Noack and
      R. J. Conzemius, J. Crystal Growth 36 115(1976)

[39] M. A. Noack and J. D. Verhoeven, J. Crystal Growth 49
      595

[40] J. M. Ziman, "Electrons and Phonons" Oxford, London,
      1963

[41] C. Oshima, T. Tanaka, E. Bannai and S. Kawai, Japan.
      J. Appl. Phys. 16 965(1977)

[42] S. Funahashi, private communication.

[43] L. Onsager, Phil. Mag. 43 1006(1952)

[44] A. S. Josef, A. C. Thorsen, E. Gertner and L. E. Valby,
      Phys. Rev. 148 569(1966)

[45] E. P. Papadakis, J. Appl. Phys. 35 1474(1964)

[46] J. Yoshimoto, Report of Nat. Inst. Res. Inorg. Mater.
      No.16 p.108(1978)

[47] W. J. Parker, R. J. Jenkins, C. P. Butler and G. L. Abbott, J. Appl. Phys. $\underline{32}$ 1679(1961)

[48] Y. Takahashi, J. Nuclear Mater. $\underline{51}$ 17(1974)

[49] R. D. Cowan, J. Appl. Phys. $\underline{32}$ 1363(1961)

[50] M. J. Wheeler, Br. J. Appl. Phys. $\underline{16}$ 365(1965)

[51] G. V. Samsonov, L. Ya. Markevski, A. F. Zigach and M. G. Valayshko, "Boron, Its Compounds and Alloys" Acad. Sci. Ukrainian S. S. R. Kiev, 1960

[52] A. J. Arko, G. Crabtree, D. Karim, F. M. Mueller and L. R. Windmiller, Phys. Rev. B$\underline{13}$ 5240(1976)

[53] C. Kittel, "Introduction to Solid State Physics" 5th ed. Wiley, New York, 1976

[54] D. Shoenberg, F. R. S. and P. J. Stiles, Proc. Roy. Soc. London A$\underline{281}$ 62(1964)

[55] D. Shoenberg, F. R. S., Phil. Trans. Roy. Soc. London A$\underline{255}$ 85(1962)

[56] D. G. Howard, Phys. Rev. $\underline{140}$ 1705(1965)

[57] Y. Ishizawa, H. Nozaki and T. Tanaka, J. Phys. Soc. Japan $\underline{48}$ 1439(1980)

[58] I. M. Lifshits, M. Ya. Azbel and M. I. Kaganov, "Electron theory of Metals" Consultants Bureau, New York, 1973

[59] P. G. Perkins, D. A. Armstrong and A. Breeze, J. Phys. C $\underline{8}$ 3558(1975)

[60] P. F. Walch, D. E. Ellis and F. M. Mueller, Phys. Rev. B$\underline{15}$ 1859(1977)

[61] A. Hasegawa and A. Yanase, "Extended Abstracts for US-Japan Seminor(Physical Properties of Rare-Earth Magnetic Semiconductors)" Sendai, p.204, 1977

[62] S. H. Liu, L. Kopp, W. B. England and H. W. Myron, Phys. Rev. B11 3463(1975)

[63] H. Ihara, M. Hirabayashi and H. Nakagawa, Phys. Rev. B16 726(1977)

[64] D. L. Johnson, B. N. Harmon and S. H. Liu, J. Chem. Phys. 73 1898(1980)

[65] P. G. Perkins and A. V. J. Sweeney, J. Less-Common Metals 47 165(1976)

[66] H. J. McSkimin and W. L. Bond, Phys. Rev. 105 116(1957)

[67] F. H. Featherston and J. R. Neighbours, Phys. Rev. 130 1324(1963)

[68] D. I. Bolef and J. de Klerk, J. Appl. Phys. 33 2311(1962)

[69] J. J. Gilman and B. W. Roberts, J. Appl. Phys. 32 1405 (1961)

[70] L. J. Graham, H. Nadler and R. Chang, J. Appl. Phys. 34 1572(1963)

[71] S. Haussühl, Zeits. Kristallogr. 110 67(1958)

[72] E. G. Spencer, R. T. Denston, T. B. Buteman, W. B. Snow and L. G. Van Uitert, J. Appl. Phys. 34 3059(1963)

[73] D. D. Betts, A. A. Bhatia and M. Wyman, Phys. Rev. 104 37(1956)

[74] E. F. Steigmeier, Appl. Phys. Letters 3 6(1963)

[75] G. A. Slack, D. W. Oliver and F. H. Horn, General Electric

Technical Information Series, No.71-C-143(1971)

[76] M. Ishii, T. Tanaka, E. Bannai and S. Kawai, J. Phys.

Soc. Japan 41 1075(1976)

[77] M. Ishii, private communication.

[78] T. Shimanouchi, M. Asahina and S. Enomoto, J. Polymer

Sci. 59 93(1962)

[79] T. Fujita, private communication.

[80] T. Kasuya, K. Takegahara, T. Fujita, T. Tanaka and E. Bannai,

J. de Phys. Colloque C5 40 308(1979)

[81] M. Ishii, M. Aono, S. Muranaka and S. Kawai, Solid State

Commun. 20 437(1976)

[82] F. Gompf, G. Schell and H. Winter, Progress Report Teil-

intitut Nukleare Festkörperphysik, Gesellschaft für

Kernforschung, KfK 2670 17(1978), 2881 20(1979)

[83] M. Ishii, private communication.

[84] J. Bardeen, J. Appl. Phys. 11 88(1940)

[85] D. J. Howarth and E. H. Sondheimer, Proc. Roy. Soc.

(London) A219 53(1953)

[86] W. D. Ryden, A. W. Lawson and C. C. Sartain, Phys. Rev.

B1 1494(1970)

[87] L. Colquitt, Jr. J. Appl. Phys. 36 2454(1965)

[88] T. Tanaka, T. Akahane, E. Bannai, S. Kawai, N. Tsuda

and Y. Ishizawa, J. Phys. C 9 1235(1976)

[89] C. N. King, H. C. Kirsh and T. H. Geballe, Solid State

Commun. 9 907(1971)

[90] D. S. MacLachlan, R. Mailfert, B. Souffache and J. P. Burger,

Proceeding Low Temp. Phys. LT14 $\underline{3}$ 40(1975)

[91] J. M. Ziman, "Electrons and Phonons" Oxford, London, 1963

[92] G. Leibfried and E. Schlömann, Nachr. Akad. Wiss. Göttingen, II Math. Phys. Kl $\underline{4}$ 71(1954)

[93] J. H. Moeser, F. Steiglich and G. V. Minigerode, J. Low Temp. Phys. $\underline{15}$ 91(1974)

[94] K. Winzer, Solid State Commun. $\underline{16}$ 521(1975)

[95] A. S. Edelstein, C. J. Toanchita, J. D. McMasters and K. A. Gschneidner, Jr. Solid State Commun. $\underline{15}$ 81(1974)

[96] J. C. Nickelson and R. M. White, J. Appl. Phys. $\underline{40}$ 1011 (1969)

[97] B. Cornut and B. Coqblin, Phys. Rev. B$\underline{5}$ 4541(1972)

[98] K. N. Lee and B. Bell, Phys. Rev. B$\underline{6}$ 1032(1972)

[99] T. Komatsubara, T. Suzuki, N. Kawakami, T. Fujita, Y. Isikawa, A. Takase, K. Kojima, M. Suzuki, Y. Aoki, K. Takegahara and T. Kasuya, J. Mag. and Magnetic Mater. (17-19) (1980)

[100] J. C. Nickelson, R. M. White, K. N. Lee, R. Backmann, T. H. Geballe and G. W. Hull, Jr. Phys. Rev. B$\underline{3}$ 2030 (1971)

[101] M. Aono, T. Tanaka, E. Bannai and S. Kawai, Appl. Phys. Letters $\underline{31}$ 323(1977)

[102] B. R. Coles, T. Cole, J. Lambe and N. Laurance, Proc. Phys. Soc. $\underline{79}$ 84(1962)

[103] H. Nozaki, T. Tanaka and Y. Ishizawa, J. Phys. C $\underline{13}$

2751(1980)

[104] Y. S. Tyan, L. E. Toth and Y. A. Chang, J. Phys. Chem.
Solids $\underline{30}$ 785(1969)

[105] H. J. Juretschke and R. Steinitz, J. Phys. Chem. Solids
$\underline{4}$ 118(1958)